

Dual Modality Optical Coherence Tomography and Multispectral Fluorescence
Imaging for Ovarian Cancer Detection

by

Tyler Houston Tate

A Dissertation Submitted to the Faculty of the

COLLEGE OF OPTICAL SCIENCES

In Partial Fulfillment of the Requirements

For the Degree of

DOCTOR OF PHILOSOPHY

In the Graduate College

THE UNIVERSITY OF ARIZONA

2016

THE UNIVERSITY OF ARIZONA

GRADUATE COLLEGE

As members of the Dissertation Committee, we certify that we have read the dissertation prepared by Tyler Tate, titled *Dual Modality Optical Coherence Tomography and Multispectral Fluorescence Imaging for Ovarian Cancer Detection* and recommend that it be accepted as fulfilling the dissertation requirement for the Degree of Doctor of Philosophy.

_____ Date: (12/20/2016)

Jennifer K. Barton

_____ Date: (12/20/2016)

Urs Utzinger

_____ Date: (12/20/2016)

Jim Schwiegerling

Final approval and acceptance of this dissertation is contingent upon the candidate's submission of the final copies of the dissertation to the Graduate College.

I hereby certify that I have read this dissertation prepared under my direction and recommend that it be accepted as fulfilling the dissertation requirement.

_____ Date: (12/20/2016)

Dissertation Director: Jennifer K. Barton

STATEMENT BY AUTHOR

This dissertation has been submitted in partial fulfillment of the requirements for an advanced degree at the University of Arizona and is deposited in the University Library to be made available to borrowers under rules of the Library.

Brief quotations from this dissertation are allowable without special permission, provided that an accurate acknowledgement of the source is made. Requests for permission for extended quotation from or reproduction of this manuscript in whole or in part may be granted by the head of the major department or the Dean of the Graduate College when in his or her judgment the proposed use of the material is in the interests of scholarship. In all other instances, however, permission must be obtained from the author.

SIGNED: Tyler Houston Tate

ABSTRACT	7
CHAPTER 1: INTRODUCTION	8
1.2.1. Hallmarks of Cancer and Their Detection	10
1.2.2. Ovarian Cancer Characteristics.....	11
1.2.3. Existing Screening Methods	12
1.2.4. Endoscopic Screening.....	14
1.2.5. Potential Optical Imaging Technologies for Cancer Screening.....	15
1.3.1. Interferometry and Temporal Coherence.....	18
1.3.2. Endoscopic OCT System Design Overview	20
1.3.3. TD-OCT.....	21
1.3.4. FD-OCT.....	22
1.3.5. Light-Tissue Interaction.....	25
1.3.6. Lateral Resolution and Depth of Field.....	26
1.3.7. Scanning Geometry.....	29
1.3.8. Fiber-based Implementation	32
1.4.1. Fluorescence Process	33
1.4.2. Intrinsic vs. Extrinsic Fluorescence	35
1.4.3. Fluorescence Imaging Systems.....	37
CHAPTER 2: PRESENT STUDY.....	40
CHAPTER 3: FUTURE WORK	46
REFERENCES.....	50
APPENDIX A: MFI <i>EX VIVO</i> STUDY	57
A.1. Accepted Manuscript	57
2.7.1 Descriptive Statistics.....	68
2.7.2 Logistic Regression Analysis on Ovarian Tissue.....	69
2.7.3 Quadratic Discriminant Analysis on Ovarian Tissue.....	70
A.2. Data Storage.....	85
A.2.1. Raw data and analysis images.....	85
A.3. Standard Operating Procedures.....	87
A.4. Statistical Analysis.....	98
A.4.1. Biostatistics shared service	98
A.4.2. Discriminant Analysis.....	99
A.5. MATLAB Scripts.....	100
A.5.1. Initial Image Processing.....	100

A.5.2.	Preparation for statistical analysis.....	101
A.5.3.	Statistical Analysis.....	105
APPENDIX B: FALLOSCOPE.....		122
B.1.	Submitted Manuscript.....	122
B.2.	Data Storage.....	145
B.3.	Standard Operating Procedures.....	146
B.4.	Lens Design Files.....	147
B.4.1.	Distal 3 element Objective.....	147
B.4.2.	Proximal Illumination System	149
B.5.	MATLAB scripts	153
B.5.1.	Gaussian Beam Modeling	153
B.5.2.	CFB Image Processing.....	160
B.5.3.	USAF Test Target Modulation Contrast Measurements.....	166
APPENDIX C: DOUBLE REFLECTION COVER PLATE..		170
C.1.	Detailed Lens overview	170
C.2.	Lens Prescription	191
C.3.	MATLAB Scripts.....	197

LIST OF FIGURES

Figure 1.1: Michelson interferometer for OCT imaging.....	19
Figure 1.2: Coefficient of absorption (1/cm) as a function of wavelength for oxygenated hemoglobin (HbO ₂), deoxygenated hemoglobin (Hb) and water (H ₂ O).	25
Figure 1.3: Δx , D and DOF as functions of NA for a wavelength of 1 micron in air.....	26
Figure 1.4: Example of Gaussian beam distal OCT modeling.....	28
Figure 1.5: Jablonski energy diagram of the fluorescence process in a fluorophore with two excitation peaks and one emission peak.	34

LIST OF TABLES

Table 1.1: Table comparing necessary components for TD-OCT, SD-OCT and SS-OCT and the primary contributors to system optical specifications for each system.....	21
--	----

ABSTRACT

Ovarian cancer is the deadliest gynecologic cancer for women. Diagnosis at the local stage leads to 91% 5-year survival rates, but only 15% of cases are detected early. Existing screening methods have proven ineffective in large clinical trials. Screening is complicated by the heterogeneity of the disease with multiple types of ovarian cancer originating both on the ovary and in the fallopian tube. Early stage cancer is too subtle for non-invasive imaging techniques such as ultrasound or magnetic resonance imaging. This study evaluates the feasibility and design of dual modality, multispectral fluorescence imaging (MFI) and optical coherence tomography (OCT) endoscopes for improved ovarian cancer screening.

The study is broken up into three sections. In the first study MFI is validated in an *ex vivo* imaging study of human ovarian and fallopian tube tissue samples. Tissue autofluorescence excited by ultraviolet and blue wavelengths is shown to be a promising discriminator between normal and cancerous tissue.

The second study combines OCT and MFI into a sub millimeter diameter endoscope designed to screen for ovarian cancer by screening inside the fallopian tube and at the ovary. The small size is required for screening the full length of the fallopian tube. MFI is implemented as a wide-field navigational imaging technique with high sensitivity complemented by high resolution structural depth imaging of OCT over a limited field of view.

The final study presents a novel lens design for a scanning fiber endoscope with forward-viewing navigation and side-viewing OCT. A piezo tube is used to scan an optical fiber providing both the navigation channel's illumination and OCT imaging. The design spatially separates the forward-viewing illumination from the OCT. As the piezo fiber circularly scans at its maximum deviation the OCT beam focus is rotationally scanned out the side of the endoscope tip by a rotationally symmetric double reflection in the cover plate.

CHAPTER 1: INTRODUCTION

1.1 Motivation

Ovarian cancer is the deadliest gynecologic cancer for women. Over 22,000 new cases and 14,000 deaths occur per year, in the United States alone. Overall 5-year and 10-year survival rates are just 46% and 35% respectively¹. Diagnosis at the local stage leads to 91% 5-year survival rates, but only 15% of cases are detected early. In comparison, the overall 5-year survival rate for breast cancer is 91% with 61% of cases detected early stage¹. Breast cancer often presents with a specific symptom such as a lump or mass and mammography is a reasonably good, available and noninvasive screening method.

Unlike breast cancer, ovarian cancer has either no or nonspecific early stage symptoms and currently no effective screening option exists. Nonspecific symptoms may include bloating, abdominal pain, difficulty eating or urinary urgency. In general, existing screening techniques including pelvic examination, transvaginal ultrasound and a blood test for the CA125 tumor marker have proven ineffective in reducing death rates in multiple large clinical trials²⁻⁴. One trial showed possible benefit after 7-14 years of annual multi-modality screening for some population groups³. These preliminary data are not sufficient to recommend screening in the general population, but further validation of reduction in mortality is underway with results expected in 2019, which may lead to screening recommendations for some populations.

While the average lifetime risk of developing ovarian cancer is 1 in 76, certain high risk groups have lifetime risk as high as 1 in 2⁵. Primary risk factors are having BRCA1 or BRCA2 gene

mutations or having family history of breast or ovarian cancer. Other risk factors include pelvic inflammatory disease, Lynch syndrome, menopausal hormone therapy and tobacco smoking. Due to the lack of an effective screening method, many high risk women are often recommended to have a prophylactic salpingo-oophorectomy with hysterectomy in which the ovaries, fallopian tubes and uterus are removed. While effective, there are significant side-effects including increased mortality for women who undergo the procedure before age 45 without hormone replacement^{6,7}. Ideally a noninvasive screening method will be developed for all women. However, a screening method with similar invasiveness to a colonoscopy may be appropriate for regular screening, particularly in high-risk women who wish to maintain fertility and normal hormonal function as long as possible.

This work focuses on the development and integration of advanced optical imaging techniques into endoscopes for ovarian cancer screening. The imaging techniques used are optical coherence tomography (OCT) and multispectral fluorescence imaging (MFI). OCT provides high resolution depth images of tissue microstructure, but has a small field of view limiting utility for survey and navigation. MFI complements OCT by providing wide-field navigational imaging. Unlike a traditional white light camera, MFI obtains a series of fluorescence and reflectance images with a specific set of excitation wavelengths and emission bands. The excitation and emission wavelengths can be chosen to target specific endogenous fluorophores with fluorescence signal dependent on tissue pathology. Thus MFI will provide a wide field of view survey modality with enhanced contrast for abnormal biomolecule concentrations. Abnormal regions can then be further examined with the high resolution depth imaging of OCT for diagnostic confirmation. Miniaturization of both modalities into sub millimeter diameter endoscopes is possible for eventual use as an ovarian cancer screening technique.

1.2 Ovarian Cancer

1.2.1. Hallmarks of Cancer and Their Detection

Development of a screening method first requires a brief overview of what cancer is and thus what features may be used for identification during screening. Cancer is a blanket term covering many diseases all characterized by both uncontrolled divisions of cells and ability to spread into or invade nearby tissues. Many, but not all cancers form a solid tumor. As the cancer progresses, cancerous cells begin to migrate through physical contact, the circulatory system or the lymphatic system. Seminal papers from Hanahan and Weinberg in 2000⁸ and 2011⁹ outline identifying hallmark features distinguishing cancerous from normal cells. The original six hallmarks are: sustaining proliferative signaling, evading growth suppressors, activating invasion and metastasis, enabling replicative immortality, inducing angiogenesis and resisting cell death. The follow-up report lists two additional hallmarks- deregulating cellular energetics and avoiding immune destruction- as well as two characteristics that enable cancer development- genome instability and mutation, and tumor-promoting inflammation.

Hallmarks such as proliferation, invasion and angiogenesis can be seen as anatomical changes resulting in tumor and nearby vasculature growth. Imaging techniques designed to image anatomical changes can be considered structural imaging techniques. This includes the standard imaging configurations of ultrasound (US), magnetic resonance imaging (MRI) and OCT.

Most of the hallmarks can also be associated with physiological changes. For example, a cancerous cell can signal the surrounding microenvironment to promote angiogenesis. These functional changes in cell signaling are associated with changes in the concentrations of molecules used for signaling. If the changes are large enough and result in a secreted factor, they may be able to be detected via a blood test.

Imaging can also target physiological changes. The amino acids tryptophan, tyrosine and phenylalanine, structural proteins collagen and elastic, metabolic co-factors hydrogenated

nicotinamide adenine dinucleotide (NADH) and Flavin adenine dinucleotide (FAD), and porphyrins are endogenous fluorophores and have intrinsic fluorescence (autofluorescence). Each of these molecules naturally absorb certain wavelengths of light and then emit lower energy (longer wavelength) light. Physiological changes otherwise too small to spatially resolve can be detected as changes in autofluorescence intensity as molecular concentrations change.

Autofluorescence imaging of cancer inside the body requires a close proximity imaging system in order to deliver the necessary excitation wavelength with sufficient intensity, and have sufficient collection of generally weak autofluorescence signals. Extrinsic signals can also be generated using dyes or tracers designed to attach to a specific molecule that is part of a physiological signaling mechanisms and then emit a known signal. Dyes require specific excitation wavelengths and emit at know wavelengths, and the setups used to detect these targeted fluorophores are substantially similar to those used for autofluorescence. Tracers can emit radiation detectable using external imaging techniques such MRI or positron emission tomography (PET). Extrinsic dyes and tracers allow targeting of more specific physiological targets and have stronger signals, but can add additional complexity as many are not approved for use in humans and must be administered before imaging.

1.2.2. Ovarian Cancer Characteristics

Ovarian cancer is a heterogeneous term referring to a diverse group of malignancies affecting the ovary and fallopian tube. Tumors typically develop from either epithelia cells, sex cord-stromal cells or germ cells¹⁰. Tumors developing from epithelial cells account for 60% of total tumors, but are the most likely to become malignant accounting for 90% malignant tumors¹¹. Sex cord-stromal and germ cell tumors respectively account for 7% and 3% malignancies¹². Both of these cell types reside on the interior of the ovary making detection via imaging more challenging. Epithelial cells cover the surface of the ovary and fallopian tube. Multiple types of cancers can develop from each of the three cell types. Each type of ovarian cancer has unique

morphological and molecular genetic features¹³. The heterogeneity complicates detection, treatment and monitoring of ovarian cancer.

In general, ovarian cancers can be divided into type I and type II tumors. Type I tumors tend to be less aggressive and are often detected at earlier stages. Type II tumors, including high-grade serous and high-grade endometrioid carcinomas, are very aggressive and typically not detected until later stages. The type II tumors are most often epithelial in origin and account for 75% of all epithelial carcinomas¹³. These cancers can originate in the epithelial lining of either the ovary or the fallopian tube, particularly the fimbriated end. The epithelial lining on the surfaces of the ovary and fallopian tube is approximately 100 microns thick in normal conditions. Precursor lesions to ovarian cancer that develop in the fallopian tube epithelial lining may be as small as 4-5 cell layers (~50 microns), causing some epithelial thickening¹⁴. Noninvasive depth imaging techniques such as OCT are well suited to screening the epithelial layer with sufficient resolution to detect precursor lesions. Integration into a screening endoscope would provide a screening method for the deadliest and most difficult to detect ovarian cancers originating in the epithelium.

1.2.3. Existing Screening Methods

Developing an effective screening method is challenging largely due to a combination of small precursor lesion size and limited access to the ovaries and fallopian tubes¹⁴. Ovarian cancer is heterogeneous with multiple genetic and epigenetic factors contributing to the development of various types of ovarian cancer¹⁵. Additionally, emerging consensus suggests that perhaps over 50% of the most lethal form of the disease, high grade serous ovarian cancer, originates in the fallopian tube^{10,16}. Early detection is particularly critical because ovarian cancer has no anatomical barriers to early metastasis into the peritoneal cavity. The combination of complicated biology, subtle physical changes and high probability for early metastasis makes regular and effective screening both challenging and critical.

Screening approaches can broadly be categorized as physical examination, biomarker testing or imaging. Physical screening methods include pelvic examination in which the ovaries are evaluated for size, shape and consistency. While pelvic exams are useful for detecting many gynecologic conditions, most early stage ovarian cancers do not present sufficient changes for pelvic exam detection.¹⁷

Blood test for biomarkers offers the least invasive route for screening, but the heterogeneity of ovarian cancer has hindered development of an effective biomarker test. Currently a blood test for the CA-125 biomarker is available. Decreasing CA-125 levels in patients who have ovarian cancer can indicate positive response to treatment¹⁸. However, multiple large clinical trials have shown testing CA-125 levels to be ineffective as a screening technique and high rates of false positives can result in complications from unnecessary follow-up procedures^{2-4,19}. Research on a more robust biomarker test for ovarian cancer is ongoing²⁰⁻²². Development of a reasonably effective blood test for ovarian cancer screening with high sensitivity and moderate specificity would be groundbreaking. Such a test could be used for annual non-invasive screening. However, a follow-up screening procedure to a positive test results capable of validating the diagnosis and providing localization of the disease remains critical.

Imaging inside the body can be done via external or internal techniques. Use of external techniques, such as MRI and PET, is preferred because they are completely non-invasive. These techniques are useful for preoperative staging of later stage cancer, but have proved ineffective for early-stage screening with insufficient resolution to detect subtle anatomical early-stage changes²³. Similar to the CA-125 blood test, functional PET and MRI techniques have shown strong ability to evaluate recurrent disease and response to treatment. Sensitivity to early stage disease is limited with current functional techniques making them unsuitable for early-stage screening²³.

Improved resolution can be achieved by internal imaging in which the imaging system is placed inside the body for close contact with the disease site. Transvaginal ultrasound is a clinically available and minimally invasive imaging technique sometimes used for ovarian cancer screening, but as with other existing screening methods it has proved ineffective for early-stage detection²⁴.

1.2.4. Endoscopic Screening

Although more invasive than other methods discussed, optical imaging endoscopy may be the most promising screening approach. To access the fallopian tube and ovary an endoscope has three primary approaches. Laparoscopic endoscopes enter the body through an incision in the abdomen. This approach allows for probes with diameter as large as 10 mm and is useful for validating advanced imaging techniques during laparoscopic oophorectomy procedures with minimal patient risk. The procedure is too invasive to be considered as a viable regular screening technique. Additionally, the angle of entry is not optimal for evaluating inside the distal fallopian tube.

Alternatively, there are two transvaginal approaches. An endoscope, or falloposcope, can access the ovary by passing through the natural pathway of the vagina, uterus, and fallopian tube. The invasiveness is similar to that of a colonoscopy which is an accepted cancer screening method. The approach allows for screening the entire length of the fallopian tube in addition to the ovary. The proximal tubal opening of the fallopian tube is located in the uterus with an ostium diameter of approximately 1 mm²⁵. The size constraint requires optical techniques suitable for ultra-miniaturization.

A second transvaginal approach is to access the ovary and distal fallopian tube via a small incision in the posterior fornix of the vaginal wall. This allows a reasonable-sized endoscope (e.g. 3 mm diameter) to access the ovary and distal FT by passing through the rectouterine pouch (pouch of Douglas). The insertion angle naturally leads the endoscope to the distal openings of

the fallopian tubes. Introducing a small amount of sterile saline into the pouch allows the floppy fimbriated ends of the FTs to float open for complete visualization. Endoscopic screening using either transvaginal procedure is suitable for a clinical setting requiring little preparation and only local anesthesia.

1.2.5. Potential Optical Imaging Technologies for Cancer Screening

Advanced optical imaging techniques have sufficient anatomical or functional imaging capabilities to detect early-stage cancer. Promising results have been demonstrated imaging ovarian cancer with OCT^{26–29}, confocal microscopy^{30–33}, multiphoton microscopy (MPM)^{34,35}, photoacoustic imaging (PAI)^{29,36–38} and fluorescence spectroscopy/imaging^{39–41}. With the exception of certain fluorescence imaging configurations, all of the advanced optical techniques have high resolution, small field of view, are point- or line-scanning imaging methods or require reconstruction, and thus have limited utility for navigation or rapid, large-area visualization. Some, such as multiphoton microscopy and photoacoustic imaging, typically utilize complex laser systems which are less suitable for a robust, inexpensive clinical imaging system, although, new fiber-based laser systems may enable small portable systems^{42–47}. All of the above high resolution optical techniques may have promise for detecting early stage ovarian cancer assuming the imaging system can be placed near or in contact with the cancerous region of the epithelium.

An endoscope ideally combines a wide field of view navigational technique with a high resolution technique. White-light imaging is typically used for endoscopic navigation. In an endoscope the total number of imaging pixels are limited based on the size of the endoscope. With a static pixel count increasing field of view reduces resolution. Wide-field white-light imaging may easily miss small early-stage tumors with similar appearance to surrounding tissue. One approach to increasing tumor sensitivity without increasing resolution is to increase the contrast of the tumor relative to the surrounding tissue. Morphological changes in the tissue may

change the light-tissue interaction in terms of absorption, scattering, or polarization. Chemical changes in the tissue can be imaged using a functional imaging technique such as fluorescence.

Fluorescence imaging can be accomplished by modifying a white light imaging system to have specific illumination and emission wavelength bands targeting fluorophores. Allowing for multiple excitation and emission bands creates an MFI system capable of improved evaluation of the complex changes in molecular concentrations associated with ovarian cancers. An advantage of fluorescence imaging is that the fluorescence signal from each fluorescing molecule is effectively a point source. The imaging system can detect changes in the quantities of the point sources without sufficient spatial resolution to detect each point source. In a dual modality configuration where MFI is combined with a high resolution imaging technique, the MFI system needs high sensitivity. That is to say the navigational system can accurately identify all potentially cancerous signals.

As a complementary high-resolution technique, OCT can provide a highly specific diagnosis of regions with abnormal fluorescence signals. OCT provides structural depth imaging over a limited field of view. OCT has axial resolution of a few microns suitable to detect precursor lesions a few cell layers thick. While there are other high resolution imaging techniques that can be used, OCT is a well-established technique that is very well suited to miniaturization and has previously proven utility *in vivo* ovarian cancer detection in a laparoscope²⁶.

1.3 OCT

OCT is a low coherence interferometric technique used for imaging. It is often considered the optical analog to US imaging. Similar to US, OCT can acquire cross-sectional depth images in tissue. While US imaging devices typically use frequencies in the 1 to 20 MHz range, OCT typically uses near infrared light with frequencies in the 200 to 400 THz range. The much higher frequencies and thus shorter wavelengths decrease depth of penetration to a few millimeters while increasing lateral resolution to around ten microns.

Both technologies fundamentally detect back reflections caused by changes in the speed of the wave (acoustic or electromagnetic) at sample interfaces. For US this typically means boundaries of fluid, soft tissue, bone, etc. can be clearly distinguished. The increased resolution and sensitivity of optical waves enables distinguishing layers of a few cell thickness from each other within a tissue sample. For example, OCT is frequently used to image the eye and individual layers within the retina can be resolved. One fundamental difference between the technologies is how the depth or location of an object is determined for reconstruction. In US the average speed of sound through the sample is known and the difference in time between emission and detection of a reflected ultrasonic wave can be measured. From this information the distance the wave travelled before reflection can be calculated and thus the location of a boundary between materials of different refractive index is known. The speed of light is approximately 881 thousand times faster than the speed of sound making precise time of flight measurements over a depth of a few millimeters unrealistic. OCT image reconstruction fundamentally differs from US in that it requires interferometric techniques.

Originally developed for ophthalmology^{48,49} OCT was quickly modified for use in catheters and endoscopes⁵⁰. The utility of OCT has been demonstrated for diagnosis of cancers in the esophagus⁵¹⁻⁵³, gastrointestinal tract⁵⁴⁻⁵⁷, bilio-pancreatic ductal system^{58,59}, urinary tract⁶⁰, cervix⁶¹ and ovary^{26,62}. Previous works have covered the mathematical derivation of the physics

underlying OCT in depth⁶³. The focus of this research is implementing OCT into endoscopes for ovarian cancer screening. An overview of physics behind the different types of OCT is provided, but the emphasis of the section is on the considerations necessary for integrating OCT into an endoscope.

1.3.1. Interferometry and Temporal Coherence

Interferometry extracts information from the superposition of waves. When two waves of the same frequency combine the variations in intensity pattern are due to phase differences between the waves. This interference pattern can be measured in order to determine the phase difference. The wavefront and thus phase of a beam of light is altered by each optical element it interacts with via reflection, refraction or transmission. In order to determine how close an optical element is to specifications, a wavefront that has interacted with the element can be interfered with a known ideal wavefront. Deviations from normal will induce a known amount of phase change that can be measured with very high precision in the interference pattern. There are many configurations of interferometers for a wide array of applications. OCT is an amplitude splitting, low coherence interferometric technique, most commonly implemented in Michelson interferometer configuration (Figure 1.1).

The spectrum of the light source used in an interferometer determines the sources temporal coherence and thus coherence length. A purely monochromatic light source would have infinite temporal coherence. That is to say the interference fringes in the Michelson interferometer would measure the fractional difference in optical path length between the two arms of the interferometer with high visibility independent of any integer wavelength difference between the path lengths. Each wavelength in a light source has slightly different frequency. The farther the optical path difference (OPD) deviates from zero between the two arms of the interferometer the farther out of phase each source frequency becomes. At some threshold the OPD will become

significant enough that the constructive and destructive interference from the source frequencies will negate each other and interference fringes will cease to be visible.

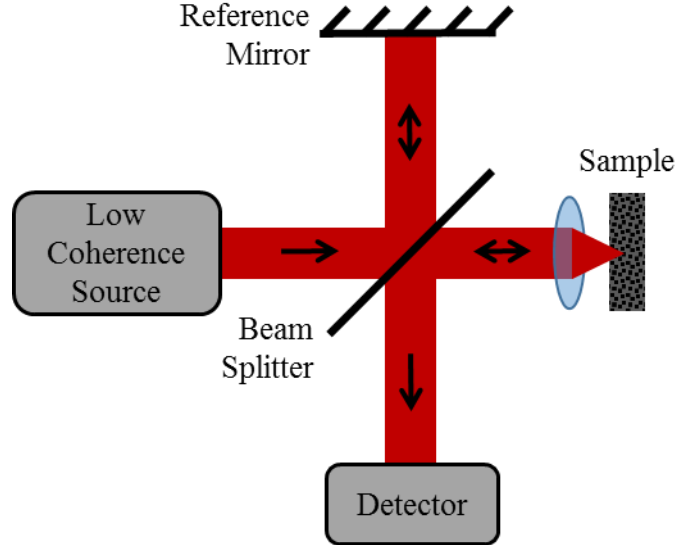


Figure 1.1: Michelson interferometer for OCT imaging.

The Fourier transform of the power spectrum of the source is known as the coherence function. The coherence length, l_c , is defined as the full-width at half-maximum (FWHM) of the coherence function. For OCT the coherence length defines the axial resolution, Δz . For a Gaussian source power spectrum with central wavelength λ_0 and normalized $1/e$ bandwidth, $\Delta\lambda$, the coherence length and thus axial resolution is given by:

$$\Delta z = l_c = \frac{2 \ln(2)}{\pi} * \frac{\lambda_0^2}{\Delta\lambda}$$

Choice of coherence length is largely application specific. For measurement of smoothly varying, polished optics with small height difference a nearly monochromatic source and thus long coherence length is preferred. This is known as high coherence interferometry and techniques exist to directly calculate height changes from the interference patterns resulting in sub angstrom axial resolutions. These techniques are not suitable for determining locations of many discrete reflectors in an inhomogeneous medium such as tissue. Such calculations can only

measure fractional wavelength changes in OPD so sudden changes in the interference pattern may indicate a discontinuity in surface height but the size of the discontinuity cannot be calculated. In contrast, due to Fourier relationships a broadband source (~ 100 nm) has low coherence. Thus fringes are only visible within a coherence length around zero OPD between the sample and reference arm. A fringe generating reflection in the object will have maximum fringe visibility with zero OPD between the sample and reference arm. The known optical path length of the reference arm can thus be used to calculate the depth of the object. This allows accurate measurements of axial locations of discrete reflectors in an inhomogeneous medium such as tissue. Axial resolution depends on coherence length in this configuration and is on the order of a few microns in typical OCT systems.

1.3.2. Endoscopic OCT System Design Overview

Ultimately an OCT endoscope needs to provide diagnostic imaging in a clinically useful system. To be clinically useful the system needs to be robust, simple and display easy to interpret images. Fundamentally OCT only generates a single depth scan, A-scan, per acquisition. In order to generate a 2D or 3D image, the OCT system must be scanned at the sample. The acquisition rate of the OCT system and the desired pixel resolution will determine what size images can be acquired for real-time imaging. Whether the endoscope needs to be forward- or side-viewing and what the most useful scanning geometry is will be determined by the application. The wavelength dependent optical properties of the tissue being imaged including index of refraction, scattering coefficient and absorption coefficient must be considered in the system design as this will fundamentally limit imaging depth. If the OCT system is designed to detect cancerous lesions then the range of possible lesion depths and size is critical in determining the necessary lateral resolution, axial resolution, focal depth and depth of focus.

The method of image reconstruction is determined by whether the system is a time-domain OCT (TD-OCT) or Fourier domain OCT (FD-OCT) system. FD-OCT has two common

implementations known as spectral domain OCT (SD-OCT) and swept source OCT (SS-OCT). Choice of system type will determine possible acquisition speeds, signal-to-noise ratio (SNR) and the necessary components to build the system (Table 1.1). Practical considerations such as whether the implement the system using fiber optics, free space optics or a combination of both must be considered. An overview of how each type of system works and how each component impacts the system performance is provided.

Component	TD-OCT	SD-OCT	SS-OCT
Ref. Mirror	Scanning	Stationary	
Detector	Photodiode	Spectrometer	Photodiode
Light Source	Broadband		Swept Source
System Spec			
A-Scan rate	Ref. Mirror	Detector	Light Source
Axial Resolution	Source; $\Delta Z = l_c = \frac{2 \ln(2)}{\pi} * \frac{\lambda_0^2}{\Delta \lambda}$		
Lateral Resolution	Distal optics; $\Delta x = \frac{0.61 \lambda_0}{NA}$		
Penetration Depth	λ dependent light-tissue interaction		
B-scan Geometry	Endoscopic scanning scheme		

Table 1.1: Table comparing necessary components for TD-OCT, SD-OCT and SS-OCT and the primary contributors to system optical specifications for each system.

1.3.3. TD-OCT

TD-OCT systems were the original implementation of OCT and are the most conceptually intuitive. As discussed earlier the interference fringes in the sample will only be visible near zero OPD between the sample and the reference arm. In order to scan the sample in depth a time domain system physically scans the mirror in the reference arm to change the optical path length (OPL) of the reference arm. This effectively scans the location of zero OPD through the sample, creating a depth profile as a function of time. Each scan of the mirror creates a single depth profile known as an A-scan. On the detection side only a single element photodiode is necessary.

TD-OCT is fundamentally limited in scanning speed, typically on the order of kilohertz, by the rate at which the reference mirror can be scanned. The scanning speed of the reference mirror introduces a Doppler shift into the interference signal that must be removed by demodulation. There are some advanced approaches such as placing multiple partially reflecting mirrors in the reference arm to allow for increased scanning speeds⁶⁴⁻⁶⁸. The major advantages of TD-OCT systems over Fourier domain systems is generally lower cost and complexity, particularly in terms of detection and image reconstruction.

1.3.4. FD-OCT

FD-OCT is an alternative approach for A-scan generation that overcomes the need for a scanning reference mirror. Rather than detecting the full spectrum of the source simultaneously the interference pattern on the detector is sampled in wavenumber. There is a Fourier relationship between the interference pattern sampled in wavenumber and the depth location of scatterers creating the interference pattern. An inverse Fourier transform can be applied to the spectrally sampled interference pattern to generate an A-scan.

As discussed in the interference section above, narrower source bandwidth corresponds to longer temporal coherence length. While a broadband source has overall low coherence, small spectral ranges within the total bandwidth have longer coherence lengths. By sampling the interference signal with sufficiently high spectral resolution the coherence length for each spectral sample can have coherence length long enough for fringe visibility over the entire imaging depth. Increased spectral resolution increases coherence length of each spectral sample and thus possible imaging depth.

In an FD-OCT system the zero OPD location is set just before (outside of) the sample. Each scatterer in the tissue creates a back reflection that interferes with the reference beam. As a function of wavenumber the interference pattern generated from each scatterer is a cosine function with frequency proportional to the distance between zero OPD and the scatterer location

(depth). The overall spectrally sampled signal is thus a super position of cosine functions from each scatterer in the sample. The inverse Fourier transform converts the data from wavenumber to spatial depth. The cosine functions with frequency proportional to object depth become a pair of delta functions (positive and negative) with distance from the origin (zero OPD) proportional to the cosine frequency. This creates mirrored images of the sample on either side of the origin. In this configuration only the positive data is meaningful and the negative data can be ignored. Thus the inverse Fourier transform of the spectrally encoded data provides the spatial location of each scattering object in the sample.

Although this description conveys the general concept in lieu of a detailed mathematical derivation, there are a few additional complexities of the derivation worth addressing. The detected interference pattern has additional contributions in addition to the cosine functions from each scatterer. The sum of all reflections from the reference and sample arm contribute a constant bias to the detected signal. Additionally, low frequency cosine interference patterns are generated for any two scatterers separated by less than the source coherence length. Finally, these two terms as well as the desirable cosine terms are all multiplied by the spectrum of the source. After taking the inverse Fourier transform the constant bias becomes an undesired DC term at zero OPD. The low frequency cosine functions become delta functions near zero OPD. Finally, all terms are convolved with the Fourier transform of source spectrum which by definition is the source coherence function. The undesirable DC term and low frequency artifacts can be removed by high pass filtering. At the location of each delta function is now a copy of the coherence function which by definition has a FWHM of one coherence length. Although mathematically derived via different image reconstruction techniques, the coherence length defines the axial resolution in both TD-OCT and FD-OCT.

The interference pattern can be spectrally sampled either on the detection or source side. Detection side sampling is typically done by using a dispersive optical element such as a grating

to spectrally distribute the signal onto a line detector (CCD or CMOS). This approach is typically referred to as SD-OCT or spatially encoded frequency domain OCT. SD-OCT acquires the entire signal in a single exposure. Alternatively, a frequency scanning light source such as a swept source laser can be used. Swept source lasers have very small instantaneous bandwidth that sweeps through the lasers full bandwidth as a function of time with high frequency. This is known as SS-OCT or time encoded frequency domain OCT. In this configuration the detector is simply a photodiode as in TD-OCT as the complexity has largely been moved to the light source.

FD-OCT technique have major advantages in speed and sensitivity compared to TD-OCT. Standard TD-OCT systems with a single galvo mirror can typically acquire A-scans at a rate of less than 1 kHz. Commercial SD-OCT systems with acquisitions speeds in excess of 50 kHz are readily available. Commercial SS-OCT systems with speeds up to 200 kHz are readily available and some systems using state of the art Fourier domain mode locked lasers are now available operating at 1.5 MHz speeds allowing for video rate 3D imaging.

In TD-OCT reflected light from the entire imaging depth is incident on the detector and contributing to the noise, but only the light within a coherence length around the zero OPD location is contributing the signal. In contrast FD-OCT techniques use light from the entire sample to create the image. In theory the increased sensitivity scales with the number of resolved wavelength bands (pixels) used to sample the spectrally encoded interference signal⁶⁹. In practice the gains may be partially offset by reduced detector dynamic range and dispersive element aberrations in SD-OCT systems. In SS-OCT systems nonlinearities in wavelength and linewidth broadening when scanning at high frequencies may degrade imaging quality, offsetting some of the gains from increased sensitivity.

This summarizes the primary types of OCT architecture in terms how they generate an A-scan. The type of OCT system will determine the necessary type of detector and light source as well as establish general speed and sensitivity ranges. In order to build an endoscopic OCT system a few

additional system characteristics needs to be considered. The central wavelength and bandwidth of the source will determine the axial resolution. However, the light-tissue interactions are also essential to consider in choice of wavelength as this will impact penetration depth. The distal optics in the endoscope (sample arm) will determine lateral resolution and scanning geometry for image reconstruction.

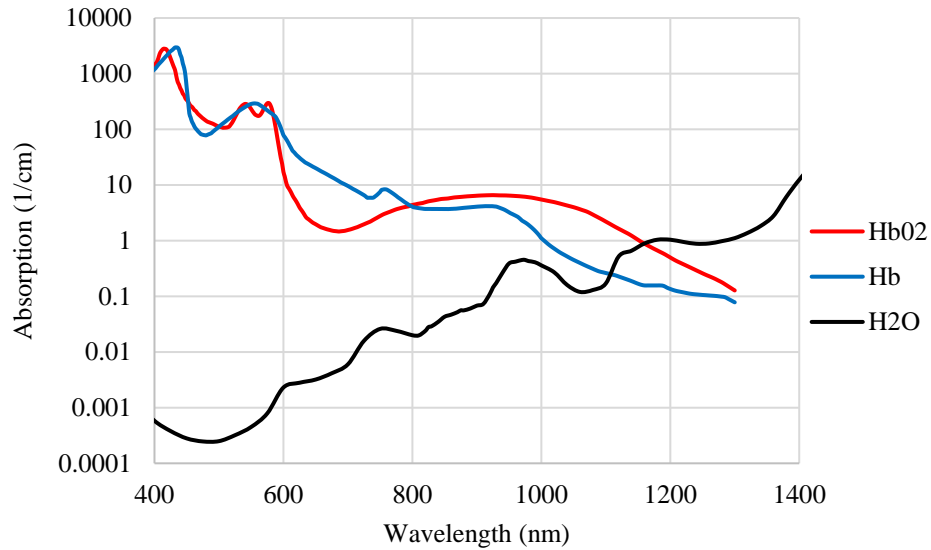


Figure 1.2: Coefficient of absorption (1/cm) as a function of wavelength for oxygenated hemoglobin (HbO₂), deoxygenated hemoglobin (Hb) and water (H₂O). Data⁷⁰.

1.3.5. Light-Tissue Interaction

For biological tissue OCT systems typically use wavelengths in the near IR. In order to create an interference pattern, photons must penetrate the sample, reflect off an index of refraction change in the tissue, exit the sample and return through the optical path with sufficient power to create a detectable interference pattern. The sample has wavelength dependent absorption and scattering properties that attenuate the optical power as a function of penetration depth. The coefficients for tissue are a compilation of the components that make up the tissue including hemoglobin, water, fat and collagen. Water and hemoglobin absorption are primary attenuators in

biological tissue (Figure 1.2). OCT systems designed to image biological samples commonly operate in the near IR range between 800 and 1400 nm. This range provides a good balance between the high absorption of blood in the visible spectrum and high absorption of water farther into the infrared. Imaging depths of 1-2 mm in tissue is typical. Another factor influenced by wavelength choice is resolution. In general systems with shorter wavelengths have better resolutions at the cost of reduced penetration depth.

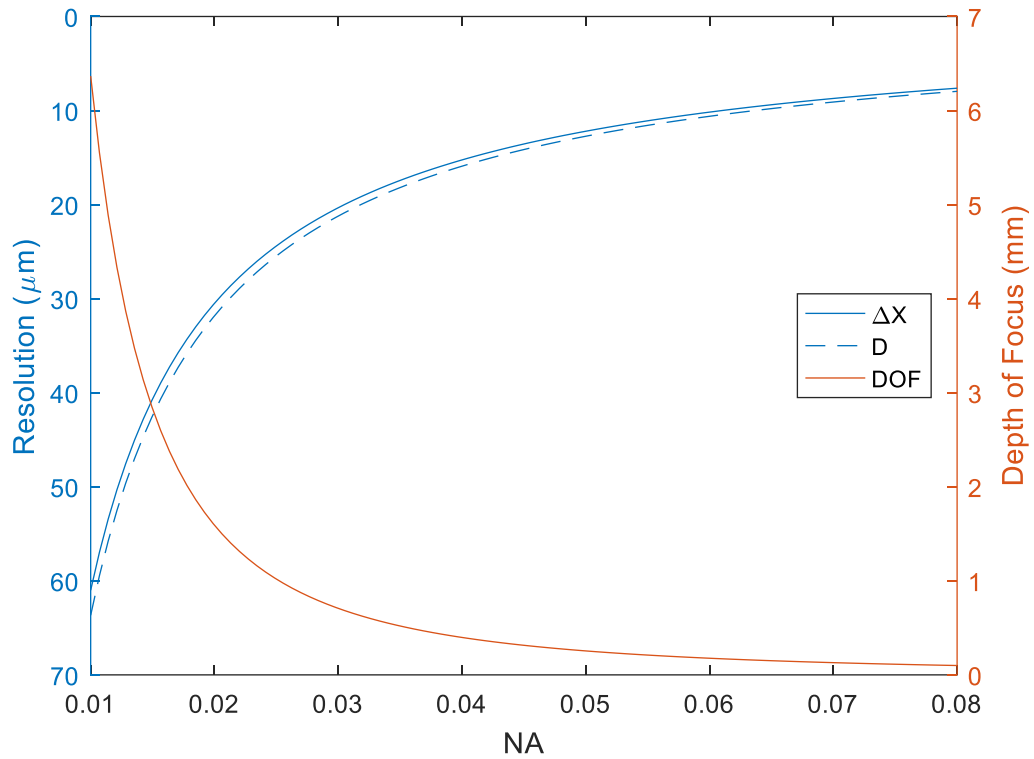


Figure 1.3: Δx , D and DOF as functions of NA for a wavelength of 1 micron in air. Although derived from different physical phenomena, in practice Δx and D both give sufficiently accurate resolution approximation for OCT design.

1.3.6. Lateral Resolution and Depth of Field

The distal optical design will determine, lateral resolution, depth of field and scanning geometry. Axial and lateral resolution are decoupled for OCT with lateral resolution determined by the distal focusing optics. There is a fundamental tradeoff between increased resolution and decreased depth of field. For a diffraction limited system the Rayleigh resolution is given by:

$$\Delta x = \frac{0.61\lambda_0}{NA}$$

In general OCT focusing optics are low NA and are approximately monochromatic making first order modeling sufficient. A useful modeling technique to design endoscopic OCT focusing optics is to use Gaussian beams⁷¹. The sample arm connecting the proximal system to the distal objective is typically a single mode fiber. The output of the single mode fiber can be approximated as a Gaussian beam with beam waist, ω_0 , equal to half the mode field diameter of the fiber. A Gaussian beam can be completely described by a complex beam parameter as a function of the optical axis, z , denoted by $q(z)$:

$$\frac{1}{q(z)} = \frac{1}{R(z)} - i \frac{\lambda_0}{\pi n \omega(z)^2}$$

$R(z)$ is the radius of curvature and $\omega(z)$ is the beam radius with the beam waist (minimum radius) located at the origin. The advantage of using the q parameter is that it can be used with ray transfer matrices (ABCD matrices). Each optical element alters the q parameter, effectively creating a new Gaussian beam. By transferring the q parameter through each optical element the final output Gaussian beam of the optical system provides the focal location, resolution and depth of field. The focal location determined by the new beam waist location with resolution, D , being twice the diameter of the beam waist at focus (the beam waist size is defined by amplitude falloff to $1/e$ of the maximum). The depth of field is twice the Rayleigh range and determines the range over which near diffraction limited imaging occurs. Assuming the small values of NA typically used in OCT the beam diameter and depth of field are approximately (Figure 1.3):

$$D = 2 * \omega_0 \approx \frac{2\lambda}{\pi NA}$$

$$DOF = 2 * Z_r \approx \frac{2\lambda}{\pi (NA)^2}$$

In the case of ovarian cancer screening the deadliest cancers are thought to develop in the epithelium which is the outermost 100-micron layer of tissue. Assuming a 1-micron wavelength

and NA of 0.065 the Gaussian beam diameter is approximately 9.8 microns with a depth of field of 150 microns. For an endoscope designed to image while in contact with the tissue the beam waist can be designed to be 75 microns outside of the endoscope so that any tissue from in contact to 150 microns away is imaged with high resolution. This should provide high resolution throughout the epithelial layer including any thickening associate with precursor legions. Tissue beyond 150 microns would still be imaged with increasingly poor resolution until the beam divergence, tissue scattering and tissue absorption attenuate the signal to noise levels. Figure 1.4 shows an example of a purely fiber based focusing system with these parameters.

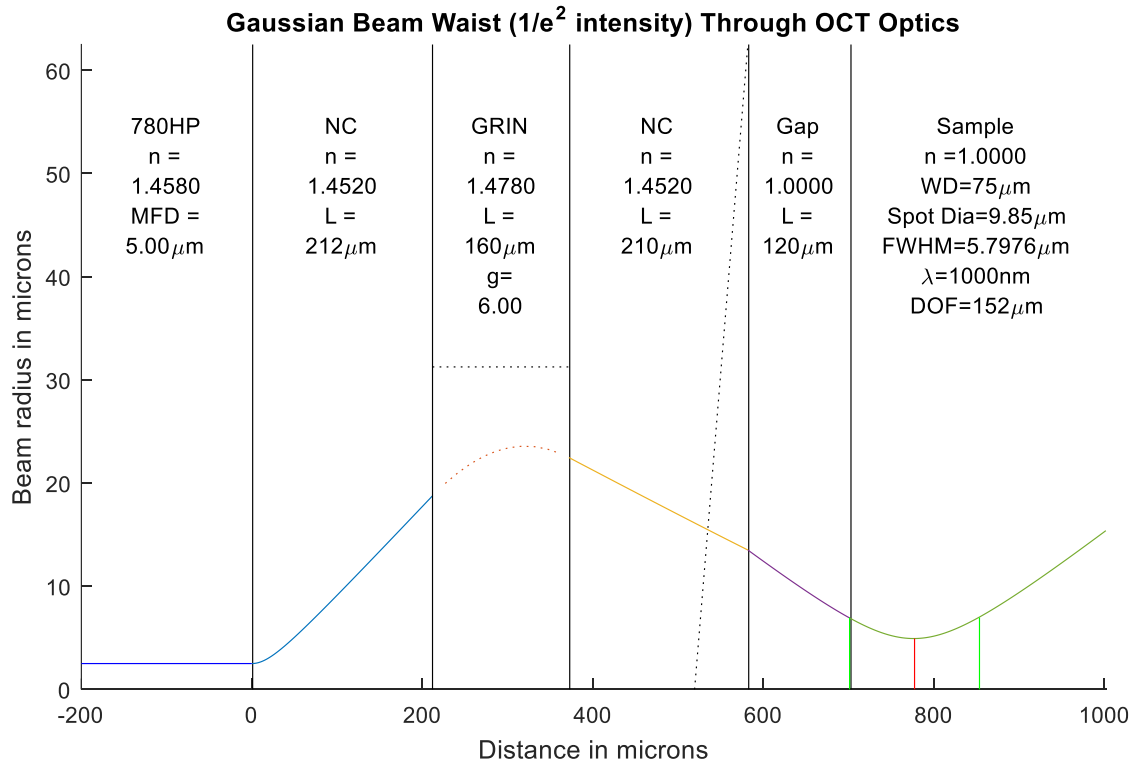


Figure 1.4: Example of Gaussian beam distal OCT modeling. Beam originates from the output of a single mode 780HP fiber and then propagates through no-core fiber (large core multimode), gradient index fiber with limited aperture (dashed horizontal line), another no-core fiber section with reflective angle polish (dashed diagonal line), a gap between output of the fiber and edge of the endoscope, and finally into the sample. Each optical interface changes the q parameters which then remains constant during propagation to the next interface except inside of the GRIN fiber in which q parameter changes continuously during propagation.

1.3.7. Scanning Geometry

The distal optical design also determines scanning geometry. All parameters discussed this far are primarily in the context of acquiring each A-scan. Each A-scan is only a single depth profile of the tissue. In order to generate an image, the OCT beam must be scanned relative to the sample. By scanning the focused beam of the sample arm in a direction orthogonal to the optical axis a 2D depth slice of the sample can be created known as a B-scan. By additionally scanning in a third axis orthogonal to both the optical axis and B-scan axis a 3D volume can be reconstructed (C-scan). The limited size of endoscopes can make implementing scanning mechanisms challenging. Choice of scanning mechanism will depend on whether the endoscope is forward- or side-viewing.

Forward viewing endoscopes are useful for investigating tissue located in front of the endoscope. Depending on angle of approach this could include imaging the ovary. Scanning mechanisms for forward-viewing endoscopes most commonly are paired angle rotation scanning (PARS), microelectromechanical scanners (MEMS) mirrors and scanning fiber endoscopes (SFE).

PARS is a technique that uses two GRIN lenses separated by an air space. The surfaces of the GRIN lenses facing each other are polished to with equivalent angles. If each lens is rotated in opposite directions at the same speed the beam will perform a fan sweep in the tissue^{72,73}. Each sweep images a B-scan. The smallest implementation of this approach has been demonstrated in a needle probe with outer diameter of 820 microns (21 gauge needle)⁷³. The technique can be expanded for volumetric C-scan imaging. Changing the relative offset in angle between the two GRIN lenses will change the orientation of the fan sweep in discrete steps. Alternatively, a small offset in rotational velocity between the two lenses will continuously rotate the sweep orientation. Full field of view (FFOV) of demonstrated probes has been 30-40 degrees and lateral resolution degrades as field angle increases.

MEMS mirrors are a pair of very small tip and tilt mirrors that provide raster scanning. MEMS devices typically have a footprint of 1 mm x 1 mm and have been demonstrated for OCT scanning in forward viewing endoscopes with diameters as small as 2.8 mm⁷⁴⁻⁷⁹. MEMS based OCT endoscopes typically achieve FFOV in each scanning axis of at least 40 degrees. MEMS mirrors offer additional capabilities such as dynamic focus tracking^{77,80}, but barring further miniaturization are not suitable for endoscopes with diameter less than a few millimeters.

SFE makes use of the mechanical resonance frequency of a fiber for scanning. A fiber is placed inside a quartered piezo electric tube with the fiber fixed to one end of the piezo tube. A cantilevered length of fiber then extends from the fixed location. The fiber can be oscillated by driving a voltage across one axis of the piezo tube at the mechanical resonance frequency of the fiber⁸¹. Since the quartered piezo tube has two axes the oscillation frequencies sent to each axis can be independently controlled to create scanning geometries. Two sinusoidal waves with 90-degree phase offset and equal amplitude will cause the fiber tip to oscillate in circle. By scanning the amplitude, a spiral scan pattern can be generated. Spiral scanning has been demonstrated for use in forward viewing OCT endoscopes^{82,83}. Lissajous trajectories have also been demonstrated which allow full-field sampling with increased spatial sampling as a function of time⁸⁴. In order to create Lissajous patterns the resonant frequency in each axis must be differentiated which can be done by adding an asymmetrical weight to the tip of the fiber. SFE based designs have been demonstrated in endoscopes with outer diameter as small as 1.2 mm. The technology is particularly appealing as it can be adapted for single-channel multi-modality imaging.

For endoscopes designed to pass through and image a tubal wall a side-viewing approach is preferred. For example, imaging the epithelium of the fallopian tube wall is ideally performed by side-viewing. For side-viewing geometries the scanning axes can typically be decomposed into as rotational and a longitudinal. The simplest approach is to display A-scans as a function of time and manually generate a B-scan by pulling back or rotating the endoscope. Automated scanning

provides a consistent image with known sampling density designed to ensure that features necessary for diagnosis are not missed.

Rigid needle probes using an all fiber based optical design similar to the one shown in Figure 1.4 have been demonstrated with outer diameter of just 0.31 mm⁸⁵. The small rigid probe can easily be rotated 360 degrees to create a circular B-scan. Then the probe can be longitudinally pulled back between B-scans to create a cylindrical C-scan for 3D volume image reconstruction. Alternate scans rotate in opposite directions to avoid damaging the fibers. For larger endoscopes friction between the endoscope and tissue may prevent rapid rotation of the entire endoscope. This can be solved by having a protective exterior layer of the endoscope that remains stationary while the interior optics translate or rotate. The rotate, translate, counter-rotate scanning geometry is still applicable. Alternately, some endoscopes translate to generate the B-scan, perform a small rotation and then repeat the translation⁸⁶. The decision of scanning geometry should depend on whether a circular B-scan or longitudinally translated B-scan is more diagnostically useful to the application. In either approach care must be taken to alternate rotation direction between full rotations in order to prevent damage to the fiber. Helical or spiral scanning is possible by adding hardware to overcome the issue of twisting the proximal fibers.

If 3D volume scanning is critical then spiral scanning is an ideal geometry to provide Nyquist sampling of the tubal wall. In order to perform spiral scanning the system must continuously rotate the beam while being slowly translated through the sample. One approach to avoid damaging the fiber is to place a fiber optics rotary joint in the proximal end of the sample arm. This allows the sample arm distal of the joint to freely rotate inside the endoscope while leaving the fiber on the proximal side of the joint stationary⁸⁷. A second approach is to attach the angle mirror or prism that deviates the OCT beam to a micromotor placed in the distal tip of the endoscope⁸⁸. This has the advantage of isolating the rotation from the fiber and focusing optics,

but requires slightly larger diameter (~ 3 mm) and the electronic connections to the motor may obscure the beam over a partial angle range of the full rotation.

1.3.8. Fiber-based Implementation

The interferometry setup for endoscopic OCT is typically fiber based. Using fibers instead of free space optics can make the system small, robust and portable. The sample arm is effectively the endoscope. Interchanging the endoscope for one with the same scanning geometry simply requires realigning the sample arm and reference arm path lengths to the zero OPD location. Inserting a new endoscope with a different scanning geometry is more complicated and may require altering the software acquisition settings and imaging processing. A fiber based interferometer requires additional dispersion and polarization correction compared to a free space system. Light traveling through a fiber experiences dispersion from the wavelength dependent index of refraction of the fiber core. Dispersion must be corrected to maintain axial resolution and can be corrected with an adjustable dispersive prism in the reference arm or with software during imaging processing⁸⁷. The orientation of the light source polarization may not be maintained by the fibers. Maximum interference visibility requires the sample and reference arm polarizations to match. Polarization paddles can be added to one of the arms in order to correct the mismatch.

1.4 Multispectral Fluorescence Imaging

The phenomenon of fluorescence was initially discovered by Stokes in 1852⁸⁹ and first applied to the biomedical field in 1911⁹⁰. For over 50 years fluorescence imaging has been studied in numerous forms for diagnostic applicability to a wide variety of cancers. The fluorescence process occurs when a molecule enters an excited state after absorbing an excitation photon and then emits a lower energy (longer wavelength) photon while returning to the ground state. Molecules exhibiting this characteristic are known as fluorophores and can be organic or inorganic. Each fluorophore has specific excitation and emission wavelength spectra. By imaging a tissue sample with the proper illumination wavelength and emission filters information about the tissues biochemical composition can be obtained. Fluorescence imaging can target changes in fluorophores associated with changes in tissue state due to disease state. Fluorescence imaging can be implemented in a wide variety of configurations. For endoscopic imaging a wide-field of view fluorescence imaging channel can provide navigation with high sensitivity to abnormal fluorescence signals.

1.4.1. Fluorescence Process

The creation of light fundamentally requires accelerating charge. Thermal radiation such as from the sun or an incandescent light bulb is generated by thermal motion of charged particles. Light emission generated by non-thermal processes such as chemical reactions or electrical energy is known as luminescence. Fluorescence is a type of luminescence in which the absorption of photons by a molecule causes some of its electrons to briefly enter an excited state. As the photon relaxes back to the ground state some of the energy is lost as emission of a lower energy photon.

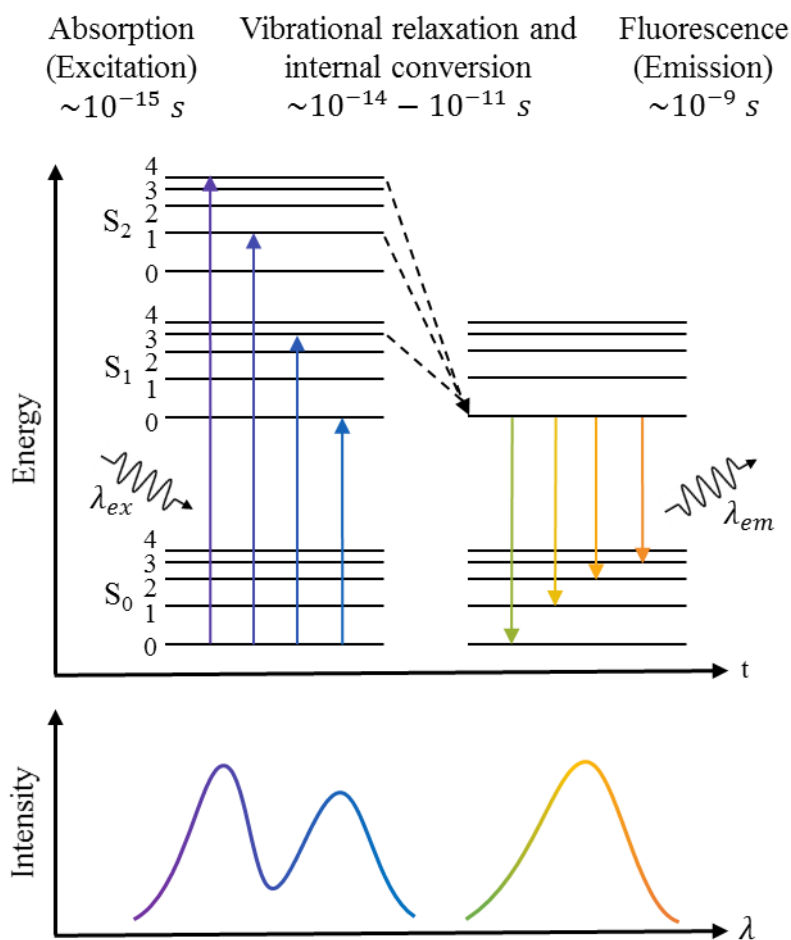


Figure 1.5: Jablonski energy diagram of the fluorescence process in a fluorophore with two excitation peaks and one emission peak. S_0 is the ground state of the electrons on the molecule. Absorption of particular wavelengths excite the electron into an excited state, S_1 or S_2 . Each excited state has multiple energy levels corresponding to different vibrational states. After initial excitation non-radiative decay initially reduces the energy level of the electron. The radiative decrease to the ground state releases a photon of lesser energy than the absorbed photon. Each fluorophore has unique wavelength dependent absorption and emission spectra represented at the bottom section of the figure.

The fluorescence process is often described with a Jablonski energy diagram (Figure 1.5). The ground state of the electrons is denoted S_0 and successively higher energy states are denoted S_1 , S_2 , etc. Each energy state has sublevels associated with different vibrational states of the electron. Depending on the molecular structure certain wavelength photons are more likely to be absorbed. As shown in Figure 1.5 it is possible to have multiple absorption peaks associated with different absorption levels. The absorption process happens on the order of 10^{-15} s and typically the

electron incurs both electrical and vibrational excitation. Vibrational relaxation happens prior to electronic relaxation and occurs on the order of 10^{-14} - 10^{-11} s. The vibrational relaxation energy is a non-radiative energy transfer such as heat dissipation. Electronic relaxation then results in the emission of a photon with lower energy than the one absorbed. Electronic relaxation can be to different vibrational sublevels of the ground state. The possible relaxation energy changes and the associated probability of each determines the emission spectrum associated with each excitation wavelength. During fluorescence imaging not all photons will be absorbed and not all absorbed photons will result in radiative decay (fluorescence). The ratio of emitted to absorbed photons is known as the quantum yield and is wavelength dependent.

1.4.2. Intrinsic vs. Extrinsic Fluorescence

A primary distinction in imaging fluorophores in biological tissue is the use of intrinsic or extrinsic fluorophores. Intrinsic fluorophores are naturally occurring in the tissue such as tryptophan, collagen, elastin, FAD, NADH, and porphyrins⁹¹. These are often also referred to as endogenous fluorophores and the fluorescence they generate is more specifically called autofluorescence. Alternatively, a marker ligand with a known fluorophore attached can be used as a dye. The ligand is designed to target specific receptors in tissue associated with disease state and the fluorophore is used to image location of the drug. Or, a non-targeted fluorophore can be administered, which may have selective uptake in various tissue types or cellular/extracellular components due to the chemical properties of the fluorophore. This type of dye is an extrinsic or exogenous fluorophore.

Endogenous fluorophores typically have peak excitation wavelengths in the UV and blue spectrum and emission intensity may be 5 or 6 orders of magnitude below reflected excitation intensity. High quality dichroic and blocking filters are necessary for good signal-to-background ratio and a high sensitivity, low noise detector is required for good SNR. The endogenous

fluorophores also typically have some overlap in excitation and emission spectrum so the detected signal may be a combination of fluorophores.

Exogenous fluorophores are specifically chosen or designed for their task. As such they overcome many of the challenges of endogenous fluorophores. Excitation wavelengths avoid the complications of UV in favor of common laser lines in the green and red spectrum. Multiple fluorophores can be used with well differentiated signals to simultaneously image different specific targets. Quantum efficiency and thus signal are higher. Well-designed tracers may also more specifically target the region of interest. However, the need to administer the tracer presents a major hurdle. A tracer will be considered as a drug, and any new drug or new use for an existing drug requires significant proof of safety for FDA approval. Even use of an approved drug complicates an *in vivo* imaging procedure by requiring the drugs administration, waiting for it to go into effect and then flushing the drug if necessary. Extrinsic dyes for *ex vivo* studies are a powerful tool, but for *in vivo* imaging the use of endogenous fluorophores is strongly preferred.

Changes in tissue pathology can alter an autofluorescence signal in a variety of ways. For example, the concentration of certain fluorophores may be different in a cancerous lesion compared to surrounding tissue resulting in a change in the total fluorescence signal from each region. Alternatively, the fluorescence properties of individual fluorophores may be altered due to changes in the microenvironment surrounding the fluorophore^{92,93}. Changes in optical properties could include excitation spectrum, emission spectrum, or fluorescence lifetime (average time between excitation and emission). Understanding how the change in pathology alters the fluorophores is important in designing a system to measure the most diagnostically useful parameter of the fluorescence signal. An additional complication is that the optical absorption and scattering properties of the tissue surrounding the fluorophores may change as a function of pathology. Since the fluorescence signal must pass through the surrounding tissue, changes in

optical properties of the tissue alter the fluorescence signal. This effect makes the recorded signal highly dependent on the illumination and imaging geometries⁹⁴⁻⁹⁶.

1.4.3. Fluorescence Imaging Systems

A fluorescence imaging system must consider spatial, spectral and temporal resolution. Point probes measure fluorescence at a single spatial location and can easily be implemented using small fiber optics for integration into very small probes. Since only one spatial coordinate is considered the detector can be a spectrometer with high spectral detection resolution or an extremely fast detector for fluorescence lifetime measurements. Adding a tunable light source or multi-wavelength illumination source can also be done in order to increase excitation spectral resolution. In order to provide imaging over a larger field of view the system must be capable of recording fluorescence from multiple spatial pixels.

Wide field imaging can be achieved using a scanning system or a 2D detector. Scanning confocal microscopy has been integrated into a laparoscope for ovarian cancer imaging with high spatial resolution and small field of view³⁰⁻³³. Fiber scanning piezo tubes could also be used for large field of view endoscopic MFI imaging. To date a visible reflectance fiber scanning endoscope has been used to acquire a proof-of-concept fluorescence image⁸¹, but no MFI specific implementation of a scanning fiber endoscope has been developed. Photodiodes or single point detectors used in scanning systems typically have superior properties compared to 2D detectors. However, in order to generate an image with N pixels in T seconds a single detector is limited to exposure time of T/N seconds per pixel which negates some of the inherent advantages. For the same image using a 2D detector all pixels can use the full exposure time T . Cooled charged-coupled devices (CCD) are a typical 2D detector for fluorescence imaging as they have low noise, high sensitivity and can often provide quantitatively repeatable measurements. Near real-time endoscopic 2D fluorescence lifetime imaging has been demonstrated, but implementation is still

complex and total pixel count is limited⁹⁷. An effective approach to diagnostically differentiating multi-component fluorescence signals is to use MFI.

MFI requires an illumination system with multiple excitation wavelengths and detection of multiple emission bands for increased spectral information at each spatial location. The illumination system can be a broadband light source with tunable filters used to select the excitation band. The filters must have high out-of-band suppression in order to maintain a high signal-to-background ratio for detection of the fluorescence signal. Alternately, multiple narrowband sources such as lasers or LED's can be used. Using mechanical shutters or high speed electronic switching the sources can be sequentially scanned or combined as desired.

Detection must also be capable of selecting emission bands. This can be achieved with a single detector and a high-speed filter wheel. Alternately the spectral bands can be spatially separated and imaged on multiple detectors or different regions of a single detector. Simultaneous detection is less flexible for prototyping and generally more expensive to implement. With known emission bands based on prototype data a simultaneous collection system is more desirable. Acquisition time is decreased and tissue motion between sequentially acquired spectral images is eliminated. In terms of implementation into an endoscope the multispectral illumination and detection systems primarily impact the proximal optical design. The fiber optics connecting the proximal and distal systems must be chosen to transmit the necessary wavelengths. Coherent imaging fiber bundles with small core-to-core spacing necessary for reasonable resolution attenuate strongly in the UV spectrum. Chromatic aberrations of the distal imaging optics become increasingly important as the total detection wavelength range increases. In general, the distal illumination and imaging optics are not significantly different than a wide-field of view white-light imaging endoscope. However, the inclusion of UV wavelengths for excitation or emission can severely limit optical material choices. The peak excitation of many endogenous fluorophores is in the UV spectrum, making inclusion of UV wavelengths at least for excitation highly desirable. Systems

using a coherent fiber bundle to relay the image from the distal optics to the proximal optics or scanning systems such as piezo scanning fiber systems are both suitable for wide-field fluorescence imaging.

CHAPTER 2: PRESENT STUDY

The present study validates MFI for ovarian cancer detection and presents optical designs for integrating MFI and OCT into miniature endoscopes for ovarian cancer screening. The contributions to the field of optical ovarian cancer screening are: 1) the validation of wide-field MFI imaging for diagnostic ovarian cancer imaging on *ex vivo* samples, 2) the optical design for a miniaturized wide-field MFI system for integration into a sub-millimeter diameter endoscope, and 3) the optical design of common path endoscopic lens system for forward viewing navigation and circle scanning side-viewing OCT. The methods, results and conclusions of each contribution are attached in the appendices.

1.1 *Ex vivo* wide-field MFI of human ovary and fallopian tube tissue

While OCT had been previously validated for *in vivo* endoscopic evaluation of ovarian cancer using a laparoscope²⁶, wide-field MFI need further study for application to ovarian cancer. Dr. Utzinger's lab had previously determined autofluorescence excitation-emission matrices for normal and cancerous ovarian tissue using a fiberoptic probe³⁹ and performed wide-field autofluorescence imaging with 365 nm excitation and eight emission bands⁴⁰. In addition, the lab developed an MFI system to study *ex vivo* surgical discard colon tissue with promising results for diagnostic imaging⁹⁸. In this study the previously developed *ex vivo* MFI system was used to image surgically discarded ovarian and fallopian tube tissue shortly after removal.

The project was highly collaborative. Tissue was received from consented patients undergoing an oophorectomy, hysterectomy or debulking surgery. Surgeries were performed by Dr. Setsuko Chambers and Dr. Kenneth Hatch. Contributing authors Koevary, Orsinger, Nymeyer and Welge consented patients and transported tissues from the surgical location to the MFI system location. Contributing author Baggett and myself acquired images on the MFI system. Using modified and newly developed MATLAB scripts I processed all images and extracted normalized fluorescence

data for every tissue sample. I collaborated with contributing authors Dr. Roe and Saboda from the biostatistics shared service to perform statistical logistic regression analysis on the fluorescence data. In addition, I performed statistical analysis using MATLAB (scripts in appendix A) on the data using the statistical methods of principle component analysis, mahalanobis distance and linear and quadratic discriminant analysis. The published paper includes the results from the logistic regression and quadratic discriminant analysis.

Results indicated MFI is a promising approach to wide-field navigational imaging with ability to discriminate between cancer and non-cancerous ovarian and fallopian tube tissue. All excitation and emission combinations except 280 nm excitation showed statistically significant intensity difference between cancer and non-cancerous samples. The increased absorption associated with angiogenesis in tumor locations appeared to be a strong contributor to decreased fluorescence in cancerous samples. The *ex vivo* system allows for reasonable normalization of intensity of each image type for comparison between samples as all imaging parameters are monitored and controlled. Use of the technique for endoscopic *in vivo* imaging will require alternate image normalization techniques for comparison of relative fluorescence between tissue locations. Future work on the ovarian and fallopian tube images should include evaluation of ratiometric image combinations similar to those done on colon tissue⁹⁸. The ratiometric image combination technique provides some image relative normalization and is easily applied for *in vivo* imaging.

1.2 Dual Modality Falloposcope

This project involved the miniaturization and integration of OCT and MFI into an 800 micron diameter endoscope prototype. As discussed in the introduction there are three approaches for endoscopic evaluation of the ovary and fallopian tubes. The most invasive approach is via a laparoscope and has been used to validate advanced imaging techniques for ovarian cancer detection, but is too invasive to be a regular screening procedure. The two transvaginal approaches are more suitable for a screening procedure. One transvaginal approach is to access the ovary and distal fallopian tube via a small incision in the vaginal wall. This allows for an endoscope with diameter of a few millimeters, but only accesses the distal region of the fallopian tube. The second transvaginal approach is to access the ovary through the natural pathway of the vagina, uterus and fallopian tube. The proximal tubal opening of the fallopian tube is located in the uterus with an ostium diameter of approximately 1 mm²⁵. An endoscopes designed for this approach, or falloposcope, has the ability to fully interrogate the fallopian tube, but requires a sub millimeter diameter. The goal of this project was to build a proof of concept falloposcope to validate the feasibility of dual-modality screening via the natural pathway approach.

The dual-modality OCT and MFI falloposcope is 800 microns in diameter, highly flexible and steerable. The highly collaborative project required significant optical, mechanical and optomechanical design. The investigators Dr. Barton, Dr. Utzinger and Dr. Black led the project with significant experience in endoscope and catheter design, fluorescence and OCT imaging of cancer, and laser design. Dr. Keenan's graduate work focused on the mechanical specification and integration of the optical systems as well as the mechanical and material design of the endoscope in order to achieve desired flexibility and steering⁹⁹. My work largely focused on the optical design of the endoscope with particular emphasis on the adaptation of MFI for endoscopic use.

The endoscope has six optical subsystems, 3 distal and 3 proximal, each with independent and interrelated design criteria¹⁰⁰. Each proximal optical system is connected to a corresponding distal system by optical fiber. Thus there are three optical fibers inside of the endoscope connecting the distal and proximal optical systems. OCT performs illumination and imaging both via the same sample arm and distal optical design and thus requires only one single mode fiber connected the distal and proximal systems. Interference and image processing is performed in the proximal system. The proximal OCT system for the falloposcope was adapted from an existing system. The purely fiber based focusing optics for the distal OCT was based on recent ultrathin OCT needle probes⁸⁵. I developed MATLAB scripts to model the beam propagation through the fiber based focusing system as a Gaussian beam. Dr. Keenan used the Gaussian beam propagation model to determine fiber specifications and then built and tested the distal OCT system to validate performance. Due to the extreme size constraints of the falloposcope, the OCT system does not include automated scanning.

The MFI system requires separate illumination and imaging channels in order to separate illumination and imaging signals. Each of the four MFI optical subsystems were based on the *ex vivo* system, but completely redesigned for endoscopic use. The submitted manuscript describing the new endoscopic MFI system with 300-micron diameter imaging elements and a 125-micron illumination fiber suitable for integration into ultra-miniature endoscopes attached in appendix B.

Overall the falloposcope project proves the feasibility of building a dual modality endoscope with the optical and physical specification necessary for fallopian tube screening. The University of Arizona has a patent pending covering the technology¹⁰¹. The promising technology will require industry support to transition from a proof-of-concept device to a portable, robust and automated clinical device.

1.3 Single Lens System for Forward Viewing Navigation and Scanning Side-Viewing OCT

The extremely limited size of the falloposcope is necessary for full fallopian tube screening, but also limits optical imaging functionality. The OCT system lacks scanning and the MFI imaging has limited pixels. The alternate transvaginal screening approach of introducing the endoscope through a small incision in the vaginal wall allows for endoscopes with diameter on the order of 3 mm. While the design from the falloposcope could scale for increased MFI imaging resolution, the larger size allows for alternate optical design approaches integrating OCT and MFI illumination into a single path to enable both increased MFI resolution and OCT scanning.

Using a piezo scanning fiber endoscope (SFE) design instead of a coherent imaging fiber bundle allows the OCT path and navigational illumination path to be combined into a more space efficient single path. SFE uses a piezo tube to vibrate a fiber at its resonance frequency in two axes in order to scan the fiber in a known pattern. Collecting light as the illumination fiber scans the sample allows the image to be digitally reconstructed. To date the smallest demonstrated scanning fiber endoscope is 1.2 mm diameter which is too large for the proximal fallopian tube, but sufficiently small for a transvaginal endoscope. Scanning fiber endoscopes have been used for forward-viewing navigation with white-light⁸¹ and forward-viewing OCT^{83,84} independently. The possibility adding fluorescence imaging capabilities necessary for MFI has been demonstrated, but not fully implemented⁸¹. The dual modality combination of OCT with white-light or fluorescence navigation has not yet been done in a fiber scanning endoscope. OCT implementations have all been forward-viewing. For many tubal imaging applications side-viewing OCT preferable.

A novel endoscopic lens design is described in detail (appendix C) allowing for a combined forward viewing navigation and side-viewing OCT with scanning. Standard side-viewing endoscopes use a flat prism or mirror to deviate the beam. The mirror may rotate for

scanning, but is fundamentally not a rotationally symmetric element. For an SFE a rotational symmetric optic is desired that focuses the beam out the side of the endoscope as the OCT fiber scans in a circle of a known radius. I modeled a novel cover plate that achieves this rotationally symmetric beam deviation using a double reflection. Scanning the fiber in a circle at the designed radius causes the OCT beam to rotate around the endoscope. Smaller radial fiber deviations are focused in front of the endoscope for the forward-viewing navigation. The navigation channel presented is for white-light, but could easily be adapted for MFI. The novel lens design is ideal for applications needing forward viewing navigation through a tube while performing high resolution depth imaging of the tubal wall. This includes the fallopian tube as well as other body lumens such as the biliary ducts.

CHAPTER 3: FUTURE WORK

The ultimate goal of this field of research is the development of an effective method for ovarian cancer screening. Each of the three projects presented in this dissertation advance the scientific body of knowledge necessary to achieve that goal. However, significant future work remains both in terms of follow-up research on the presented projects as well as for the field as a whole.

3.1 Ex vivo MFI imaging study

This work builds on previous studies of ovarian fluorescence imaging conducted by the Utzinger lab and others. It continues to show the promise of fluorescence imaging for wide-field diagnostic imaging, but with multiple excitation and emission wavelengths using MFI. Endoscopic implementation as is done in the falloposcope is the clear next step. While the falloposcope validates that an imaging system with MFI capabilities can be implemented in an extremely small form factor, more work is needed to validate the utility of MFI *in vivo*. Wide-field fluorescence imaging is dependent on illumination and collection geometry. Any implementation including the falloposcope needs to validate the *ex vivo* results translate to *in vivo* imaging.

In the *ex vivo* study the data are quantitative because all system parameters are measured during each imaging acquisition sequence and the resulting images are normalized to system fluctuations. Extensive calibration is not realistic for clinical application *in vivo*. Rather than comparing absolute fluorescence signals it is more practical to compare relative fluorescence signals. This can be accomplished using ratiometric imaging as has been previously done on colon tissue with the *ex vivo* system⁹⁸. The absolute fluorescence data used in this study should be used to develop ideal ratiometric imaging combination for ovarian tissue. This will ultimately be more useful to compare and validate *in vivo* imaging results against.

3.2 Falloposcope Project

The falloposcope project successfully validated that dual modality imaging could be integrated into a sub millimeter package. The proof-of-concept design needs a few iterations of revisions to be made ready for clinical trials. In general, the revisions need to focus on simplifying and automating the construction and imaging as well as making the proximal systems robust and portable for integration into a surgical cart.

Currently each MFI image is sequentially acquired by manually adjusting the filters, illumination wavelength and exposure times. There are no hardware limitations to automating this process. A unified software package needs development to communicate with each piece of hardware and automate the process. Once the ideal illumination and imaging wavelength combinations are determined a potential hardware upgrade is a multispectral detector system to acquire all fluorescence and reflectance signals simultaneously. Simultaneous acquisition combined with a unified software package would drastically simplify operation and improve imaging speed.

For clinical use the entire proximal system must fit onto a surgical cart. The current proximal MFI illumination and imaging systems would need to be replaced with more robust and portable components. In particular, the alexandrite laser will likely need to be replaced with a compact diode laser or LED source.

For mass production the construction process of the distal tip would need to be automated to increase alignment capabilities and yield. Construction by hand is tedious and components are to easily damaged or lost.

None of these future changes are fundamentally limited by the general design. In general, they simply require the transition of the technology to a company with the funds and resources to drive the technology forward. The technology has been patented by the University and work to find a company to license and develop the technology is ongoing.

3.3 Single lens, multipath optical design for multimodal endoscopy

The majority of the modeling for this project has been completed. A few details in terms of specific components and design remain. Much of the remaining work is in building prototypes to validate design concepts and construction techniques. There will need to be an iterative process between prototype testing and updating the design in order to validate the technology. Ultimately the concepts used in the design need to be integrated into a prototype endoscope to prove the utility of the design.

Further research in the design approach may reveal very interesting applications and implementations. Each endoscopic image acquisition technology offers unique advantages. For purely white-light imaging the continued miniaturization of distal tip detectors may be simpler and more practical than scanning fiber endoscopes. However, scanning fiber technology offers significant advantage for multimodality endoscopes in both illumination and light collection.

Scanning the illumination fiber inherently requires only a single illumination fiber. A single mode fiber is often used because it is effective and simple. Using a dual-clad fiber could allow for use of the inner cladding as an additional illumination or collection channel. Custom multi-core fibers are also possible. A custom fabrication could allow multiple single- or multi- mode cores inside a single fiber to be scanned. On the proximal end each core could be separated and coupled into separate light sources or detectors. Single-mode cores typically only operate efficiently over a few hundred nanometer wavelength range. Combining multiple single mode cores into a single illumination fiber could allow for single-mode propagation over a wide spectral range from the near UV to the near IR with each core coupled to an independent light source. This possibility further enhances the options for multimodality imaging since many of the advanced imaging techniques require specific light sources.

The light collection configuration also provides increased flexibility when compared to distal detector of CFB endoscopes. The image is acquired with temporal rather than spatial sampling so

photomultiplier tubes or photodiodes can be used instead of a CCD or CMOS detector. For spectral imaging this allows for a series of filters and single point detectors to be used to acquire a multispectral data at every acquisition. Color imaging on a 2D detector typically is done using a pixel level color filter array such as a Bayer filter that reduces the sampling frequency of each color. Alternatively, time sequenced images can be acquired to avoid the reduction in sampling frequency, but at the increase of total image time and susceptibility to motion artifacts. Even if these issues could be overcome a distal detector is simply not compatible with scanning imaging techniques such as OCT, confocal and multiphoton. These imaging techniques are possible with a SF endoscope both in single and multimodality configurations.

By designing optical systems that have spatially or spectrally differentiated optical properties, scanning fiber technology allows combination of advanced optical imaging techniques in novel configurations. The DRCP design presented spatially separates two low NA techniques in OCT and monochromatic imaging. High NA imaging techniques such as confocal and multiphoton microscopy could also be used in place of or in addition to the existing imaging modalities. For example, it may be possible to expand the DRCP design presented with small FFOV, high-resolution forward-viewing multiphoton imaging. Further addition of UV and visible wavelengths to the navigational channel would allow for a quad modality endoscope with wide FFOV navigational white-light and multispectral fluorescence imaging, forward-viewing high resolution multiphoton imaging and high resolution side scanning OCT depth imaging. The DRCP presented here is meant as a first step into advanced multimodal scanning fiber endoscopes. As expertise in design and construction expands the future holds many possibilities for the technology.

REFERENCES

1. “Cancer Facts and Figures,” American Cancer Society, 2016, <<http://www.cancer.org/acs/groups/content/@research/documents/document/acspc-047079.pdf>> (accessed 23 September 2016).
2. S. S. Buys et al., “Ovarian cancer screening in the Prostate, Lung, Colorectal and Ovarian (PLCO) cancer screening trial: findings from the initial screen of a randomized trial,” *Am. J. Obstet. Gynecol.* **193**(5), 1630–1639 (2005) [doi:10.1016/j.ajog.2005.05.005].
3. I. J. Jacobs et al., “Ovarian cancer screening and mortality in the UK Collaborative Trial of Ovarian Cancer Screening (UKCTOCS): a randomised controlled trial,” *The Lancet* (2015) [doi:10.1016/S0140-6736(15)01224-6].
4. S. Vaughan et al., “Rethinking ovarian cancer: recommendations for improving outcomes,” *Nat. Rev. Cancer* **11**(10), 719–725 (2011) [doi:10.1038/nrc3144].
5. M.-C. King et al., “Breast and ovarian cancer risks due to inherited mutations in BRCA1 and BRCA2,” *Science* **302**(5645), 643–646 (2003) [doi:10.1126/science.1088759].
6. L. T. Shuster et al., “Prophylactic oophorectomy in pre-menopausal women and long term health - a review,” *Menopause Int.* **14**(3), 111–116 (2008) [doi:10.1258/mi.2008.008016].
7. W. H. Parker et al., “Long-term mortality associated with oophorectomy compared with ovarian conservation in the nurses’ health study,” *Obstet. Gynecol.* **121**(4), 709–716 (2013) [doi:10.1097/AOG.0b013e3182864350].
8. D. Hanahan and R. A. Weinberg, “The hallmarks of cancer,” *Cell* **100**(1), 57–70 (2000).
9. D. Hanahan and R. A. Weinberg, “Hallmarks of Cancer: The Next Generation,” *Cell* **144**(5), 646–674 (2011) [doi:10.1016/j.cell.2011.02.013].
10. A. M. Karst, K. Levanon, and R. Drapkin, “Modeling high-grade serous ovarian carcinogenesis from the fallopian tube,” *Proc. Natl. Acad. Sci. U. S. A.* **108**(18), 7547–7552 (2011) [doi:10.1073/pnas.1017300108].
11. A. M. Karst and R. Drapkin, “Ovarian Cancer Pathogenesis: A Model in Evolution,” *J. Oncol.* **2010**, e932371 (2009) [doi:10.1155/2010/932371].
12. I. Romero and R. C. Bast, “Minireview: Human Ovarian Cancer: Biology, Current Management, and Paths to Personalizing Therapy,” *Endocrinology* **153**(4), 1593–1602 (2012) [doi:10.1210/en.2011-2123].
13. R. J. Kurman and I.-M. Shih, “The origin and pathogenesis of epithelial ovarian cancer: a proposed unifying theory,” *Am. J. Surg. Pathol.* **34**(3), 433–443 (2010) [doi:10.1097/PAS.0b013e3181cf3d79].
14. R. S. Tuma, “Origin of ovarian cancer may have implications for screening,” *J. Natl. Cancer Inst.* **102**(1), 11–13 (2010) [doi:10.1093/jnci/djp495].
15. R. C. Bast, B. Hennessy, and G. B. Mills, “The biology of ovarian cancer: new opportunities for translation,” *Nat. Rev. Cancer* **9**(6), 415 (2009) [doi:10.1038/nrc2644].
16. E. Kuhn, R. J. Kurman, and I.-M. Shih, “Ovarian Cancer Is an Imported Disease: Fact or Fiction?,” *Curr. Obstet. Gynecol. Rep.* **1**(1), 1–9 (2012) [doi:10.1007/s13669-011-0004-1].
17. “Can ovarian cancer be found early?,” <<http://www.cancer.org/cancer/ovariancancer/detailedguide/ovarian-cancer-detection>> (accessed 27 October 2016).
18. D. Gupta and C. G. Lis, “Role of CA125 in predicting ovarian cancer survival - a review of the epidemiological literature,” *J. Ovarian Res.* **2**, 13 (2009) [doi:10.1186/1757-2215-2-13].
19. S. S. Buys et al., “Effect of screening on ovarian cancer mortality: the Prostate, Lung, Colorectal and Ovarian (PLCO) Cancer Screening Randomized Controlled Trial,” *JAMA J. Am. Med. Assoc.* **305**(22), 2295–2303 (2011) [doi:10.1001/jama.2011.766].

20. L. A. Beer et al., "Identification of multiple novel protein biomarkers shed by human serous ovarian tumors into the blood of immunocompromised mice and verified in patient sera," *PloS One* **8**(3), e60129 (2013) [doi:10.1371/journal.pone.0060129].
21. H.-Y. Tang et al., "A xenograft mouse model coupled with in-depth plasma proteome analysis facilitates identification of novel serum biomarkers for human ovarian cancer," *J. Proteome Res.* **11**(2), 678–691 (2012) [doi:10.1021/pr200603h].
22. E. V. Stevens, L. A. Liotta, and E. C. Kohn, "Proteomic analysis for early detection of ovarian cancer: a realistic approach?," *Int. J. Gynecol. Cancer Off. J. Int. Gynecol. Cancer Soc.* **13 Suppl 2**, 133–139 (2003).
23. E. Alvarez Moreno et al., "Role of New Functional MRI Techniques in the Diagnosis, Staging, and Followup of Gynecological Cancer: Comparison with PET-CT," *Radiol. Res. Pract.* **2012**, e219546 (2012) [doi:10.1155/2012/219546].
24. D. A. Fishman et al., "The role of ultrasound evaluation in the detection of early-stage epithelial ovarian cancer," *Am. J. Obstet. Gynecol.* **192**(4), 1214-1221-1222 (2005) [doi:10.1016/j.ajog.2005.01.041].
25. E. Lorenzen et al., "A review of the human vs. porcine female genital tract and associated immune system in the perspective of using minipigs as a model of human genital Chlamydia infection," *Vet. Res.* **46**, 116 (2015) [doi:10.1186/s13567-015-0241-9].
26. L. P. Hariri et al., "Laparoscopic optical coherence tomography imaging of human ovarian cancer," *Gynecol. Oncol.* **114**(2), 188–194 (2009) [doi:10.1016/j.ygyno.2009.05.014].
27. M. A. Brewer et al., "Imaging of the ovary," *Technol. Cancer Res. Treat.* **3**(6), 617–627 (2004).
28. T. Wang, M. Brewer, and Q. Zhu, "An overview of optical coherence tomography for ovarian tissue imaging and characterization," *Wiley Interdiscip. Rev. Nanomed. Nanobiotechnol.*, n/a-n/a (2014) [doi:10.1002/wnan.1306].
29. Y. Yang et al., "Integrated optical coherence tomography, ultrasound and photoacoustic imaging for ovarian tissue characterization," *Biomed. Opt. Express* **2**(9), 2551–2561 (2011) [doi:10.1364/BOE.2.002551].
30. A. A. Tanbakuchi et al., "Clinical confocal microlaparoscope for real-time in vivo optical biopsies," *J. Biomed. Opt.* **14**(4), 44030 (2009) [doi:10.1117/1.3207139].
31. T.-Y. Wu et al., "Confocal microlaparoscope for imaging the fallopian tube," *J. Biomed. Opt.* **19**(11), 116010 (2014) [doi:10.1117/1.JBO.19.11.116010].
32. Risi, Matthew D. et al., "Pilot Clinical Evaluation of a Confocal Microlaparoscope for Ovarian Cancer Detection," *Int. J. Gynecol. Cancer*.
33. A. A. Tanbakuchi et al., "In vivo imaging of ovarian tissue using a novel confocal microlaparoscope," *Am. J. Obstet. Gynecol.* **202**(1), 90.e1-9 (2010) [doi:10.1016/j.ajog.2009.07.027].
34. N. D. Kirkpatrick, M. A. Brewer, and U. Utzinger, "Endogenous Optical Biomarkers of Ovarian Cancer Evaluated with Multiphoton Microscopy," *Cancer Epidemiol. Biomarkers Prev.* **16**(10), 2048–2057 (2007) [doi:10.1158/1055-9965.EPI-07-0009].
35. J. Adur et al., "Optical biomarkers of serous and mucinous human ovarian tumor assessed with nonlinear optics microscopies," *PloS One* **7**(10), e47007 (2012) [doi:10.1371/journal.pone.0047007].
36. H. Li et al., "Utilizing spatial and spectral features of photoacoustic imaging for ovarian cancer detection and diagnosis," *J. Biomed. Opt.* **20**(1), 16002 (2015) [doi:10.1117/1.JBO.20.1.016002].
37. P. D. Kumavor et al., "Co-registered pulse-echo/photoacoustic transvaginal probe for real time imaging of ovarian tissue," *J. Biophotonics* **6**(6–7), 475–484 (2013) [doi:10.1002/jbio.201200163].

38. S. D. Kamath, S. Ray, and K. K. Mahato, "Photoacoustic spectroscopy of ovarian normal, benign, and malignant tissues: a pilot study," *J. Biomed. Opt.* **16**(6), 67001 (2011) [doi:10.1117/1.3583573].
39. R. George et al., "Parallel factor analysis of ovarian autofluorescence as a cancer diagnostic," *Lasers Surg. Med.* **44**(4), 282–295 (2012) [doi:10.1002/lsm.22014].
40. T. E. Renkoski, K. D. Hatch, and U. Utzinger, "Wide-field spectral imaging of human ovary autofluorescence and oncologic diagnosis via previously collected probe data," *J. Biomed. Opt.* **17**(3) (2012) [doi:10.1117/1.JBO.17.3.036003].
41. R. A. Bhat et al., "Autofluorescence of normal, benign, and malignant ovarian tissues: a pilot study," *Photomed. Laser Surg.* **27**(2), 325+ (2009).
42. C. J. Engelbrecht et al., "Ultra-compact fiber-optic two-photon microscope for functional fluorescence imaging in vivo," *Opt. Express* **16**(8), 5556 (2008) [doi:10.1364/OE.16.005556].
43. M. T. Myaing, D. J. MacDonald, and X. Li, "Fiber-optic scanning two-photon fluorescence endoscope," *Opt. Lett.* **31**(8), 1076 (2006) [doi:10.1364/OL.31.001076].
44. J. C. Jung and M. J. Schnitzer, "Multiphoton endoscopy," *Opt. Lett.* **28**(11), 902 (2003) [doi:10.1364/OL.28.000902].
45. M. J. Levene, "In Vivo Multiphoton Microscopy of Deep Brain Tissue," *J. Neurophysiol.* **91**(4), 1908–1912 (2004) [doi:10.1152/jn.01007.2003].
46. H. Bao et al., "Fast handheld two-photon fluorescence microendoscope with a $475\ \mu\text{m} \times 475\ \mu\text{m}$ field of view for in vivo imaging," *Opt. Lett.* **33**(12), 1333 (2008) [doi:10.1364/OL.33.001333].
47. G. Liu et al., "Multiphoton microscopy system with a compact fiber-based femtosecond-pulse laser and handheld probe," *J. Biophotonics* **4**(1–2), 34–39 (2011) [doi:10.1002/jbio.201000049].
48. D. Huang et al., "Optical Coherence Tomography," *Science* **254**(5035), 1178–1181 (1991).
49. M. R. Hee et al., "Quantitative Assessment of Macular Edema With Optical Coherence Tomography," *Arch. Ophthalmol.* **113**(8), 1019–1029 (1995) [doi:10.1001/archophth.1995.01100080071031].
50. G. J. Tearney et al., "In Vivo Endoscopic Optical Biopsy with Optical Coherence Tomography," *Science* **276**(5321), 2037–2039 (1997) [doi:10.1126/science.276.5321.2037].
51. B. J. Vakoc et al., "Comprehensive esophageal microscopy by using optical frequency-domain imaging (with video)," *Gastrointest. Endosc.* **65**(6), 898–905 (2007) [doi:10.1016/j.gie.2006.08.009].
52. M. J. Suter et al., "Comprehensive microscopy of the esophagus in human patients with optical frequency domain imaging," *Gastrointest. Endosc.* **68**(4), 745–753 (2008) [doi:10.1016/j.gie.2008.05.014].
53. M. J. Suter et al., "Image-guided biopsy in the esophagus through comprehensive optical frequency domain imaging and laser marking: a study in living swine," *Gastrointest. Endosc.* **71**(2), 346–353 (2010) [doi:10.1016/j.gie.2009.07.007].
54. J. A. Evans et al., "Identifying intestinal metaplasia at the squamocolumnar junction by using optical coherence tomography," *Gastrointest. Endosc.* **65**(1), 50–56 (2007) [doi:10.1016/j.gie.2006.04.027].
55. M. V. Sivak et al., "High-resolution endoscopic imaging of the GI tract using optical coherence tomography," *Gastrointest. Endosc.* **51**(4 Pt 1), 474–479 (2000).
56. J. M. Poneros et al., "Diagnosis of specialized intestinal metaplasia by optical coherence tomography," *Gastroenterology* **120**(1), 7–12 (2001).
57. P. R. Pfau et al., "Criteria for the diagnosis of dysplasia by endoscopic optical coherence tomography," *Gastrointest. Endosc.* **58**(2), 196–202 (2003) [doi:10.1067/mge.2003.344].

58. P.-A. Testoni and B. Mangiavillano, "Optical coherence tomography in detection of dysplasia and cancer of the gastrointestinal tract and bilio-pancreatic ductal system," *World J. Gastroenterol.* **14**(42), 6444–6452 (2008).
59. J. H. Tabibian et al., "Advanced endoscopic imaging of indeterminate biliary strictures," *World J. Gastrointest. Endosc.* **7**(18), 1268–1278 (2015) [doi:10.4253/wjge.v7.i18.1268].
60. G. J. Tearney et al., "Optical biopsy in human urologic tissue using optical coherence tomography," *J. Urol.* **157**(5), 1915–1919 (1997).
61. J. Gallwas et al., "Optical coherence tomography as a non-invasive imaging technique for preinvasive and invasive neoplasia of the uterine cervix," *Ultrasound Obstet. Gynecol. Off. J. Int. Soc. Ultrasound Obstet. Gynecol.* **36**(5), 624–629 (2010) [doi:10.1002/uog.7656].
62. L. P. Hariri et al., "Simultaneous optical coherence tomography and laser induced fluorescence imaging in rat model of ovarian carcinogenesis," *Cancer Biol. Ther.* **10**(5), 438–447 (2010).
63. Wolfgang Drexler and James G. Fujimoto, Eds., *Optical Coherence Tomography*, 2nd ed., Springer International Publishing (2015).
64. R. Dsouza et al., "Dermascope guided multiple reference optical coherence tomography," *Biomed. Opt. Express* **5**(9), 2870–2882 (2014) [doi:10.1364/BOE.5.002870].
65. R. Dsouza et al., "3D nondestructive testing system with an affordable multiple reference optical-delay-based optical coherence tomography," *Appl. Opt.* **54**(18), 5634–5638 (2015).
66. M. Leahy et al., "Multiple reference optical coherence tomography (MR-OCT) system," 2013, 85800L–85800L–8 [doi:10.1117/12.2002480].
67. P. M. McNamara et al., "Development of a miniature multiple reference optical coherence tomography imaging device," 2016, 969909–969909–4 [doi:10.1117/12.2211309].
68. M. J. Leahy et al., "The how and why of a \$10 optical coherence tomography system," 2016, 96970T–96970T–3 [doi:10.1117/12.2213465].
69. *Advances in Imaging and Electron Physics: Optics of Charged Particle Analyzers*, Academic Press (2011).
70. "generic tissue optical properties," <http://omlc.org/news/feb15/generic_optics/index.html> (accessed 28 November 2016).
71. R. A. McLaughlin, D. Lorensen, and D. D. Sampson, "Needle Probes in Optical Coherence Tomography," in *Handbook of Coherent-Domain Optical Methods: Biomedical Diagnostics, Environmental Monitoring, and Materials Science*, V. V. Tuchin, Ed., pp. 1065–1102, Springer New York, New York, NY (2013).
72. J. Wu et al., "Paired-angle-rotation scanning optical coherence tomography forward-imaging probe," *Opt. Lett.* **31**(9), 1265–1267 (2006).
73. S. Han et al., "Handheld forward-imaging needle endoscope for ophthalmic optical coherence tomography inspection," *J. Biomed. Opt.* **13**(2), 20505–020505–3 (2008) [doi:10.1117/1.2904664].
74. A. D. Aguirre et al., "Two-axis MEMS Scanning Catheter for Ultrahigh Resolution Three-dimensional and En Face Imaging," *Opt. Express* **15**(5), 2445–2453 (2007).
75. H.-C. Park et al., "Forward-viewing endoscopic OCT catheter using asymmetrically resonant fiber scanner," in 2013 International Conference on Optical MEMS and Nanophotonics (OMN), pp. 7–8 (2013) [doi:10.1109/OMN.2013.6659032].
76. H.-C. Park et al., "Forward imaging OCT endoscopic catheter based on MEMS lens scanning," *Opt. Lett.* **37**(13), 2673–2675 (2012).
77. M. Strathman et al., "Dynamic focus-tracking MEMS scanning micromirror with low actuation voltages for endoscopic imaging," *Opt. Express* **21**(20), 23934–23941 (2013).
78. J. Sun et al., "3D in vivo optical coherence tomography based on a low-voltage, large-scan-range 2D MEMS mirror," *Opt. Express* **18**(12), 12065–12075 (2010).

79. K. Liang et al., "Ultrahigh speed en face OCT capsule for endoscopic imaging," *Biomed. Opt. Express* **6**(4), 1146–1163 (2015) [doi:10.1364/BOE.6.001146].
80. B. Qi et al., "Dynamic focus control in high-speed optical coherence tomography based on a microelectromechanical mirror," *Opt. Commun.* **232**(1–6), 123–128 (2004) [doi:10.1016/j.optcom.2004.01.015].
81. C. M. Lee et al., "Scanning fiber endoscopy with highly flexible, 1-mm catheterscopes for wide-field, full-color imaging," *J. Biophotonics* **3**(5–6), 385–407 (2010) [doi:10.1002/jbio.200900087].
82. K. L. Lurie et al., "Rapid scanning catheterscope for expanded forward-view volumetric imaging with optical coherence tomography," *Opt. Lett.* **40**(13), 3165–3168 (2015).
83. L. Huo et al., "Forward-viewing resonant fiber-optic scanning endoscope of appropriate scanning speed for 3D OCT imaging," *Opt. Express* **18**(14), 14375–14384 (2010).
84. H.-C. Park, Y.-H. Seo, and K.-H. Jeong, "Lissajous fiber scanning for forward viewing optical endomicroscopy using asymmetric stiffness modulation," *Opt. Express* **22**(5), 5818–5825 (2014).
85. D. Lorenser et al., "Ultrathin side-viewing needle probe for optical coherence tomography," *Opt. Lett.* **36**(19), 3894–3896 (2011) [doi:10.1364/OL.36.003894].
86. M. R. Keenan et al., "Dual Optical Modality Endoscopic Imaging of Cancer Development in the Mouse Colon," *Lasers Surg. Med.* **47**(1), 30–39 (2015) [doi:10.1002/lsm.22307].
87. W. A. Welge and J. K. Barton, "Expanding Functionality of Commercial Optical Coherence Tomography Systems by Integrating a Custom Endoscope," *PLoS ONE* **10**(9) (2015) [doi:10.1371/journal.pone.0139396].
88. T.-H. Tsai et al., "Ultrahigh speed endoscopic optical coherence tomography using micromotor imaging catheter and VCSEL technology," *Biomed. Opt. Express* **4**(7), 1119–1132 (2013) [doi:10.1364/BOE.4.001119].
89. G. G. Stokes, "On the Change of Refrangibility of Light," *Philos. Trans. R. Soc. Lond.* **142**, 463–562 (1852) [doi:10.1098/rstl.1852.0022].
90. H. Stübel, "Die Fluoreszenz tierischer Gewebe in ultravioletter Licht," *Pflüg. Arch. Für Gesamte Physiol. Menschen Tiere* **142**(1), 1–14 (1911) [doi:10.1007/BF01680690].
91. S. Andersson-Engels et al., "In vivo fluorescence imaging for tissue diagnostics," *Phys. Med. Biol.* **42**(5), 815–824 (1997).
92. E. Gudgin, R. Lopez-Delgado, and W. R. Ware, "The tryptophan fluorescence lifetime puzzle. A study of decay times in aqueous solution as a function of pH and buffer composition," *Can. J. Chem.* **59**(7), 1037–1044 (1981) [doi:10.1139/v81-154].
93. R. Cubeddu et al., "Time-gated fluorescence spectroscopy of the tumor localizing fraction of HpD in the presence of cationic surfactant," *Photochem. Photobiol.* **50**(2), 157–163 (1989).
94. J. Wu, M. S. Feld, and R. P. Rava, "Analytical model for extracting intrinsic fluorescence in turbid media," *Appl. Opt.* **32**(19), 3585–3595 (1993).
95. A. J. Durkin et al., "Relation between fluorescence spectra of dilute and turbid samples," *Appl. Opt.* **33**(3), 414–423 (1994).
96. S. A. Ahmed et al., "Effect of multiple light scattering and self-absorption on the fluorescence and excitation spectra of dyes in random media," *Appl. Opt.* **33**(13), 2746–2750 (1994).
97. I. Munro et al., "Toward the clinical application of time-domain fluorescence lifetime imaging," *J. Biomed. Opt.* **10**(5), 51403–051403–051409 (2005) [doi:10.1117/1.2102807].
98. T. E. Renkoski et al., "Ratio images and ultraviolet C excitation in autofluorescence imaging of neoplasms of the human colon," *J. Biomed. Opt.* **18**(1), 16005 (2013) [doi:10.1117/1.JBO.18.1.016005].
99. Molly Keenan et al., "Design and characterization of a combined OCT and wide field imaging falloposcope for ovarian cancer detection," *Biomed. Opt. Express*.

100. T. Tate et al., "Optical design of an optical coherence tomography and multispectral fluorescence imaging endoscope to detect early stage ovarian cancer," 2014, 92931F–92931F–8 [doi:10.1117/12.2073824].
101. J. Black et al., "Falloscope and method for ovarian cancer detection," WO2016126879 A1 (2016).
102. "American Cancer Society. Cancer Facts & Figures" (2015).
103. Eagle and Ledermann, "Tumor Markers in Ovarian Malignancies," *The oncologist* **2**(5), 324–329 (1997).
104. B. C. Vanderhyden, "Loss of ovarian function and the risk of ovarian cancer," *Cell Tissue Res.* **322**(1), 117–124 (2005) [doi:10.1007/s00441-005-1100-1].
105. J. G. Fujimoto et al., "Optical biopsy and imaging using optical coherence tomography," *Nat. Med.* **1**(9), 970–972 (1995).
106. J. N. McAlpine et al., "Autofluorescence imaging can identify preinvasive or clinically occult lesions in fallopian tube epithelium: A promising step towards screening and early detection," *Gynecol. Oncol.* **120**(3), 385–392 (2011) [doi:10.1016/j.ygyno.2010.12.333].
107. J. M. Watson et al., "In vivo time-serial multi-modality optical imaging in a mouse model of ovarian tumorigenesis," *Cancer Biol. Ther.* **15**(1), 42–60 (2014) [doi:10.4161/cbt.26605].
108. B. L. Wen et al., "Texture analysis applied to second harmonic generation image data for ovarian cancer classification," *J. Biomed. Opt.* **19**(9), 96007 (2014) [doi:10.1117/1.JBO.19.9.096007].
109. D. Granot et al., "In vivo Imaging of the Systemic Recruitment of Fibroblasts to the Angiogenic Rim of Ovarian Carcinoma Tumors," *Cancer Res.* **67**(19), 9180–9189 (2007) [doi:10.1158/0008-5472.CAN-07-0684].
110. R. M. Williams et al., "Strategies for High-Resolution Imaging of Epithelial Ovarian Cancer by Laparoscopic Nonlinear Microscopy," *Transl. Oncol.* **3**(3), 181–194 (2010).
111. U. Alqasemi et al., "Interlaced photoacoustic and ultrasound imaging system with real-time coregistration for ovarian tissue characterization," *J. Biomed. Opt.* **19**(7), 76020 (2014) [doi:10.1117/1.JBO.19.7.076020].
112. R. Drezek et al., "Understanding the contributions of NADH and collagen to cervical tissue fluorescence spectra: Modeling, measurements, and implications," *J. Biomed. Opt.* **6**(4), 385–396 (2001) [doi:10.1117/1.1413209].
113. S. Prahl, "Tabulated Molar Extinction Coefficient for Hemoglobin in Water," <<http://omlc.org/spectra/hemoglobin/summary.html>> (accessed 2 March 2015).
114. *User's Guide*, Stata 14, Stata Press (2015).
115. E. N. Atkinson, "Age and FSH effects in fluorescence spectra from the cervix: An exploratory analysis," *Gynecol. Oncol.* **99**(3, Supplement), S95–S97 (2005) [doi:10.1016/j.ygyno.2005.07.051].
116. Y. Yang et al., "Optical scattering coefficient estimated by optical coherence tomography correlates with collagen content in ovarian tissue," *J. Biomed. Opt.* **16**(9), 90504 (2011) [doi:10.1117/1.3625247].
117. B. Banerjee et al., "Tryptophan autofluorescence imaging of neoplasms of the human colon," *J. Biomed. Opt.* **17**(1), 16003 (2012) [doi:10.1117/1.JBO.17.1.016003].
118. S. C. Gebhart, S. K. Majumder, and A. Mahadevan-Jansen, "Comparison of spectral variation from spectroscopy to spectral imaging," *Appl. Opt.* **46**(8), 1343 (2007) [doi:10.1364/AO.46.001343].
119. K. T. Schomacker et al., "Ultraviolet laser-induced fluorescence of colonic tissue: basic biology and diagnostic potential," *Lasers Surg. Med.* **12**(1), 63–78 (1992).
120. E. Crowell et al., "Correlation Coefficient Mapping in Fluorescence Spectroscopy: Tissue Classification for Cancer Detection," *Anal. Chem.* **77**(5), 1368–1375 (2005) [doi:10.1021/ac049074+].

121. R. S. Bradley and M. S. Thorniley, "A review of attenuation correction techniques for tissue fluorescence," *J. R. Soc. Interface* **3**(6), 1–13 (2006) [doi:10.1098/rsif.2005.0066].
122. J. Y. Qu and J. Hua, "Calibrated fluorescence imaging of tissue in vivo," *Appl. Phys. Lett.* **78**(25), 4040–4042 (2001) [doi:10.1063/1.1379980].
123. P. O. Brown and C. Palmer, "The Preclinical Natural History of Serous Ovarian Cancer: Defining the Target for Early Detection," *PLoS Med.* **6**(7) (2009) [doi:10.1371/journal.pmed.1000114].
124. E. Lengyel, "Ovarian Cancer Development and Metastasis," *Am. J. Pathol.* **177**(3), 1053–1064 (2010) [doi:10.2353/ajpath.2010.100105].
125. J. Kerin et al., "Development and application of a falloposcope for transvaginal endoscopy of the fallopian tube," *J. Laparoendosc. Surg.* **1**(1), 47–56 (1990).
126. A. Y. Wong and S. M. Walker, "Fallopscopy--a prerequisite to the proper assessment of tubal infertility," *Hong Kong Med. J. Xianggang Yi Xue Za Zhi Hong Kong Acad. Med.* **5**(1), 76–81 (1999).
127. J. Kerin et al., "Fallopscopy: a microendoscopic technique for visual exploration of the human fallopian tube from the uterotubal ostium to the fimbria using a transvaginal approach," *Fertil. Steril.* **54**(3), 390–400 (1990).
128. Y. Tanaka et al., "Renaissance of surgical recanalization for proximal fallopian tubal occlusion: falloposcopic tuboplasty as a promising therapeutic option in tubal infertility," *J. Minim. Invasive Gynecol.* **18**(5), 651–659 (2011) [doi:10.1016/j.jmig.2011.06.014].
129. M. W. SA Awaiba CH, "Mini Camera Modules Pave Way for Less-Invasive Visualization," <<http://www.photonics.com/Article.aspx?AID=56663>> (accessed 21 September 2016).
130. E. J. Seibel et al., "In vivo laser-based imaging of the human fallopian tube for future cancer detection," 2015, 93040Q–93040Q–9 [doi:10.1117/12.2076972].
131. M. Brewer et al., "Fluorescence spectroscopy for in vivo characterization of ovarian tissue," *Lasers Surg. Med.* **29**(2), 128–135 (2001) [doi:10.1002/lsm.1098].
132. T. H. Tate et al., "Multispectral fluorescence imaging of human ovarian and fallopian tube tissue for early-stage cancer detection," *J. Biomed. Opt.* **21**(5), 56005 (2016) [doi:10.1117/1.JBO.21.5.056005].
133. Molly Keenan et al., "Design and characterization of a combined OCT and wide field imaging falloposcope for ovarian cancer detection."
134. J. F. Black et al., "A six-color four-laser mobile platform for multi-spectral fluorescence imaging endoscopy," 2015, 93040T–93040T–14 [doi:10.1117/12.2077999].
135. J.-H. Han, J. Lee, and J. U. Kang, "Pixelation effect removal from fiber bundle probe based optical coherence tomography imaging," *Opt. Express* **18**(7), 7427–7439 (2010) [doi:10.1364/OE.18.007427].
136. D. Marcuse, "Loss analysis of single-mode fiber splices," *Bell Syst. Tech. J.* **56**(5), 703–718 (1977) [doi:10.1002/j.1538-7305.1977.tb00534.x].
137. S. G. Parulekar, "Ultrasound evaluation of common bile duct size," *Radiology* **133**(3 Pt 1), 703–707 (1979) [doi:10.1148/133.3.703].
138. "Optimization Online - Solving the problem of packing equal and unequal circles in a circular container," <http://www.optimization-online.org/DB_HTML/2008/06/1999.html> (accessed 5 January 2017).
139. M. Keenan et al., "Design and characterization of a combined OCT and wide field imaging falloposcope for ovarian cancer detection," *Biomed. Opt. Express* **8**(1), 124–136 (2017) [doi:10.1364/BOE.8.000124].
140. N. Stasio et al., "Towards new applications using capillary waveguides," *Biomed. Opt. Express* **6**(12), 4619–4631 (2015) [doi:10.1364/BOE.6.004619].

APPENDIX A: MFI *EX VIVO* STUDY

This appendix includes all supplemental material for the MFI *ex vivo* tissue study. This includes copies or locating instructions for the raw data, analyzed data, MATLAB scripts used in the study and standard operating procedure (SOP) for the MFI system. Relevant insights or instructions for each item are also provided.

A.1. Accepted Manuscript

The following manuscript titled “Multispectral fluorescence imaging of human ovarian and fallopian tube tissue for early-stage cancer detection,” was published by the Journal of Biomedical Optics in 2015:

T. H. Tate et al., “Multispectral fluorescence imaging of human ovarian and fallopian tube tissue for early-stage cancer detection,” J Biomed Opt 21(5), 56005 (2016)
[doi:10.1117/1.JBO.21.5.056005].

Multispectral fluorescence imaging of human ovarian and fallopian tube tissue for early stage cancer detection

Tyler H. Tate^{*a}, Brenda Baggett^b, Photini F.S. Rice^b, Jennifer W. Koevary^b, Gabriel V. Orsinger^b, Ariel C. Nymeyer^b, Weston A. Welge^a, Kathylynn Saboda^c, Denise J. Roe^c, Kenneth D. Hatch^c, Setsuko K. Chambers^c, Urs Utzinger^{a,b}, Jennifer K. Barton^{a,b}

^aCollege of Optical Sciences, University of Arizona, 1630 E University Blvd, Tucson, AZ 85721

^bBiomedical Engineering, University of Arizona 1657 E Helen Street, Tucson, AZ 85721

^cUniversity of Arizona Cancer Center, 1515 N. Campbell Ave, Tucson, AZ 85724

Abstract. With early detection, 5-year survival rates for ovarian cancer exceed 90%, yet no effective early screening method exists. Emerging consensus suggests over 50% of the most lethal form of the disease originates in the fallopian tube. Twenty-eight women undergoing oophorectomy or debulking surgery were consented for the use of surgical discard tissue samples for multispectral fluorescence imaging (MFI). Using multiple ultraviolet and visible excitation wavelengths and emissions bands, twelve fluorescence and six reflectance images of forty-seven ovarian and thirty-one fallopian tube tissue samples were recorded. After imaging, each sample was fixed, sectioned and stained for pathological evaluation. Univariate logistic regression (ULR) showed cancerous tissue samples had significantly lower intensity than non-cancerous tissue for seventeen image types. The predictive power of multiple image types was evaluated using multivariate logistic regression (MLR) and quadratic discriminant analysis (QDA). Two MLR models each using two image types had receiver operating characteristic curves with area under the curve exceeding 0.9. QDA determined 56 image type combinations with perfect resubstituting using as few as five image types. Adaption of the system for future in vivo fallopian tube and ovary endoscopic imaging is possible, which may enable sensitive detection of ovarian cancer with no exogenous contrast agents.

Keywords: Ovary, Fallopian, Cancer, Multispectral, Fluorescence, Imaging

*First Author, E-mail: TylerTate@email.arizona.edu

Grant Funding:

Department of Defense OCRP OC120140

The University of Arizona Cancer Center Support Grant P30CA023074

1 Introduction

Ovarian cancer is the most deadly female reproductive malignancy with over 21,000 new cases and over 14,000 deaths annually in the US¹⁰². Ovarian cancer typically presents with non-specific symptoms. Current screening methods (physical examination, transvaginal ultrasound, the CA-125 blood test) have not proven to be effective when used for annual screening in the general population in large clinical trials², although one noted

a possible reduction in mortality after 7-14 years of annual screening for some population groups³. The lack of specific symptoms or a proven effective screening method results in only 15% of cases discovered early stage when 5-year survival rates are over 90%. Thus overall 5-year survival rates are just 45%¹⁰². Certain high-risk women (BRCA1/2 gene mutations, family history of breast or ovarian cancer) are recommended to undergo prophylactic oophorectomy to remove the ovaries and fallopian tubes. This drastic measure decreases risk, but side effects include increased mortality for women who undergo the procedure before age 45, without hormone replacement^{6,7}. Early detection is extremely difficult because early changes may be too subtle to be resolved with whole body imaging techniques such as magnetic resonance imaging, computed tomography or ultrasound^{103,104}. Additionally, emerging consensus suggests that perhaps over 50% of the most lethal form of the disease, high grade serous ovarian cancer, originates in the fallopian tube^{10,16}.

The need for an effective screening method is universal to all women, but is particularly critical for high-risk women. Without any high-risk factors the lifetime risk of developing ovarian cancer is 1-2%. Women with a family history, but no BRCA mutation have a risk of 4-7% while women with family history and a BRCA mutation have a 23-54% lifetime risk⁵. For high-risk patients a reliable detection method may delay prophylactic salpingo-oophorectomy with regular monitoring. Advanced optical imaging techniques are a promising approach to provide the resolution and functional imaging needed for a sensitive and specific screening test.

Optical techniques can be miniaturized for endoscopy, are robust and are relatively inexpensive. Ovarian cancer has been imaged by several microscopic optical modalities in

the past, including optical coherence tomography (OCT)^{26–29,105}, confocal microscopy^{30–33}, multiphoton microscopy (MPM)^{34,35}, photoacoustic imaging (PAI)^{29,36–38} and fluorescence spectroscopy/imaging^{39–41,106}. OCT captures high resolution depth images of tissue microstructure, and has demonstrated ability to distinguish normal tissue from ovarian cancer *in vivo* in animal models¹⁰⁷ and laparoscopically *in vivo* in human patients²⁶. Fluorescence confocal imaging has been integrated into a microlaparoscope and with ability to detect cancerous tissue *in vivo*^{31–33}. High quality images of nuclear size and shape are obtained by the use of contrast agents which have not yet been U.S. Food and Drug Administration approved for *in vivo* use. MPM, including second harmonic generation and multi-photon excited fluorescence, can image cell and connective tissue structure and metabolic tissue properties. It has demonstrated promise for distinguishing healthy from diseased human tissue *ex vivo*^{34,35,108}, as well as *in vivo* in mouse models^{107,109,110}. Photoacoustic Imaging (PAI) combines high resolution ultrasound (US) imaging with contrast from optical absorption. Visible red or near-infrared (NIR) illumination wavelengths are commonly used to provide large imaging depths. Using multiple wavelengths allows mapping of changes in hemoglobin concentration and oxygen saturation related to tumor angiogenesis^{29,36–38,111}.

The above techniques have high resolution, small field of view, are point- or line-scanning imaging methods or require reconstruction, and thus have limited utility for navigation or rapid, large-area visualization. Some, such as multiphoton microscopy and photoacoustic imaging, typically utilize complex laser systems which are less suitable for a robust, inexpensive clinical imaging system, although, new fiber-based laser systems may enable small portable systems^{42–47}. All of the above high resolution optical techniques may

have promise for detecting early stage ovarian cancer assuming the imaging system can be placed near or in contact with the epithelium of the ovary and fallopian tube.

While high resolution techniques show promise, they may need to be coupled with a lower resolution, wide field of view, and long depth of field modality to navigate the ovarian and fallopian tube epithelium and identify suspicious areas. In an open surgery a high resolution modality endoscope can be visually directed to the tissue of interest, whereas in a laparoscopic procedure a white-light imaging system (either integrated with the high resolution system into a dual-modality endoscope or in a second endoscope) can be used for navigation. However, the subtle changes of early stage ovarian cancer may not be visible to the human eye or a standard white-light endoscope. Thus in this case, the guidance imaging system simply guides the high resolution system to the ovary so the high resolution modality can optically biopsy discrete locations on the ovary and fallopian tubes. Furthermore, open and even laparoscopic surgeries are too invasive to be a widely used screening method. A less invasive imaging method could utilize the natural orifice of the vagina, uterus and fallopian tube for a miniature endoscopic imaging system. The system could combine a wide field of view, highly sensitive navigation and surveillance technique with a more specific high resolution technique.

Fluorescence imaging is a promising candidate for the large field of view, highly sensitive imaging technique. Systems visualizing autofluorescence have been demonstrated¹¹⁻¹³. Autofluorescence imaging is advantageous because it does not require any dyes or contrast agents that may complicate regulatory approval. Previous studies by the investigators and others have characterized normal, cancerous and benign *ex vivo* ovarian tissue autofluorescence using fiberoptic probes. One study excited tissue with a

325 nm pulsed laser and evaluated the emission spectrum from 350 to 600 nm for normal, benign and malignant samples⁴¹. Another study used a probe with tunable narrow-band excitation and emission windows to develop complete excitation-emission matrices for excitation from 270 to 550 nm and emission from 290 to 700 nm with high spectral resolution³⁹. Wide-field spectral imaging with limited wavelengths has also been performed on both ovarian and fallopian tube tissue. Ovarian tissue was imaged using a 365 nm source to excite the tissue and an imaging system capable of recording 8 emission bands between 400 and 640 nm⁴⁰. Another study imaged normal and cancerous fallopian tube samples by capturing a series of images including white-light reflectance, narrow-band green reflectance, green autofluorescence (405 and 436 nm excitation) and blue autofluorescence (405 nm excitation)¹⁰⁶. All these studies indicate autofluorescence imaging shows promise for detection of ovarian cancer.

Building upon these previous studies, a new imaging system was developed with a wide field of view, multiple excitation wavelengths and multiple emission bands. Multi-spectral Fluorescence Imaging (MFI) creates a series of co-registered fluorescence and reflectance images with a specific set of excitation wavelengths and emission bands that are selected to match the expected characteristics of known endogenous tissue fluorophores. These fluorophores may change in concentration and spatial location as normal tissue transitions to a cancerous or benign abnormality state. The reflectance images taken at several narrowband wavelengths effectively sample the blood absorption spectrum of hemoglobin, as well as indicate the overall remittance of light from scatterers in the tissue. Cancerous tissue tends to have increased vessel density leading to higher optical absorption and decreased reflectance and fluorescence^{40,106}. In cervical tissue it has been

shown that increased proteolytic activity associated with dysplasia reduces collagen fluorescence¹¹². The fluorescence images are obtained at multiple excitation wavelengths between 255 nm to 550 nm with emission bands between 340 nm and 650 nm. Miniaturization of the system to endoscopy is possible. The system has been successfully used to obtain high contrast images of colon polyps⁹⁸ and is utilized in this study to visualize ovarian and fallopian tube surgical biopsies.

2 Materials and Methods

2.1 Patients

Patients at the University of Arizona Medical Center undergoing oophorectomy, salpingo-oophorectomy, total abdominal hysterectomy with bilateral salpingo-oophorectomy and debulking surgeries were asked to donate surgical discard tissue to this imaging study. Additionally, the patients were requested to fill out a questionnaire including questions about age and menopause status. The study and questionnaire were approved by the Institutional Review Board of the University of Arizona and tissue was collected for nine months. Informed consent was obtained from twenty-eight patients during the study. Tissue was not available for four consented patients. Samples from the remaining twenty-four patients were imaged on the MFI system.

2.2 Tissue Samples

Surgical discard tissue was made available after samples necessary for clinical pathology were removed. Collected tissue samples for the study were small pieces of the ovary, fimbria or distal fallopian tube. The imaged surface area of resected tissues was

typically 1.1 cm^2 . Surface area for small samples of all tissue types were typically $0.2\text{-}0.3 \text{ cm}^2$, while the largest imaged surface areas were 3.3 cm^2 and 9.6 cm^2 for fallopian tube and ovarian samples respectively.

2.3 Multispectral Fluorescence Imaging System

The laboratory-built MFI system used to collect images has been described in detail previously⁹⁸. The system uses a xenon arc lamp (300 W, Lambda LS, Sutter Instruments, Novato, California) and 10-position filter wheel to select discrete narrowband ($\sim 20 \text{ nm}$ FWHM) illumination wavelengths between 260 nm and 650 nm. The illumination light is transmitted through a custom quartz fiber bundle with feedback fibers to monitor source power. The fiber illuminates a $4 \text{ cm} \times 4 \text{ cm}$ field of view. A color-corrected UV imaging lens images the sample onto a thermoelectrically cooled, UV-enhanced camera with intensified CCD (PhotonMAX: 512B, Princeton Instruments, Trenton, NJ). A second 10-position filter wheel with long pass filters selects the detected wavelengths. Software written in LabVIEW (National Instruments, Austin, Texas) automatically collects a series of raw images of interest by controlling the two filter wheels and camera. The imaging system uses image subtraction of long pass filtered images to create effective bandpass images. For example, a 410-500 nm emission image is created by subtracting a 500 nm long pass image from a 410 nm long pass image. In total, the software uses the collected raw images to generate 18 output images for each sample: 12 autofluorescence images and 6 reflectance images (Fig. 1A). The emission and excitation combinations used for autofluorescence images are selected based on expected characteristics of endogenous

fluorophores³⁹. The reflected light images are designed to sample the absorption spectrum of hemoglobin¹¹³ (Fig. 1B).

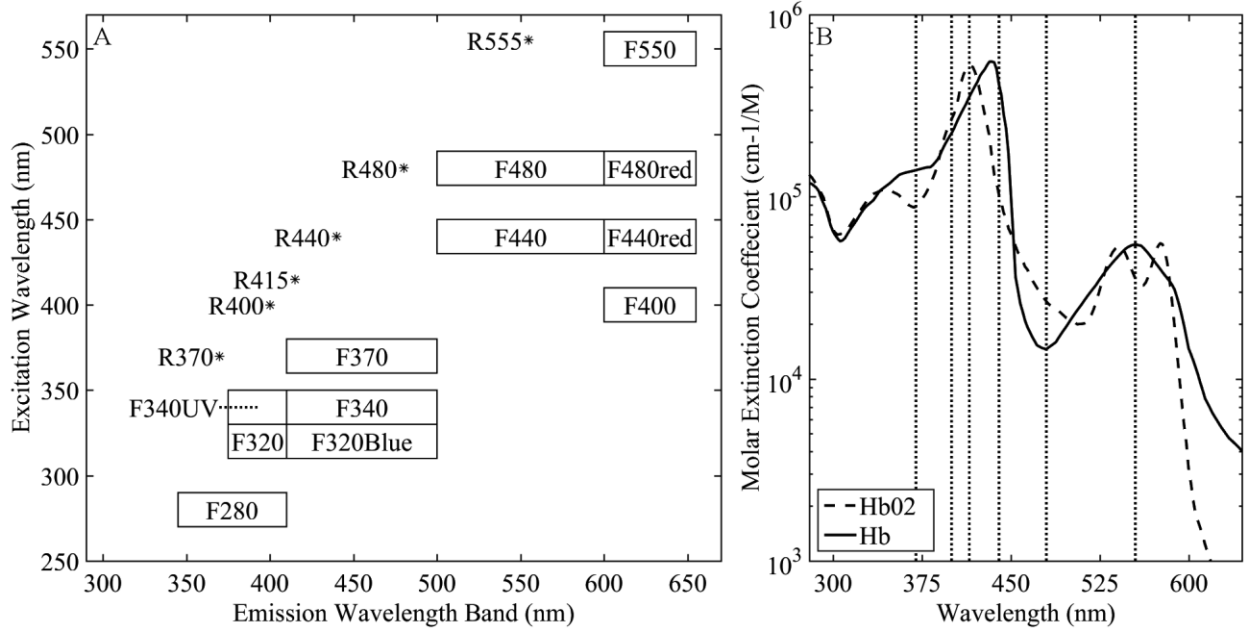


Figure 6: Summary of MFI image types. A) Plot of 18 image types collected by system. Six reflectance images are represented by asterisks having equal excitation and emission wavelengths. 12 fluorescence images are represented by boxes with height representing 20 nm FWHM illumination bandwidth and width representing the bandwidth of the collected emission. B) The absorption spectrum of hemoglobin from 250 nm to 650 nm (data¹¹³). Vertical dotted lines correspond to 6 recorded reflectance images from the MFI system. HbO2: oxygenated hemoglobin, Hb: deoxygenated hemoglobin.

2.4 Tissue Imaging

Surgical discard tissue was placed in saline immediately following surgery and transported to the MFI system. Between 1 and 8 samples were obtained and imaged per patient with between 1 and 5 samples placed in the field of view of the system at a time. Tissues were typically imaged within one hour of removal, but at most within 2 hours of removal. Tissue was kept moist with saline before and after imaging.

2.5 Histology and Pathological Evaluation

Immediately after imaging each tissue sample was affixed to filter paper to maintain orientation and fixed in 10% buffered formalin or Histochoice (Ameresco). Tissues were histologically processed into paraffin blocks and cut into 6 μm sections. Slides were stained with hematoxylin and eosin (H&E) and a histologic diagnosis of the imaged tissue obtained independent of patient diagnosis by a pathologist at the University of Arizona Cancer Center Tissue Acquisition and Cellular/Molecular Analysis Shared Resource.

2.6 Image Processing

System calibration was performed to enable comparison of intensity measurements for each piece of tissue. Immediately before or after each imaging session, a uniform reflector was imaged to normalize intensity across the field of view. Additionally, illumination power measurements and images of known fluorophores were used to normalize changes in lamp power spectrum over time. Imaging was performed in a dark room to minimize background light. As a further correction, images of tissue were obtained at each filter setting with the illumination lamp on and off. The lamp-off image was subtracted from the lamp-on image to correct for changes in ambient lighting. Exposure times were verified to be the same for all images within each image type. All normalization procedures were performed on the raw intensity values from the camera detector using MATLAB (The MathWorks, Natick, Massachusetts). Images with the desired excitation wavelength and emission band were saved as 32-bit floating point TIFF files to maintain absolute intensity values. The result was 18 recorded images per imaging sequence; 6 fluorescence images with UV excitation wavelengths, 6 fluorescence images with visible excitation

wavelengths and 6 reflected light images. An example image set is shown in Fig. 2. Only after all normalization procedures were performed were the tissue image gray scale values statistically compared.

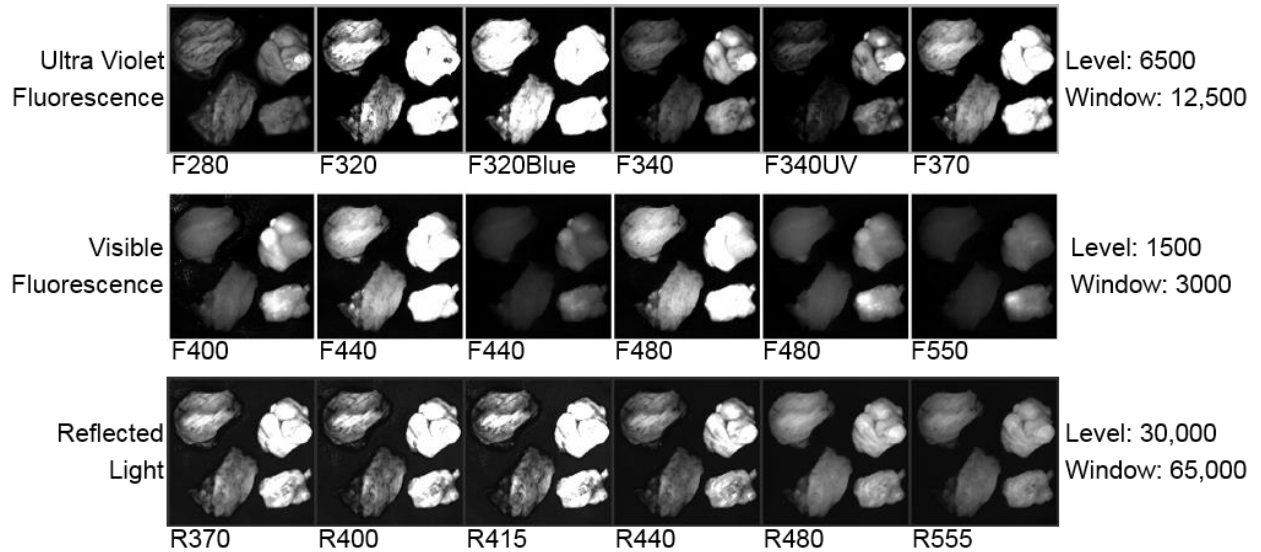


Figure 7: Example of the 18 images collected on a set of tissues. Within each image the two tissue samples on the left are histologically normal fallopian tube samples and the two samples on the right are histologically normal ovary samples. Image gray scale values have been compressed to 8 bits for display, and contrast window and level have been adjusted between rows to account for significant differences in image intensity. Thus the intensities within a row of images are comparable, but the intensities between rows are not.

Using image analysis software (ImageJ, National Institute of Health) each set of 18 images was combined into a coregistered image stack. Each tissue within each stack was manually outlined with a many point polygon. These steps allowed simultaneous measurement of intensity statistics (mean, median, min, max and standard error) for all tissue samples and all image types in each image stack. The area (pixels) of each tissue was also recorded. All data were then combined into a master table providing the intensity statistics, tissue type, tissue pathology, imaging date and the age and menopause status if disclosed on the questionnaire, for each tissue sample.

2.7 Statistical Analysis

Three types of statistical analysis- descriptive statistics, logistic regression (LR) and quadratic discriminant analysis (QDA)- were conducted. Because of the small number of histologically-confirmed cancer samples from the fallopian tube, we limited the analysis of fallopian tube samples to descriptive statistics. LR has fewer assumptions than discriminant analysis and gives a probability of an outcome based on independent variables. It is useful for evaluating data in which one or more independent variables (e.g. image type mean intensities) determine a binary outcome (e.g. cancerous vs. non-cancerous ovarian tissue). QDA is a method of statistical classification that uses a set of training data to build quadratic classifiers designed to predict classification (e.g. normal, benign, cancerous pathology) given the independent variables (e.g. image type mean intensities) associated with the sample. In this study QDA models used all sample data as a training set and were validated using resubstitution.

2.7.1 Descriptive Statistics

For ovarian and fallopian tube samples the mean and standard error of image intensities was calculated and compared between tissue in the broad pathological categories- normal, benign and cancerous- for each image type. For ovarian tissue, robust standard error with clustering on patient was also calculated. In general, robust standard error calculations assume independence for each sample. Since multiple tissue samples from the same patient were often obtained the variance-covariance matrices used to determine robust standard error for each tissue were clustered on the patients. Clustering allows for intragroup (multiple tissues from one patient) correlation to be accounted for appropriately¹¹⁴.

2.7.2 Logistic Regression Analysis on Ovarian Tissue

The University of Arizona Cancer Center Biostatistics Shared Service performed LR on ovarian sample image data using Stata13 (StataCorp LP, College Station, Texas). The ultimate goal was to determine which, if any, small combinations of image types could accurately predict whether an ovarian tissue sample was cancerous or non-cancerous (normal and benign ovarian samples combined) given the mean intensities of the image types, patient age and patient menopause status. Univariate logistic regression (ULR) was used to compare the mean intensity values of cancer vs. non-cancer samples for each image type in order to determine how well each individual image type performed. Previous research on cervical tissue has shown an effect of age and follicle stimulating hormone, an indicator of menopause, on fluorescence and reflectance spectroscopy¹¹⁵. Age and menopause status were examined for significant impact on image intensity in the ULR models for all image types so corrections could be made if necessary. Finally, two multivariate logistic regression (MLR) models were determined with best predictive values from small subsets of image types. One model was determined using fluorescence image types and the other used reflectance image types. In each model a small subset of image types was generated by exploring the relationships between image types using correlation and bivariate LR. Pairs of image types with very high correlation were determined and only the better fitting of the image types was retained in the model. This process was repeated to determine a small subset of image types with low cross-correlation for each MLR model. The receiver operating characteristic (ROC) curves and respective area under the curve (AUC) for each model was calculated using STATA's built-in post estimation command.

Both ULR and MLR were performed using robust variance estimates clustered on patient, to account for the potential correlation of tissues within the same patient.

2.7.3 Quadratic Discriminant Analysis on Ovarian Tissue

Quadratic Discriminant Analysis (QDA) was used to build n -dimensional quadratic surfaces to separate the data by pathology given image mean intensities from n of the image types. Recording and analyzing 18 image types is impractical for future clinical devices. QDA was used to determine which subsets of image types are most efficient at predicting the correct pathology. Each subset was tested using resubstitution of the data into the model.

3 Results

The number of samples, number of patients, mean age and age range for each tissue classification (tissue type and pathology) is shown in Table 1. Tissue samples were not available for 4 of the 28 consented patients. At least one sample of ovarian tissue was received from 24 patients, resulting in 47 pieces of ovarian tissue. Of the 47 samples, 35 were pathologically normal, 7 were cancerous (serous adenocarcinoma) and 5 had a non-cancerous benign condition (2 mucinous cystadenoma and 3 simple cysts). Fallopian tube samples were collected and imaged from 21 patients. In total, 31 fallopian tube samples were imaged with 21 being normal, 1 cancer (serous adenocarcinoma) and 9 benign (mild fibrosis). The age range was between 22 and 73 years with a mean age of 49.5.

Table 1 Characteristics of patients and tissues imaged.

Tissue Classification	Samples	Patients	Mean Age	Age Range
Ovary				
Benign	5	3	48.4	45-52
<i>Mucinous Cystadenoma</i>	3	2	50.7	50-52
<i>Simple Cyst</i>	2	1	45.0	45-45
Cancer (serous adenocarcinoma)	7	4	45.4	31-64
Normal	35	19	49.2	22-73
Total	47	24	48.6	22-73
Fallopian Tube				
Benign (mild fibrosis)	9	6	57.7	45-73
Cancer (serous adenocarcinoma)	1	1	64.0	64-64
Normal	21	15	43.6	22-71
Total	31	21	48.3	22-73

3.1 Tissue Sample Intensity Descriptive Statistics

The mean fluorescence and reflectance image intensity and standard error for normal, benign and cancerous ovarian and fallopian tube tissue samples is shown in Fig. 3 A and B, respectively. The absolute intensity values of fallopian tube samples is generally a factor of 2 to 3 times lower than the ovarian samples for all image types, but relative changes between pathologies are similar. For all image types and both tissue types, the image intensity from samples with benign conditions had a higher mean intensity than the normal samples, whereas cancerous samples had lower mean image intensity than normal samples.

3.2 Logistic Regression

ULR models were used to determine age and menopause effects as well as statistical significance between intensities for cancerous and non-cancerous ovarian tissue for each image type. Twelve patients were known to be pre-menopause, seven patients were known to be post menopause and five patients had uncertain menopausal status (2 undisclosed, 2 peri-menopause and 1 prior hysterectomy). All patients provided age information, which was considered a categorical variable (< 50 , ≥ 50). The cutoff was chosen because it completely separated all known pre- and post-menopausal patients. Age did not have a statistically significant impact on measured intensity in all image type ULR models ($p \geq 0.1$). Thus, age and menopausal status were removed from all following statistical analyses for simplicity.

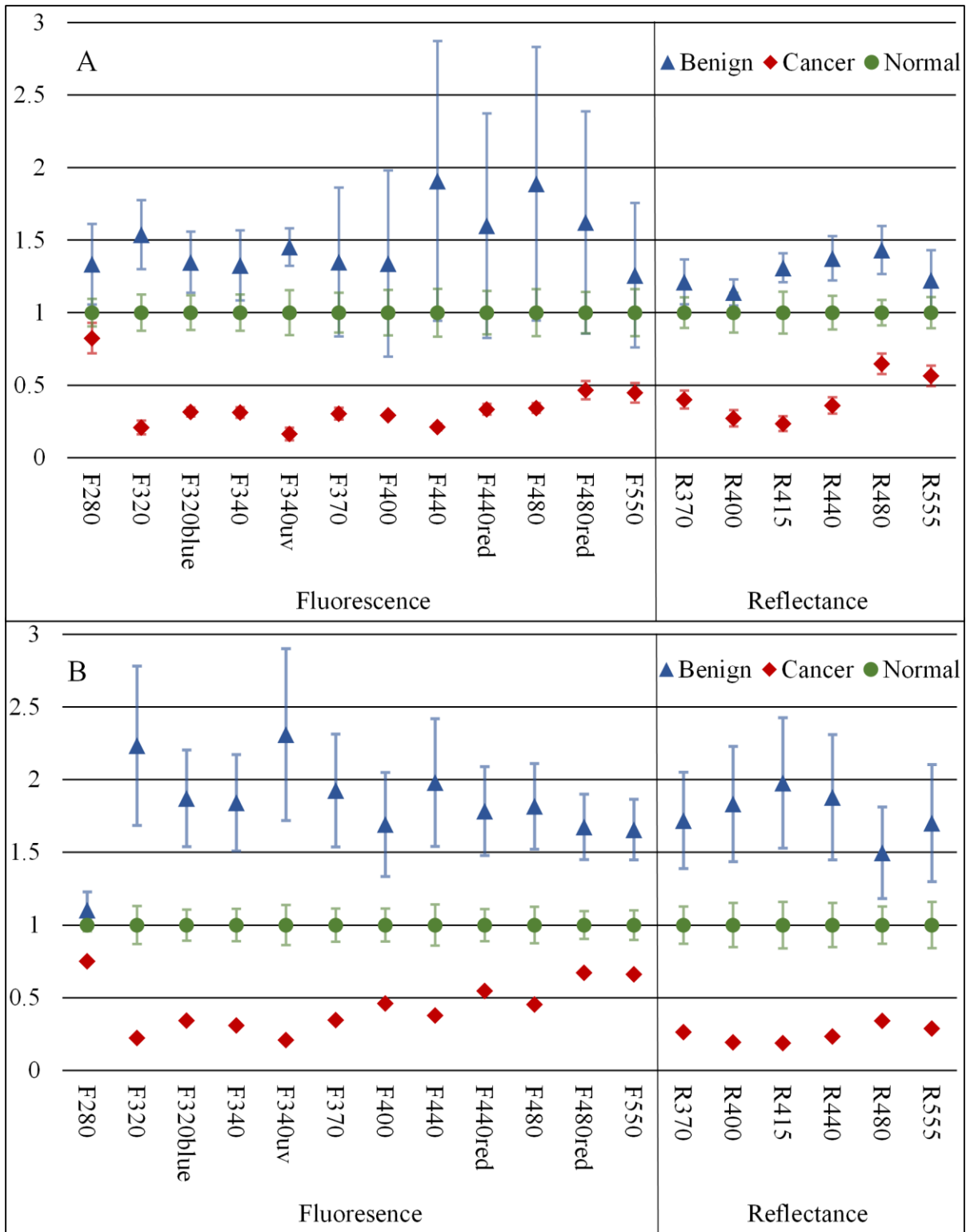


Figure 8: Mean A) ovarian and B) fallopian tube tissue intensity and standard error for each pathological group normalized to the normal group mean intensity for each image type. Standard error bars for ovarian tissue are robust standard error. Error bars are not shown for cancerous fallopian tube due to a sample size of one.

All ULR models demonstrated statistical significance ($p \leq 0.005$) between cancer and non-cancerous ovarian tissue except fluorescence using 280 nm excitation ($p = 0.163$). MLR models were developed to evaluate the predictive power of small subsets of image types. For the fluorescence data the best fitting MLR model was determined to use image types F440 and F480 ($R^2_{McFadden} = 0.4185$). For the reflectance data the best fitting MLR model used image types R440 and R480 ($R^2_{McFadden} = 0.5179$). The ROC curves, generated using STATA's built-in post estimation commands, for the fluorescence and reflectance models' ability to predict whether an ovarian tissue sample was cancerous are shown in Fig. 4. The AUCs were 0.9036 and 0.9464 for the fluorescence and reflectance models respectively. LR analysis examined cancer against non-cancerous samples, thus an image type's ability to discriminate between normal and benign pathologies was not considered.

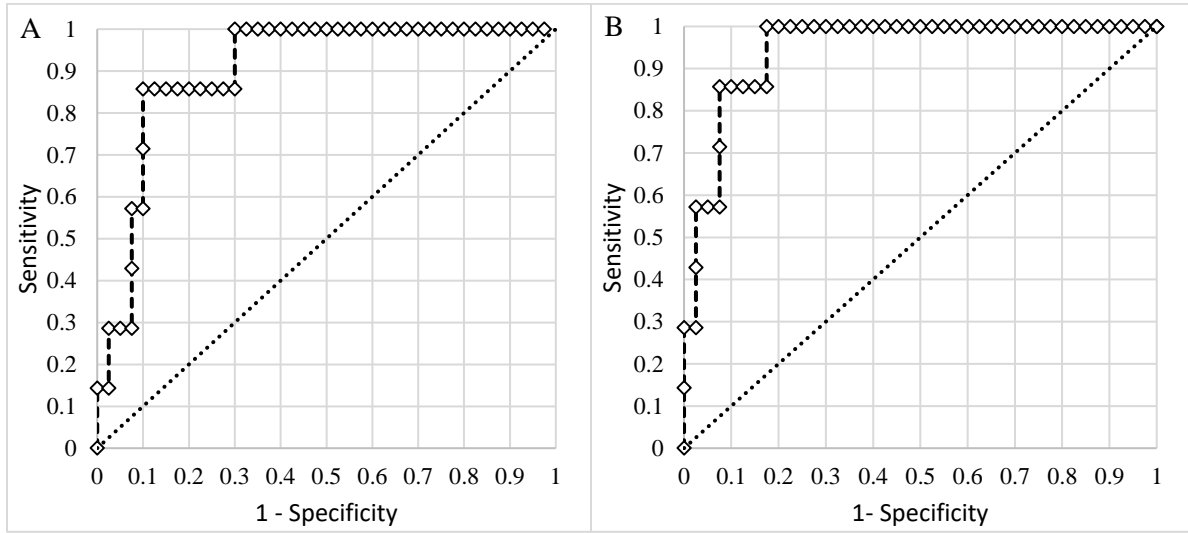

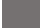


















Figure 9: ROC curves for ovarian tissue MLR models. Dotted diagonal lines represent a model with no predictive power (AUC of 0.5). A) Fluorescence model using image types F440 and F480 with AUC of 0.9036. B) Reflectance model using image types R440 and R480 with AUC of 0.946.

3.3 Quadratic Discriminant Analysis

QDA was applied to the ovarian data with the mean intensities from each of the 18 image types being the independent variables. Age and menopause status were omitted based on the results from the ULR models. QDA was run on every possible subset of image types from size 2 to 18. There are 2^{18} possible subsets for a set of 18 elements. Eliminating the 1 way to choose zero elements from the set and 18 ways to choose one element resulted in 262,125 subsets of image types analyzed with QDA. Multivariate normality, an assumption of QDA, was tested for each subset using the Mardia kurtosis test. For a subset of n image types QDA determines the two n -

Table 2 Frequency of occurrence of image-types in QDA-determined high predictive power image subsets.

Image Type	Frequency	
F280	328	
F320	299	
F320blue	436	
F340	488	
F340uv	334	
F370	264	
F400	407	
F440	394	
F440red	414	
F480	750	
F480red	414	
F550	376	
R370	485	
R400	1216	
R415	1257	
R440	576	
R480	412	
R555	308	

dimensional surfaces that best separates all tissue samples by pathology. After the model was created from the tissue sample image intensities, each sample was tested by resubstitution into the model to determine whether the model accurately classified the tissue. The classification accuracy and type of misclassifications for each QDA model was recorded. A good subset of image types was defined as one that had a p-value greater than 0.1 in the kurtosis test and had at most one tissue sample misclassified by resubstitution. There were 56 subsets that passed the Mardia kurtosis test and had zero resubstitution error. The subsets ranged in size between 5 and 9 image types. Similarly there were 1256 subsets

with 1 resubstitution mistake ranging in subset size 4 to 10. Subset sizes of 6 and 7 produced the majority of good subsets. The frequency that each image type appeared in a good image subset is listed in Table 2.

3.4 Qualitative Visualization

Of the seven image type subsets of size 5 determined by QDA to have zero resubstitution error, the representative subset of image types F320blue, F370, R400, R415 and R480 is shown in Fig. 5. Three representative tissue samples are shown of each broad category of pathology (normal, benign, cancer). Of the five benign samples the middle three in terms of average image intensity were chosen. The samples with the second, fourth, and sixth most intense images were chosen from the seven available cancer samples. The three normal samples were chosen at approximately the 25th, 50th and 75th percentile in average image intensity of all normal samples. Thus the samples are representative of the range of intensities from each pathologic group. The reflectance images have much higher intensity than fluorescence images so a logarithmic transformation has been applied to the image for display purposes.

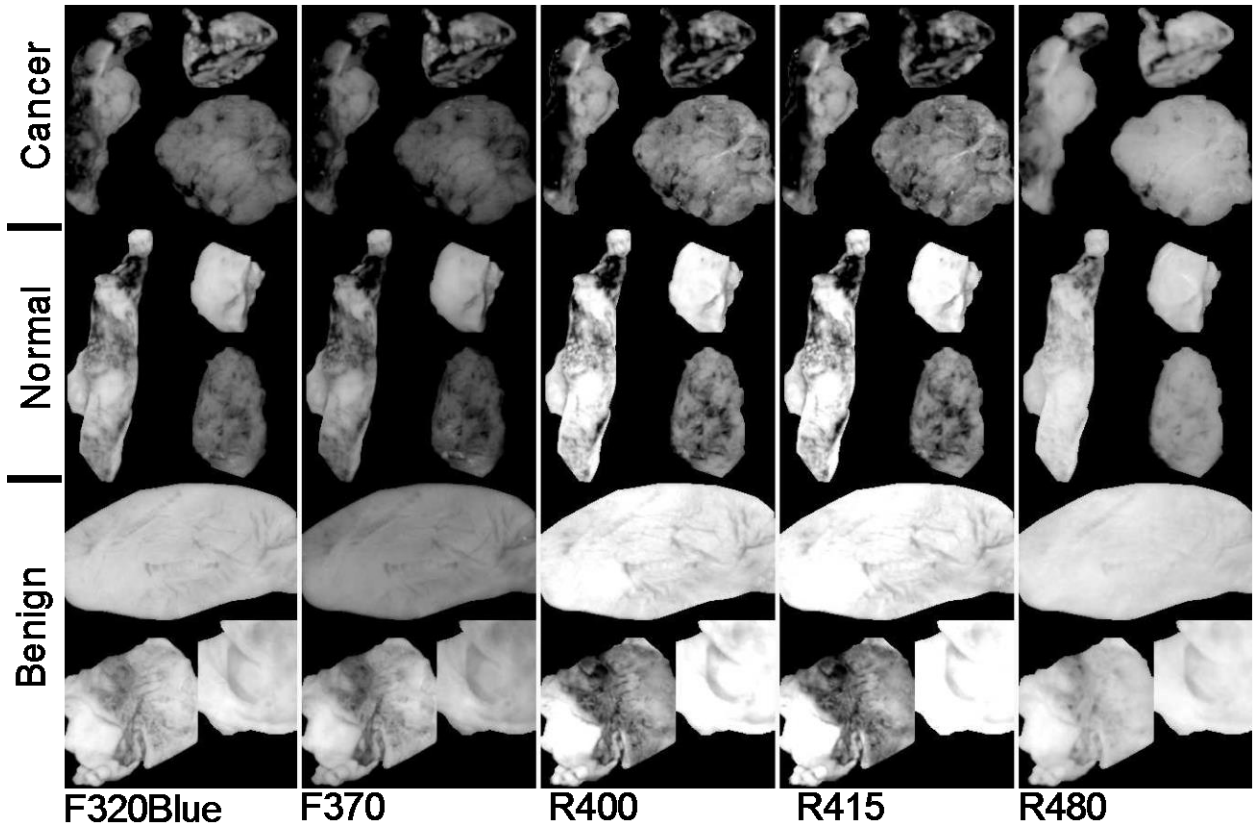


Figure 10: Representative images of ovarian tissue. Within each column the top three tissues are cancer samples, the middle three are normal samples and the bottom three are benign samples. The three samples for each pathology are representative of the range of intensities measured for the given pathology. From left to right the columns are image type F320blue, F370, R400, R415 and R480. The QDA model using these 5 image types had 0 resubstitution errors. The images are saved as floating point TIFF files for statistical comparison. The significant differences in intensities and dynamic range between image types require the images to be log scaled for visualization with the same window and level settings.

4 Discussion

The results of the *ex vivo* study support further development of multispectral fluorescence and reflectance imaging to predict ovarian and fallopian tube tissue pathology. Both the LR and QDA models showed promising results. The MLR models showed strong classification performance ($AUC > 0.9$) for detecting cancer can be obtained using only the image intensity from reflectance or fluorescence images at excitation wavelengths of 440 and 480 nm, whereas QDA showed perfect classification of normal,

cancerous and benign tissues using as little as 5 reflectance and fluorescence image types. A limitation of this study was the small number of benign and cancerous tissue samples which required tissue samples to be classified in broad pathological groups for analysis. Further, a detailed statistical analysis of fallopian tube data was not possible due to having only 1 cancerous sample. Further study with a larger number of samples is needed to corroborate these findings, however the good results and consistent trends provide confidence in MFI's ability to discriminate between normal, benign and cancerous ovarian tissue.

The overall decreased image intensity in cancerous tissue and increased intensity in benign tissue aligns with expected changes in tissue optical properties²⁷. Tissue pathology determines tissue composition and thus the concentration and distribution of fluorophores as well as the optical absorption and scattering coefficients. The dominant absorber in the UV and visible spectrum is hemoglobin (Fig. 1B). Neovascularization is a hallmark of cancer and is expected to increase the blood volume fraction and thus absorption in cancerous tissue. Examination of Fig. 3 shows that cancerous tissue has the lowest relative reflectance image intensity at 415 nm, near the hemoglobin absorption peaks, and the highest relative reflectance image intensity at 480 nm, which is near a trough in hemoglobin absorption. Cancerous ovarian tissue has been shown to have significantly less collagen content than normal tissue which is correlated with decreased scattering coefficient¹¹⁶. Thus, the increased absorption and decreased scattering are expected to decrease reflectance image intensity. Increased absorption will also cause decreased fluorescence image intensity due to overlap of the hemoglobin absorption spectrum with both the excitation and emission wavelengths. Upon visual evaluation of the H&E slides, all benign

ovary (3 mucinous cystadenoma and 2 simple cysts) and fallopian tube (9 mild fibrosis) samples had increased collagen relative to normal. The strong scattering and fluorescence of collagen may be the mechanism behind the benign samples having increased reflectance and fluorescence image intensity.

All image types except F280 showed statistically significant discrimination between cancerous and non-cancerous ovarian tissue in the ULR models. For the MLR and QDA models image types with excitation or emission wavelengths at or around the hemoglobin absorption peaks and troughs generally showed the strongest discrimination. Image types R400 and R415, both sampling the left side of the blood absorption peak, were included in over 92% of the good QDA subsets. The illumination wavelengths of 440 and 480 nm were chosen in both the fluorescence and reflectance MLR models as the best predictors of tissue pathology. The process of determining variables for the MLR models eliminated image types with high covariance and thus redundant information. Since 440 nm is near the deoxyhemoglobin absorption peak while 480 nm is in a trough, the image types acquired with these illumination wavelengths may present the strongest and weakest effects of blood absorption respectively in these samples.

Of the fluorescence image types, F480 was determined a strong discriminator by MLR and most frequently occurred in good QDA subsets. Unlike the other wavelengths with strong discrimination between pathology, the excitation and emission band of F480 are expected to have relatively low influence from blood absorption. The fluorescence from F480 has been shown to be higher for normal than cancer tissue in previous fiber probe studies, due to the primary excited fluorophores of FAD and collagen²³.

Of interest are the possible reasons F280 was the only image type not showing significant discrimination between cancerous and non-cancerous tissue in the ULR models. The excitation and emission bands are moderately affected by hemoglobin absorption. However, previous studies on colon tissue with the same imaging device have shown that optical penetration decays exponential with a $1/e$ decay at approximately 105 microns for 280 nm excitation and approximately 2 mm for 440 nm excitation¹¹⁷. Biological tissue has increased scattering with decreased wavelength, and in the ultraviolet spectrum, tissue scattering significantly limits optical penetration. Anatomically the ovarian epithelium is about 100 microns thick and lacks vasculature in normal pathology. Thus hemoglobin absorption effects are expected to be minimal for 280 nm excitation. Previous studies have indicated that excitation below 300 nm produces the highest fluorescence in cancerous ovarian tissue and lowest in benign tissue, when performing point spectroscopy²⁷. An excitation wavelength of 280 nm primarily excites the amino acid tryptophan which is believed to be more abundant in cancerous tissue due to an increase in protein synthesis^{27,39}. Imaging geometries have been shown to be more sensitive to blood absorption effects compared to probe spectroscopy¹¹⁸. Increased angiogenesis in cancerous samples may bring vasculature within 100 microns of the surface. It is possible that the attenuating effects of blood absorption (enhanced in our illumination-detection geometry) are countering the increased fluorescence from amino acids in the cancerous samples, and the net result is a similar intensity for all pathologies at F280. Prior studies on colon cancer using the multispectral imager used in this study have also shown slightly decreased intensity for cancerous tissue for F280 images⁹⁸.

Further examination of the QDA results provides additional insight. Of the top seven most frequently occurring image types (F320Blue, F340, F480, R370, R400, R415 and R440), only 2 of the 1312 good subsets were constructed exclusively of these image types. The full set of 7 and the subset excluding R440 both passed the kurtosis test and both only misclassified one benign ovary tissue sample as normal. Thus the best performing sets included some, but not all of the most frequently occurring image types. Of the image subsets of size five or six that had perfect resubstitution, all 18 image types occurred at least once. This finding is likely due to two reasons. First, the illumination and fluorescence emission wavelengths have already been chosen based on their ability to sample the most commonly occurring chromophores and fluorophores in tissue. Therefore it is not surprising that they all perform well. Also, the MLR modeling identified high covariance between many image types, suggesting that similar performance could be obtained with varying image types.

While the primary analysis focused on the ovarian tissue samples, the fallopian tube samples' descriptive statistics show trends very similar to those of the ovarian samples. The primary difference between the tissue types is the uniformly reduced image intensity for fallopian tube samples. The reduction in intensity may be primarily due to a naturally occurring higher concentration of hemoglobin and decreased collagen in the fallopian tube samples.

In addition to the limited number of benign and cancerous samples discussed above, there were two other limitations of this study. First, since no effective method of detecting early stage ovarian cancer exists, it is challenging to acquire early stage cancer samples, and all cancerous samples used in this study were advanced-stage. It is unknown if early

stage cancer has the same imaging characteristics. Most of the surgeries contributing tissue to this study were prophylactic for high risk women or to address other gynecological issues. In some cases tissue was received from patients with confirmed ovarian cancer, but the particular samples received for the study did not show signs of cancer upon independent pathological evaluation. These challenges make studying human ovarian cancer development difficult. The investigators have previously shown the ability to follow disease development in a mouse model of ovarian cancer¹⁰⁷, however that carcinogen-driven model did not mimic the usual development of ovarian cancer in women. Imaging of a mouse model that accurately mimicked the development of human ovarian cancer would enable the determination of the earliest stage at which MFI could accurately detect cancer.

Second, tissues were measured post-resection and do not reflect the *in vivo* state. All samples were imaged within two hours of removal and most typically from 30 to 60 minutes after removal. In research on resected human colon tissue it has been noted that different fluorophores decay at different rates after resection. For example, NADH decays exponentially with a half-life of 118 minutes while collagen and FAD remain relatively constant^{119,120}. One sample in this study containing two ovaries and two fallopian tubes was imaged twice with a four-minute delay between acquisition sequences. With all other variables being equal the average image intensity of ovarian samples 1 and 2 decreased by 0.09% and 0.90%, respectively, while the average image intensity of fallopian tube samples 1 and 2 decreased by 3.27% and 3.34%, respectively. These results suggest that future studies should endeavor to image samples as soon as possible after resection and at a

consistent time after resection. They also suggest that there will be differences between image intensities seen in this *ex vivo* study and future *in vivo* studies.

Future work will involve more sophisticated image processing and hardware modifications. Ratiometric imaging can be utilized to help decouple the effects of tissue absorption and scattering on fluorescence. For example, fluorescence images can be divided by green reflectance images (R555) to help isolate relative intrinsic fluorescence strength from blood absorption^{117,121,122}. Using this ratiometric imaging approach, it may be possible to create image contrast proportional to the changes in endogenous fluorescence demonstrated by spectroscopic analysis^{27,39,98}.

Work to integrate the MFI imaging system into an endoscope designed to image inside the fallopian tubes and at the ovary is in progress¹⁰⁰. The xenon arc lamp can be replaced with laser sources coupled into a multimode illumination fiber. Based on laser availability, wavelengths of 250 nm (tripled Alexandrite), 375 nm (doubled Alexandrite), 442 nm (He:Cd), 543 nm (green He:Ne) and 638 nm (diode) are initially planned for an endoscopic system. These wavelengths provide images most similar to the F280, F370, F440, F440red, F555, R370, R440 and R555 image types utilized in this study. Running the QDA model with these eight image types produced six multivariate normal subsets with only two resubstitution errors (two benign tissue samples misclassified as normal- all normal and cancer samples were accurately classified), suggesting that these wavelengths are reasonable initial choices. With a large field of view, MFI will also serve for navigation. Endoscopic *in vivo* imaging adds the challenge of a complex tissue geometry being imaged over a wide field of view and with a large depth of focus. Correcting the dynamically changing non-uniform radiometric distribution across the image for comparison of absolute

tissue intensities is impractical. In addition to the benefits of ratiometric imaging mentioned above, using real-time ratiometric imaging can help normalize the image intensities across the field. Proper ratiometric combination of image types can create images in which suspicious regions have high relative contrast compared to adjacent normal tissue. A high resolution technique (optical coherence tomography) can be added to interrogate suspicious areas, potentially heightening accuracy of the overall system. Adaption of the system for future *in vivo* fallopian tube and ovary endoscopic imaging may provide a minimally invasive and highly sensitive screening device for ovarian cancer without the use of exogenous contrast agents.

A.2. Data Storage

The details on where to find the raw data, images files and manuscript files follow.

A.2.1. Raw data and analysis images

Data associated with this project includes images, image segmentation polygons and an excel file compiling all patient data and fluorescence intensity statistics for each tissue sample. All raw data are located in the lab storage drive in the Parent folder path:

`'\Projects\Grants\DoD_Falloposcope\Design_Proximal\MFI_ImageAnalysis'`

Within that folder image data is saved in a 'Raw_Data' folder and a 'PostProcTiffNoStretch' folder. The former is the raw data acquired by the MFI system. The latter are the images after processing to normalize for system performance fluctuations and saved as 16-bit floating point TIFF images without any histogram manipulation. The pixel intensity values from these images are used for data analysis in the manuscript. Within each of the folder are subfolders for each patient labeled with 4 digit number. The last two numbers are the patient number and match the patient consent and health history forms. The first two digits are typically zero. If there was an error in imaging and the image acquisition sequence had to be repeated the first number is a 9. If there was an error during normalization processing the second number increments for each processing run.

Within each patient subfolder in the 'PostProcTiffNoStretch' folder are additional subfolders for each set of tissues measured for that patient. For example, if five tissue samples were imaged for the patient with 3 being imaged in the first acquisition sequence and 2 being imaged in the second acquisition sequence then there will be two subfolders labeled 'M1' and 'M2'. There are 18 normalized images for each acquisition sequence. Each TIFF images is available in the 'M#' folder along with a co-registered image stack that can be opened in ImageJ software.

The multipoint polygon and ROI feature of ImageJ were used to outline each sample tissue in the image stack and save the outlines for future analysis. Two sets of outlines were made for each

images stack. One outline the entire visible tissue sample and the other only outlining the top surface of each sample. Both sets of ROI polygons are saved in each measurement folder along with the images.

For both sets of ROI the area of the ROI (pixels) was recorded in addition to the mean, standard deviation, minimum, maximum and median intensity of pixels within the ROI. This was done for every tissue sample in all eighteen images types. All of the statistics were compiled in an excel sheet titled 'IntensityAnalysis' in the excel file labeled 'Specimen_Database.xlsx' located the Parent folder. Also added to 'IntensityAnalysis' sheet is a ID number for each measurement, the image acquisition date, patient number, measurement number, patient age, menopausal status, tissue type and location, imaging technician notes, independent pathological diagnosis, image type (which gives excitation and emission ranges) and a filename including ROI label for data verification. Other sheets in folder include more detailed information on patient health history, pathology results, image type wavelengths information and various preliminary analyses. The data used for final analysis was the mean intensity for the whole tissue ROI.

The images and spreadsheet are not reprinted here as their printed volume would increase the length of this document an order of magnitude. Specific data can be electronically made available upon request.

A.3. Standard Operating Procedures

For this project one standard operating procedure (SOP) copied below was developed according to laboratory protocol titled 'Imaging procedure for *ex vivo* tissue on the multispectral imaging system.'

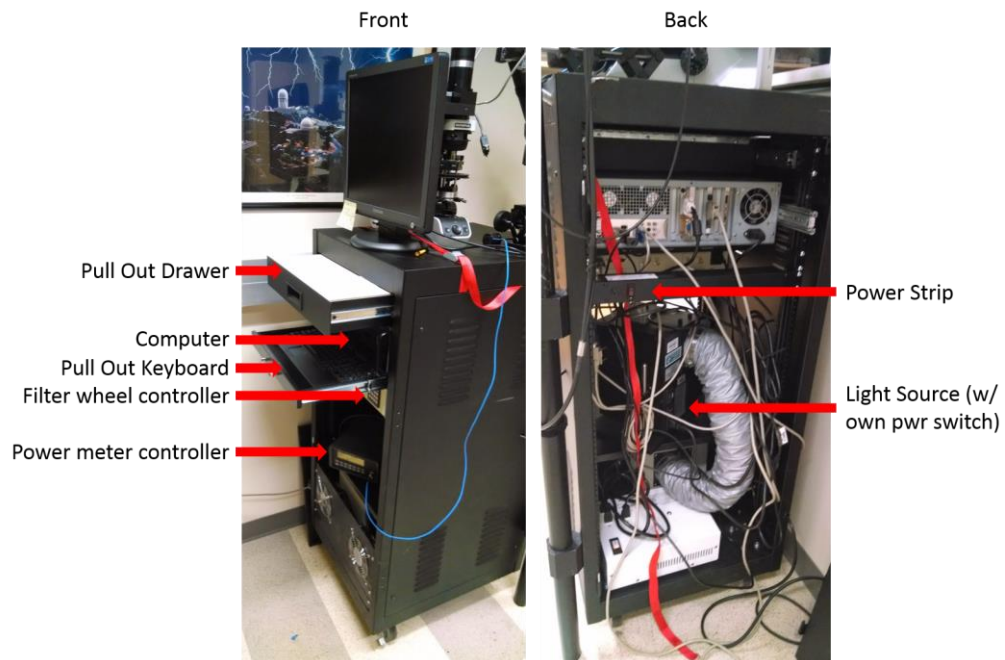
Standard Operating Procedure University of Arizona Biomedical Engineering Program

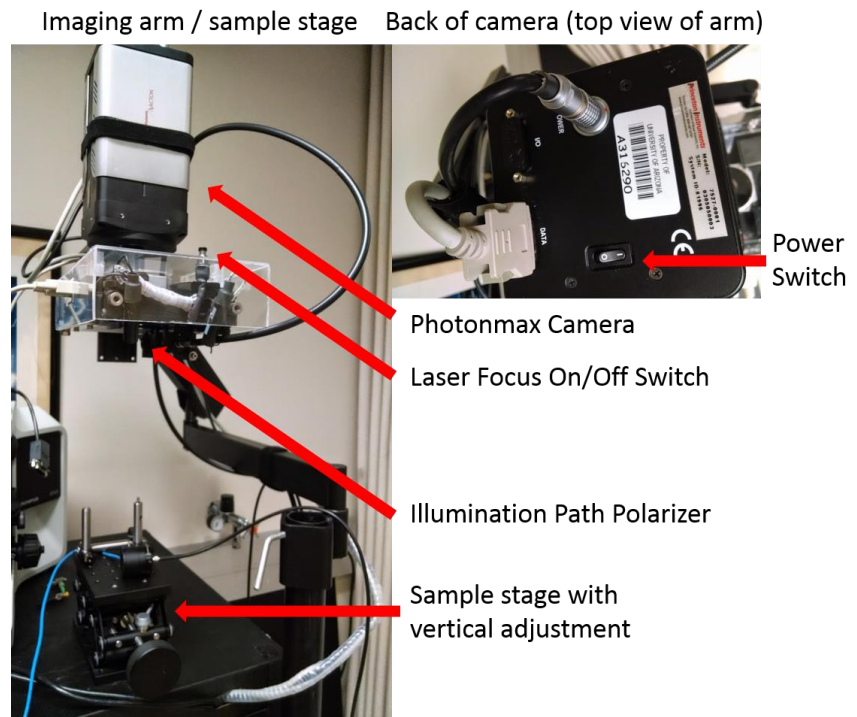
SOP # B02-010

Imaging Procedure for *ex vivo* tissue on the multispectral fluorescence imaging system

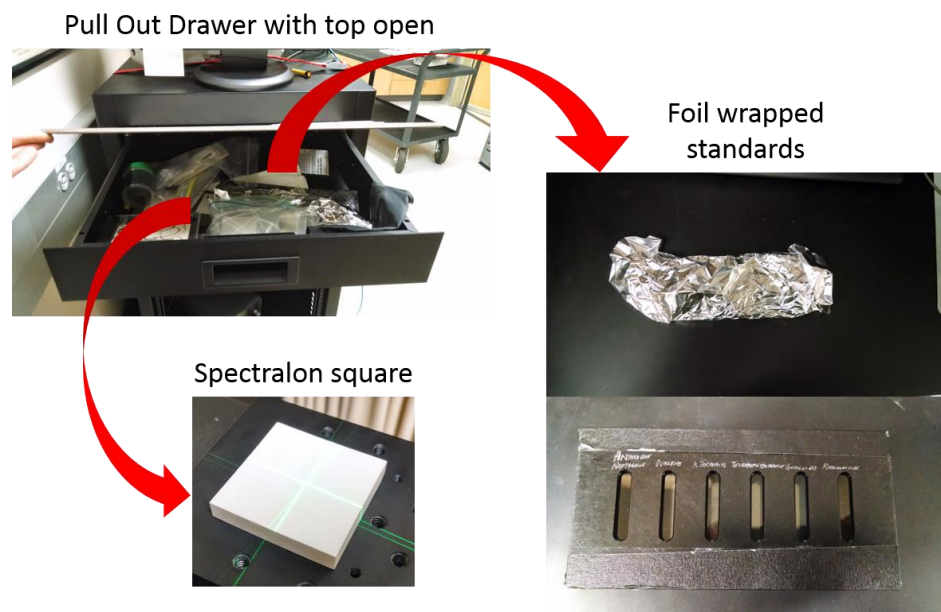
A. Supplies/Equipment:

Multispectral Imaging System and knowledge of what components are what.





Make sure the white spectralon square is in the pull out drawer. It should be stored in a zip lock bag. Also make sure the foil wrapped standards are in the drawer (keep in foil except during standards measurements). These are necessary to standardize intensity measurements of tissue over time. To close the drawer you need to release the locking mechanism by pushing in a metal tab on the left runner.



Make sure you have your tissue sample prepared on a non-fluorescing black cloth. Field of view is approximately 4cm by 4cm. See example white light image of ovarian tissues below.



B. Procedures:

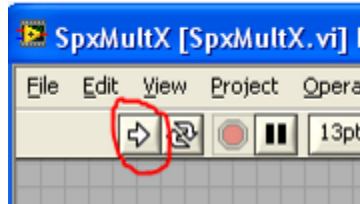
THIS SYSTEM BELONGS TO DR. UTZINGER'S LAB. DO NOT USE WITHOUT FIRST DISCUSSING YOUR PROJECT WITH HIM AND RECEIVING HIS APPROVAL. THE SYSTEM IS OFTEN IN ALTERNATE CONFIGURATIONS FOR OTHER EXPERIEMENTS. MAKE SURE IT IS PROPERLY SET UP FOR EX VIVO IMAGING AND/OR THAT CHANGING THE CONFIGURATION WILL NOT DISRUPT ANYONE ELSE'S RESEARCH.

Prepare / Turn on the system.

1. Remove dust cover from the imaging arm.
2. Make sure stabilizing pole (that imaging arm is attached to) is in contact with the ground to mitigate movement during imaging.
3. Turn on power strip in back panel of cart (this needs to be done before turning on light source).
4. Turn on camera using switch on the back of the camera. The camera needs time for the cooled CCD to reach its target temperature. (See 'back of camera' picture above for power switch location).
5. Turn on light source in back panel of cart. The light source needs ~20 minutes to warm up before imaging tissue or standards.
6. Turn on computer and monitor on front of cart.
7. Turn on Sutter filter wheel controller.
8. Turn on power meter controller (push in red button).
9. Login to computer using: User name: 'OCTlab', Password: 'coherence1300', Log on to: 'SPX-UV (this computer)'.
10. Open the SpxMultX shortcut on the desktop.



11. Once labview is open click the white arrow button in the top left of the screen to initialize the SpxMultX program within labview.

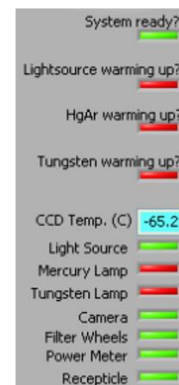


12. Now click the 'power switch' in the bottom left corner of the lab view window.



13. The code will display a series of messages most of which you have already done or can ignore. Click okay to close each message.
14. At this point the software is prepped for imaging but it is important to make sure the hardware is also. The software as a series of indicators on the left side to determine if the system is ready (see picture on right). The light source needs to have been powered on for at least 20 minutes before imaging. The CCD temperature should be approximately -65 degrees Celsius before you begin imaging. You should manually check these things in addition to checking the indicator lights.

Indicator lights when system is ready.



General Guidelines to Imaging on the System

- There are five standardization/normalization imaging scripts you will need to perform so tissue images can be normalized against fluctuations in hardware performance. There is a separate script for imaging your tissue sample.
- The five standards scripts and the tissue script can be run in any order, but should be ran as close together as possible so the system is in the same condition during all measurements.
- Do not use any additional software while running labview. Labview registers keyboard shortcuts even if it is not the active window. For example, if you type notes in notepad and hit 'enter' while a labview prompt is asking a question it will select the default option.
- Lab view pop-up windows often get lost behind the main labview window. Use keyboard shortcut 'alt+tab' to return the popup to the front so you can select an option before continuing.

- The side of the camera that mounts to the arm is the bottom of the field of view as displayed in lab view. Use this reference to orient your sample and the standards.
- The green laser pointers are used to focus the image. The location where all laser lines intersect is the focused center of the FOV. Only have on when necessary as battery life is short. ALWAYS turn them off BEFORE imaging. Leaving them on will create false measurements.
- Sometimes you will need to discard the results after running a script. See step 7 of the ‘run standards scripts’ section below for proper procedure in this situation.
- There is a linear polarizer located in the illumination path underneath the emission filter wheel (just below camera). Each script will indicate whether to insert or remove polarizer from illumination path with dialogue windows. These are important to comply with. Move polarizer gently so as not to jar the camera position between measurements. See picture:

Gently tug polarizer to allow it to hang out of illumination path

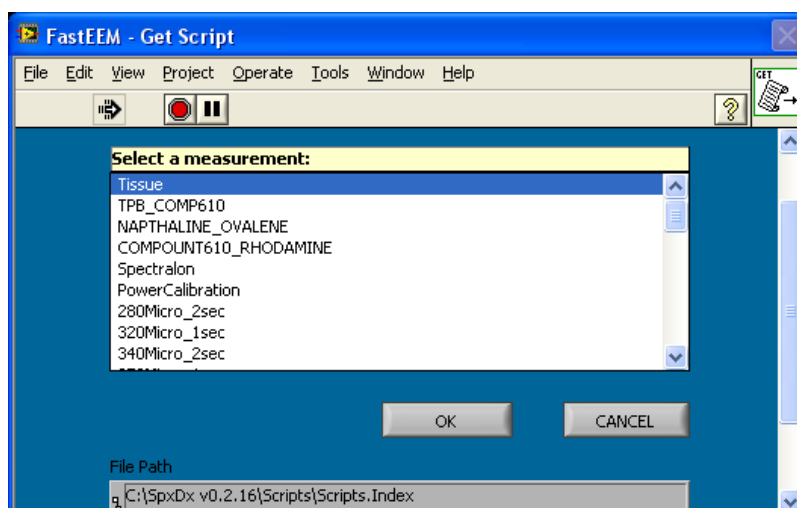


Gently push polarizer back up until it clips on the rails to put it in illumination path.



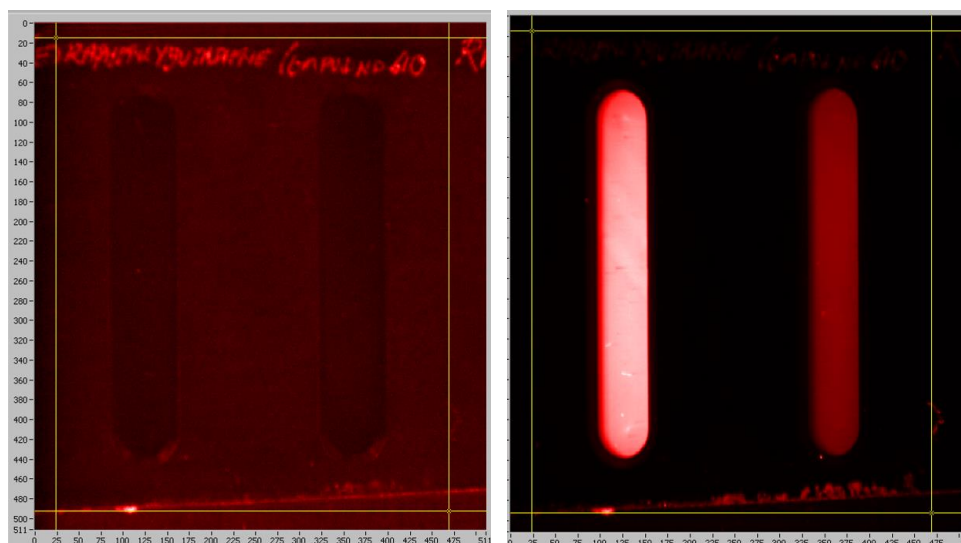
Choose script to run

Click the large green script button on the center left of the labview window to open the scripts options. The ‘Tissue’ option should be used to image a tissue sample. The options ‘TPB_COMP610’, ‘NAPHTHALINE_OVALENE’, ‘COMPOUND610_RHODAMINE’, ‘Spectralon’, and ‘PowerCalibration’ all need to be run for normalization of tissue images. They can be run before or after the tissue imaging, but should be done as close to tissue imaging as possible for accuracy.

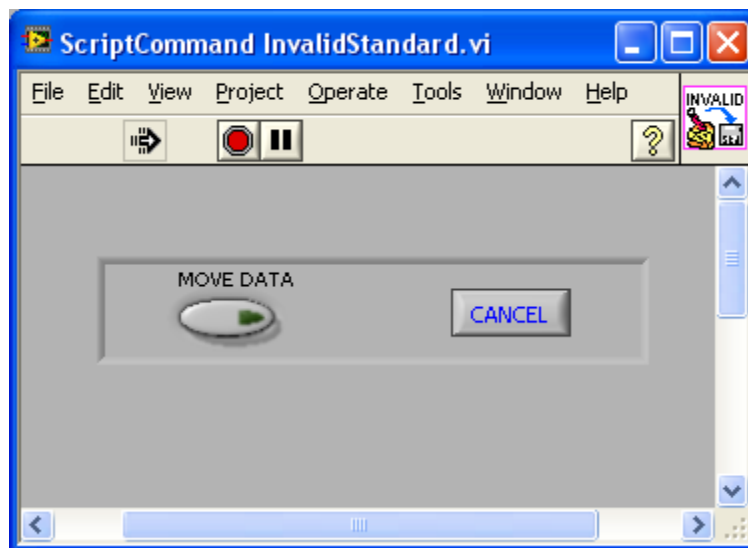


Run standards scripts (TPB_COMP610, NAPHTHALINE_OVALENE and COMPOUND610_RHODAMINE)

1. For simplicity this SOP uses TPB_COMP610 as an example.
2. Unwrap the standards from the foil and place them on the sample plane with the text in the top of the labview image (text on sample stage is on opposite side of camera from mounting arm). The standards box has 6 labeled standards, but only two simultaneously fit in the FOV. The proper two are given by the script file name. For example, Tetraphenyl Butadiene and Compound 610 should be in the FOV for the TPB_COMP610 script. See picture below.
3. Turn on the green laser pointers to focus the camera on the standards. Adjust the height of the image plane until all the laser lines intersect in center of FOV. This is easiest with a sample stage with vertical translation. However it can be performed by adjusting the imaging arm if necessary. Turn off focusing lasers once standards are focused. See picture below.



4. Once the standards are aligned as pictured click yes to the 'are you ready' dialogue box. Follow instructions for proper polarizer placement. The program will then pop up a dialogue box asking if 'image framing and focusing are finished? Lights out?' Usually this will take a sample image so you can see if the standards are indeed properly placed. If you realize after taking the measurements that they were wrong the code gives you the option to redo the measurement. Turn out the lights. Click okay to begin measuring the standards.
5. During the process the system will take a series of images that look like this:
6. The standards do not need to be perfectly vertical or centered to provide accurate information. However, they should look reasonably close the images above. If they did then click yes to save the measurement.
7. If there was an issue during the measurement and you need to redo the process follow these steps exactly. Click no to discard the data. The next dialogue box asks whether you want to save the data in an invalidated folder. YES, you do want to move data to invalidated folder. After this a second dialogue box pops up asking effectively the same thing (see picture below). IMMEDIATELY WHEN YOU CLICK 'MOVE DATA' IN THIS DIALOGUE BOX THE SYSTEM WILL START IMAGING THE STANDARD AGAIN. So, before you click 'move data' ensure you have fixed the problems and turned the lights out. Then click 'move data.'

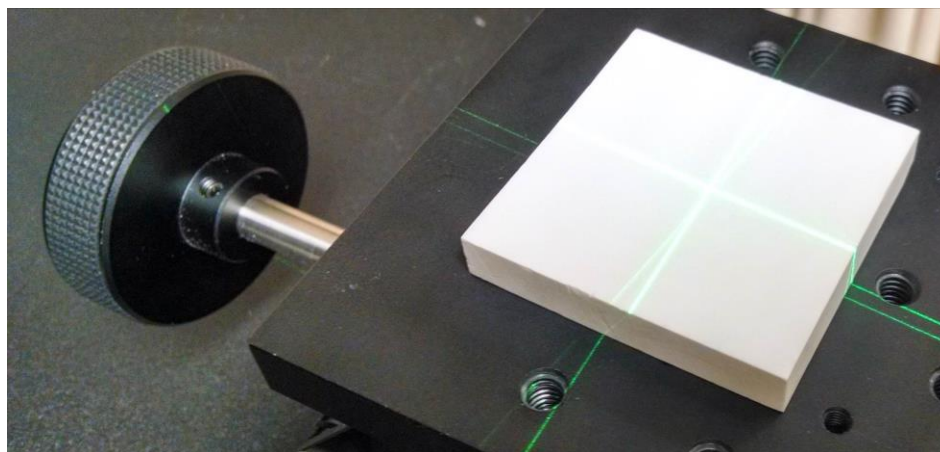


8. Repeat this process for NAPHTHALINE_OVALENE and COMPOUND610_RHODAMINE scripts. Ensure the proper to standards are in the field of view for each script.
9. Immediately after finishing imaging the standards put them back in foil and place them in the top drawer of the cart. They are susceptible to photo bleaching and must be kept in the dark to maintain long term accuracy.

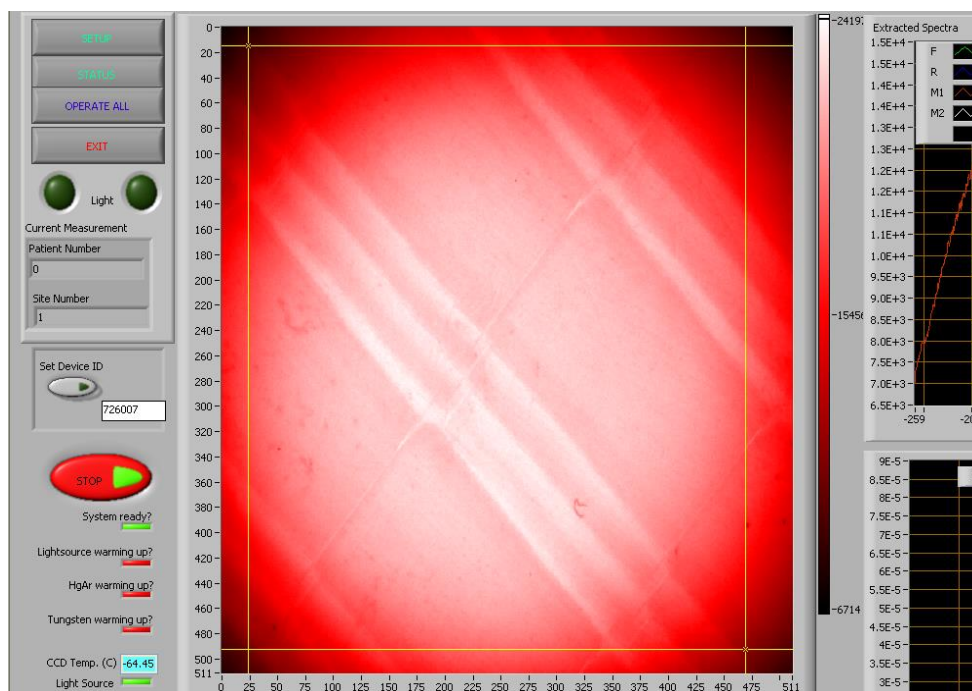
Run Spectralon script

1. Use the green script button to open the scripts options. Select 'Spectralon' and click okay.
2. This script images the flat white square for image uniformity. It is stored in a plastic bag in the top drawer of the cart. Remove it being careful to only touch the sides. Place it in the center of the camera FOV and use the laser pointers to focus the system on it. It should have an arrow on the side indicating which face is up. Remember to turn off laser pointers once focused. If the square is dusty/dirty use compressed air to clean. Isopropyl and lens cloth may be used if necessary.

3. Ensure polarizer is out of imaging path and click through dialogue windows.



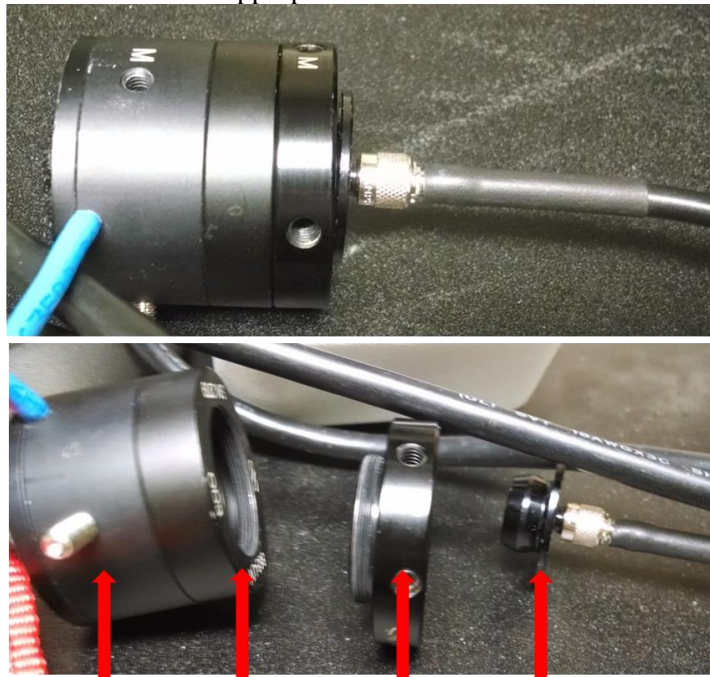
4. After a few images the code instructs you to place polarizer in image path. Do so and click okay. See picture below for a typical image during this process.
5. Once the measurements are finished click the appropriate option about being done or not. If the measurements need to be redone follow the same procedure as discussed in See step 7 of the 'run standards scripts' section. Properly store spectralon square in zip lock in top drawer.



Run 'PowerCalibration' script

1. Open the PowerCalibration script.
2. This script requires imaging of the power meter in a variety of configurations. Refer to the picture below to familiarize yourself with the codes terminology.

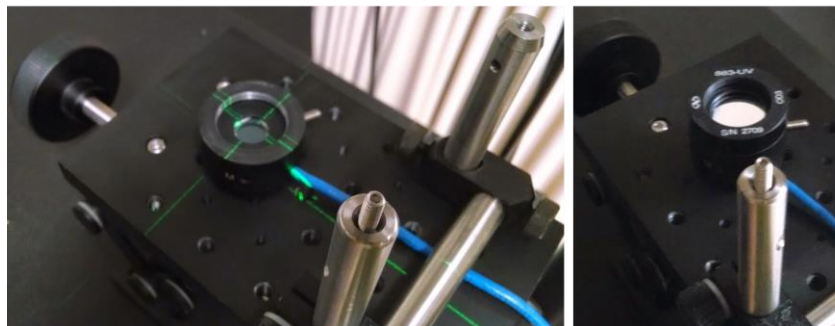
3. The code instructs you remove the 1st ring of the power meter and place the power meter in the center of the image plane. It is easiest to place the power meter in the center of the FOV by removing the first and second ring (attenuator) and using the laser pointers to get the actual power meter detector centered and focused. The power meter will beep during this process because the power of the laser pointers is saturating the detector. Use something to hold the power meter cord down so that it stays level and stationary. Then turn off the laser pointers and REPLACE the 2nd ring (attenuator) for accurate measurements. See picture below.
4. Turn off lights, click through dialogue boxes following instructions about polarizer placement and take measurements.
5. As with other calibrations click yes done or no discard as appropriate (See step 7 of the 'run standards scripts' section above for invalidating data).
6. Now reattach 1st ring and feedback fiber to power meter and click okay through dialogue boxes. This step only measures the amount of power going through feedback fiber to power meter and doesn't record any images.
7. Save or discard measurements as appropriate.



Power Meter 2nd Ring 1st Ring Feedback Fiber

Power meter centered / focused with both rings removed, cord held down to keep stationary.

2nd ring replaced, focusing lasers off. Ready for measurement.

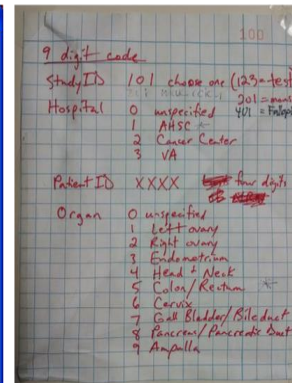


Run 'Tissue' script

1. Use the green scripts button to open the scripts menu and select 'tissue'.
2. The script asks if you are ready to set patient data. Select yes. This opens a pop-up window to create a patient barcode. The barcode is a 9 digit code where the first three digits are the study ID (401 for human ovary/fallopian tube), the fourth digit specifies the hospital, the next four digits are the patient number (0099 for patient 99) and the final digit specifies the tissue type. Use the cheat sheet taped to the pull out drawer for help. The study and patient number are critical to get correct. If you need to redo a patient measurement and do not want to override the early measurement make the first digit of the patient ID a 9. For example, 9099 for patient 99. After you type the 9 digit barcode hit the 'enter' key above the 'shift' key. If you accidentally hit the numpad 'enter' key you will need to return the cursor to the end of the barcode number and hit the proper 'enter' key. Then select 'Create Data Directory'.

Create bar code dialogue box

Cheat Sheet taped to pull out drawer



3. Remove polarizer. Ensure tissue is centered, focused, and in FOV. Make sure the feedback fiber is connected to the power meter. Turn out the lights and click okay through the dialogue boxes.
4. After a series of images are taken the code prompts you to replace polarizer. Do so and make sure the lights are out before you hit okay.
5. Choose to keep data or discard as appropriate (See step 7 of the 'run standards scripts' section above for invalidating data).

Exiting the software and shutting the system down.

1. No script should still be running (the large button in the middle left of the labview window will be green and say 'scripts'. If a script is running it will be red and say 'stop'). If any script is still running make sure you haven't lost a dialogue box by using the 'alt+tab' keyboard shortcut. If need to stop a running script for some reason you can hit the large red stop button.
2. Click the 'power switch' in the bottom left of the screen. Click through the series of dialogue boxes. You can mostly ignore them and follow these instructions instead.
3. At this stage you can monitor the CCD temperature. It should start rising. Do not flip the power switch on the back of the camera yet.
4. Turn off the filter wheel controller and power meter controller.
5. Turn off lamp source in the back of the cart. (Leave the power strip on for now – it powers the computer and the ozone filter).
6. Copy your data from the local computer to the server. Consult with the lead student on the project or Dr. Utzinger on the proper method to do this. DO NOT DELETE any local data.

7. Check camera temperature in labview. Once the temperature is above 0 Celsius turn off camera using power on back of camera.
8. Click the button that says 'exit' in red text in the top left corner of labview. It will say exiting and then labview will revert to its editor mode.
9. Now you can close labview using the standard windows close X in the top right corner. You can also close the getting started with labview window that inevitably pops up.
10. Shutdown the computer without installing updates.
11. Ensure all materials (spectralon, standards, etc.) are properly put away.
12. Properly clean any surfaces that came in contact with tissue.
13. Turn off power strip on the back of the cart to shut down ozone cleaner.
14. Cover the camera arm and filters wheel with protective dust cover. See picture below.



A.4. Statistical Analysis

In the published manuscript descriptive statistics and two form of analysis were presented. The descriptive statistics and logistic regression were performed by the University of Arizona Cancer Center Biostatistical Shared Service. Independently I performed discriminant analysis with the quadratic discriminant analysis work appearing the paper. I also analyzed the data using Mahalanobis number and principle component analysis. Since the data had many variables for generally low sample counts per pathological category rigorous analysis was challenging. Revisiting these methods may prove useful if additional data is acquired in the future.

A.4.1. Biostatistics shared service

The shared service expertise is in clinical trials with high sample counts exceeding the number of variables and a well-defined question. Many of the laboratories projects are preliminary sets of data on limited sample numbers with multiple variables. In additional some of the analysis is often exploratory rather than specifically directed. For effective results from the biostatistics shared service it is essential to be able to clearly communicate the variables in the project and the specific statistical question is being asked.

In advanced statistical methods the types of variables used are critical to understand and communicate. For example, age is an ordered numerical variable with meaningful location on a number line relative to other ages. In contrast, favorite ice cream flavor is a categorical variable with no ice cream flavor having an ordered meaning relative to another. Fluorescence images generally have excitation and emission wavelength ranges. In some cases, wavelength has ordinal meaning, but in the case of fluorescence imaging the intensity of a region of interest is related to the complex physical process of fluorescence at the specific excitation and emission wavelengths. Each excitation and emission combination is more appropriately considered a categorical variable like favorite ice cream flavor rather than an ordinal variable like age. Statistics and biomedical imaging are very different fields with different sets if standard vocabulary and concepts. The

biomedical research must both attempt to learn the basic language of statistics and be very careful about how data is labeled in order to prevent errors in analysis. For example, labeling a fluorescence image by its excitation wavelength may be convenient to the researcher, but the name should be changed to a word such as 'Tryptophan Fluorescence' before working with biostatistics in order to avoid variables being improperly defined in the statistical model and causing delays in results.

The final reports provided by Biostatistics is located in the lab storage drive in the folder:

`\Projects\Grants\DoD_Falloposcope\Reports\Papers\MFI_ExVivo\BioStatsAnalysis`

A.4.2. Discriminant Analysis

Discriminant analysis is used to find a combination of features that separate classes of objects. In this case pathology is the class and the mean image intensities are the features. Quadratic discriminant analysis is a more generalized form of linear discriminant analysis in which quadratic classifiers are used to discriminate between objects. With sufficient data a reliable classifier can be created and then new data can simply be tested against the classifier. I used the technique to try to isolate the fewest number of fluorescence images necessary to develop a reliable classifier. While my results were promising, more data are necessary to verify the ideal image type combinations. The technique could potentially be useful for *in vivo* classification of abnormal pixels in ratiometric images once sufficient *in vivo* test data is generated do develop classifiers. Discriminant analysis should be considered for future imaging applications in which multiple variables are being used to discriminate between multiple pathological diagnosis. The MATLAB scripts (Appendix A.4) may be adaptable to future application.

A.5. MATLAB Scripts

MATLAB was used extensively in the project. The raw data from the MFI system had to be preprocessed for quantitative analysis. Once processed the image intensity statistics were recorded using ImageJ and saved in the excel database as discussed early. MATLAB was used to import data from excel and perform further statistical analysis including discriminant analysis, Mahalanobis distance and principle component analysis. As with the data all MATLAB scripts are stored in the projects Parent folder:

`\Projects\Grants\DoD_Fallopiscope\Design_Proximal\MFI_ImageAnalysis`

The image processing scripts were lightly modified from previous MFI tissue studies and their location and use is described. The analysis scripts are generally based on MATLAB tutorials, but heavily modified for the specific application. They are transcribed and described below.

A.5.1. Initial Image Processing

The imaging acquisition sequence does not directly output the 18 image types used for analysis. Before tissue is imaged a series of calibration measurement are acquired including imaging fluorescence standard, a uniform reflector (Spectralon), and illumination power. After calibration measurements tissues are imaged with long pass filters with each image configuration being acquired with the illumination light on and off to measure background noise. The initial image processing normalizes the images using the calibration data and subtracts the background noise. Image subtraction is then used to create effective bandpass emission filters.

This processing had been developed by the Utzinger lab prior to this study and the same scripts were used with minor modifications. While the scripts are included in the Parent folder they require access to the system calibration data and other in house functions only available on the Utzinger lab computers. Thus operation requires permission and access from Dr. Utzinger. On the Utzinger lab computer system each user is restricted from overwriting files of other user so a

copy of the script must be created for each user. Typically, the script of function name is appended with the users initials to indicate who has permissions to use the script.

The first of two processing scripts used is 'runOnceProcessImages_tt.m'. The first four lines of the script are variables the user edits for the specific patient number and imaging date as indicated by the comments. Within this script are calls to a variety MATLAB functions developed by the utzinger lab. In order to run this script copies of each of the called functions will need to be made with the users initials appended and the calls will need to be updated in 'runOnceProcessImages_XX.m' to the updated function names. The called scripts are located in the subfolders of the directory: '\\spxdata\SPXLAB\projects\PROJECT Multispectral Imaging\

The second script is 'runOncePostProcessing_Ovary_tt.m' does the final image creation and saving using the data generated by the first script. The original version (without '_Ovary' appended to the name) creates radiometric images saved with histogram stretching. For this study radiometric images were not used and normalized intensity values were necessary for analysis. Thus the updated version comments out much of the code and saves images as 16-bit floating point tiff files. The function that writes the tiff files is name 'imwrite2tiff' and is available for free on the mathworks file exchange and is also saved in the Parent directory. This script as modified for use in this study does not call on any function only available on the Utzinger computer system. Thus if the data from the first processing step is copied to a local location this script can be run locally by updating the root directory in the script.

Once both processing scripts have been run the images files ready for quantitative analysis will be saved in the 'PostProcTiffNoStretch' folder of the root directory of the second script. If running the script on a local computer care should be taken to ensure that the root directory is either on the lab storage drive or in a folder that automatically synchronizes with the lab storage drive. It is important this data be saved in a secure and recoverable location.

A.5.2. Preparation for statistical analysis

The broad objective of statistical analysis scripts is to perform discriminant analysis, PCA and calculate the Mahalanobis distance in the hopes that these methods create a clear differentiation of cancerous, normal and benign tissue samples given a subset of 18 images types acquired for each tissue sample. In order to perform the analysis a variety of supporting functions are necessary to import and manipulate the data sent to the analysis script and then to plot the results. All of the scripts and functions are reasonably well commented with descriptions of what the variables are and what the code is doing. Again, all of the scripts are in the Parent folder.

The first step in using MATLAB to analyze the data is to load the data in from the excel file. The function copied below, 'importSpecDatabase.m', performs this action. A typical call to this function to load in the relevant data from the excel file is:

```
dataraw = importSpecDatabase('Specimen_database.xlsx',...
    'IntensityAnalysis-Play',3,1772);

function tableout =
importSpecDatabase(workbookFile, sheetName, startRow, endRow)
%IMPORTFILE Import data from a spreadsheet
% DATA = IMPORTFILE(FILE) reads data from the first worksheet in the
% Microsoft Excel spreadsheet file named FILE and returns the data
as a
% table.
%
% DATA = IMPORTFILE(FILE,SHEET) reads from the specified worksheet.
%
% DATA = IMPORTFILE(FILE,SHEET,STARTROW,ENDROW) reads from the
specified
% worksheet for the specified row interval(s). Specify STARTROW and
% ENDROW as a pair of scalars or vectors of matching size for
% dis-contiguous row intervals. To read to the end of the file
specify an
% ENDROW of inf.
%
% Date formatted cells are converted to MATLAB serial date number
format
% (datenum).
%
% Example:
% SpecimendatabaseS5 =
% importSpecDatabase('Specimen_database.xlsx','IntensityAnalysis-
Play',3,1772);
%
% See also XLSREAD.

% Auto-generated by MATLAB on 2014/08/26 12:52:14
```

```

%% Input handling

% If no sheet is specified, read first sheet
if nargin == 1 || isempty(sheetName)
    sheetName = 1;
end

% If row start and end points are not specified, define defaults
if nargin <= 3
    startRow = 3;
    endRow = 1772;
end

%% Import the data, extracting spreadsheet dates in MATLAB serial date
number format (datenum)
[~, ~, row, dateNums] = xlsread(workbookFile, sheetName,
    sprintf('A%d:AB%d', startRow(1), endRow(1)), ' ',
    @convertSpreadsheetDates);
for block=2:length(startRow)
    [~, ~, tmpRawBlock, tmpDateNumBlock] = xlsread(workbookFile,
    sheetName, sprintf('A%d:AB%d', startRow(block), endRow(block)), ' ',
    @convertSpreadsheetDates);
    row = [row; tmpRawBlock]; %#ok<AGROW>
    dateNums = [dateNums; tmpDateNumBlock]; %#ok<AGROW>
end
row(cellfun(@(x) ~isempty(x) && isnumeric(x) && isnan(x), row)) = {' '};
cellVectors = row(:, [1, 6, 7, 8, 9, 10, 11, 12, 13, 14, 15, 22]);
row = row(:, [2, 3, 4, 5, 16, 17, 18, 19, 20, 21, 23, 24, 25, 26, 27, 28]);
dateNums = dateNums(:, [2, 3, 4, 5, 16, 17, 18, 19, 20, 21, 23, 24, 25, 26, 27, 28]);

%% Replace date strings by MATLAB serial date numbers (datenum)
R = ~cellfun(@isequalwithEqualNans, dateNums, row) &
cellfun('isclass', row, 'char'); % Find spreadsheet dates
row(R) = dateNums(R);

%% Create output variable
data = reshape([row{:}], size(row));

%% Create table
tableout = table;

%% Allocate imported array to column variable names
tableout.TissueID = cellVectors(:, 1);
tableout.ImgDate = data(:, 1);
tableout.Patient = data(:, 2);
tableout.Meas = data(:, 3);
tableout.Age = data(:, 4);
tableout.Over50 = cellVectors(:, 2);
tableout.Menopause = cellVectors(:, 3);
tableout.Tissue = cellVectors(:, 4);
tableout.Side = cellVectors(:, 5);
tableout.Technician = cellVectors(:, 6);
tableout.NormalvsAbnormal = cellVectors(:, 7);

```

```

tableout.PathologyPrimary = cellVectors(:,8);
tableout.PathologySecondary = cellVectors(:,9);
tableout.Image = cellVectors(:,10);
tableout.Measurement = cellVectors(:,11);
tableout.AreaWT = data(:,5);
tableout.MeanWT = data(:,6);
tableout.StdDevWT = data(:,7);
tableout.MinWT = data(:,8);
tableout.MaxWT = data(:,9);
tableout.MedianWT = data(:,10);
tableout.Measure = cellVectors(:,12);
tableout.AreaSurf = data(:,11);
tableout.MeanSurf = data(:,12);
tableout.StdDevSurf = data(:,13);
tableout.MinSurf = data(:,14);
tableout.MaxSurf = data(:,15);
tableout.MedianSurf = data(:,16);

```

The full excel table has many more variables and data than is necessary for any given analysis.

MATLAB is ideal for manipulating matrices and vectors. However, the layout of the matrices needs to be logical for the mathematical operations and functions used in the analysis. In the full data set imported from excel there is one row per tissue sample per image type. The columns are the variables for the patient information and the image fluorescence statistics (mean, median, minimum, maximum, etc.). For analysis only one of the fluorescence statistics is used at a time. This allows the data layout to be reshaped such that there is a row for each tissue sample and a column for each image type. The data in the table is then the desired fluorescence statistic for the corresponding tissue sample (row) and image type (column). The following function, 'spectralReshape.m' takes in the output from the previous function and the desired fluorescence measurement statistic and outputs a matrix with reduced dimensionality and reshaped for efficient analysis.

```

function dataout = spectralReshape(datain, meas)

%% Spectral Reshape Description
%takes in data table with separate rows for each image type.
%Using desired measurement (MeanWT, MedianWT, MeanSurf, MedianSurf)
%a new table is made with the component images as individual columns.

datain = sortrows(datain, 'TissueID', 'ascend');
idxr = strfind(datain.Image, 'REFred'); %Find REFred image
measurements'

```



```

idxr = ~cellfun(@isempty,idxr); %Make logical matrix of locations
idxy = strfind(datain.Image, 'REFyellow'); %Find REFyellow image
measurements'
idxy = ~cellfun(@isempty,idxy); %Make logical matrix of locations
idx = (idxr | idxy); %combine locations
DataReduced = datain; %make copy of data to manipulate
DataReduced(idx,:)=[]; %remove rows for REFred and RefYellow
[r,~] = size(DataReduced);

%create index matrix with repeated values 1 through 18
imgtypes = 18; %after REFred and REFyellow removed
idx = (1:r)';
idx = mod(idx,imgtypes);
idx(idx==0)=18;
% DataReduced = sortrows(DataReduced,'TissueID','ascend');

%Created reduced table with only essential patient info
DataInfo = DataReduced(idx==1,1:8);
DataInfo = [DataInfo DataReduced(idx==1, 12)];
TissueIDabbr = DataInfo.TissueID;
TissueIDabbr = char(TissueIDabbr);
TissueIDabbr = TissueIDabbr(:,1:9);
TissueIDabbr = cellstr(TissueIDabbr);
DataInfo = [TissueIDabbr DataInfo(:, 2:end)];
DataInfo.Properties.VariableNames{1} = 'TissueID';

%loop through each img type, extract data into new table, append to
reduced
%table.
for i=1:imgtypes
    imgvec = DataReduced(idx==i,meas);
    imgname = datain.Image{i};
    DataInfo = [DataInfo imgvec];
    DataInfo.Properties.VariableNames{meas} = imgname;
end

dataout = DataInfo;

```

A.5.3. Statistical Analysis

With the data now in the proper form statistical analysis can be performed. MATLAB offers excellent tutorials on the statistical methods and how to implement them. Most of these scripts and functions are adaptations of those tutorials with enhanced functionality relevant to the particular data set.

Discriminant analysis is the primary statistical method used to evaluate the data. The script 'MFI_Discrim.m', copied below is used to perform the analysis. It supports both linear and

quadratic discriminant analysis. The comments in the script guide the user through setting up the desired parameters. The user can define a set of images types and tissue type to run the analysis on. If only two images types are selected the user can also choose to plot the results.

Combinatorics that run the analysis on subsets of the user defined images types are also supported. The user can define the minimum and maximum size of image type subsets to include. Running on all subsets of size 2 to 16 for all image types requires days of runtime on reasonable powerful desktops. If using combinatorics with many subsets it is suggested to do small ranges of subset sizes in chunks and then combine the results to avoid results being lost if the program is interrupted. The end of the script copied below includes a few lines of code that are commented out by default but can be enabled to send the user a text message when the analysis finishes. This requires the user to add the function 'send_text_message' available for free online to MATLAB's path.

```
%% Code to perform Discrim Analysis on MFI data

%% Import data from spreadsheet?

% set import to 1 for yes, 0 for no. Must import the
% first time or after changing measurement type. Set to 0 if just
% rerunning
% analysis with different settings
import = 1;
meastype = 'MeanWT'; % options are 'MeanWT', 'MedianWT', 'MeanSurf',
'MedianSurf'
if import
    clearvars -except meastype
    dataraw =
importSpecDatabase('Specimen_database.xlsx','IntensityAnalysis-
Play',3,1772);
    dataReshape = spectralReshape(dataraw, meastype);
elseif ~import
    clearvars -except dataraw dataReshape meastype
else
    warning('Invalid selection for import');
end

%% Set analysis parameters

% imgtypes options 'fl', 'ref' and 'all' for image types.
Alternatively a
```

```

% vector of specific measurements can be specified of the following:
% {'F280','F320','F320blue','F340','F340uv','F370','F400','F440',...
%
% 'F440red','F480','F480red','F550','R370','R400','R415','R440','R480','
R555'}
imgtypes = {'F320Blue','F370','R400','R415','R480'};
% imgtypes = 'ref';

%tissue options are 'FT' (includes fimbria), 'Fimbria', 'Ovary',
'Uterine'
tissue = 'Ovary';

%which types of DA to run? 1 for run, 0 for do not run
runLDA = 0; %linear
runQDA = 1; %quadratic

%display plots? Only use if not performing combinatorics.
%**** Currently must set two wavelengths manually below.
plotOn = 0; %1 for yes, 0 for no

% run combinatorics? This will choose all subsets of size a to size b
from
% imgtypes to evaluate with the chosen discrim analysis types. If set
to 0
% then a and b can be set to any number.
combOn = 0; %set to 1 to run, 0 to not run
a = 4; %minimum subset size to evaluate. Min allowed is 2
b = 7; %maximum subset size to evaluate. Max allowed is size of
imgtypes

%% Extract specified tissue type and diagnosis
% create data table with proper tissue type and only critical
variables
% Make sure all string inputs have no spaces, 1st letter cap,
remainder
% lower case
tissue = strtrim(tissue);
tissue = [upper(tissue(1)) lower(tissue(2:end))];

%determine location of desired tissue type
tissueloc = strfind(lower(dataReshape.Tissue),lower(tissue));
tissueloc = ~cellfun(@isempty,tissueloc);
data = dataReshape(tissueloc,[1,8:end]);
data = sortrows(data,'PathologyPrimary','ascend');
diagnosis = lower(data.PathologyPrimary);

% gscatter plot example
%I like F440 with F400 or F440red
if plotOn
    xdata = data.F480;
    ydata = data.F440;
    h1 = gscatter(xdata,ydata,diagnosis,'brg','^xo');
end

```

```

%% Extract data for desired imgtypes to analyze

%Cell array (row) of table titles
tabletitles = data.Properties.VariableNames();

%statements to ensure proper imgtypes variable based on earlier
setting
imgtypes = strtrim(imgtypes);
imgtypes = char(imgtypes);
imgtypes = [upper(imgtypes(:,1)) lower(imgtypes(:,2:end))];
imgtypes = cellstr(imgtypes);
if strcmp(imgtypes,'Fl')
    flcol = strfind(tabletitles, 'F');
    flcol = ~cellfun(@isempty,flcol);
    imgtypes = data.Properties.VariableNames(flcol);
elseif strcmp(imgtypes,'Ref')
    refcol = strfind(tabletitles, 'R');
    refcol = ~cellfun(@isempty,refcol);
    imgtypes = data.Properties.VariableNames(refcol);
elseif strcmp(imgtypes,'All')
    flcol = strfind(tabletitles, 'F');
    flcol = ~cellfun(@isempty,flcol);
    refcol = strfind(tabletitles, 'R');
    refcol = ~cellfun(@isempty,refcol);
    allcol = flcol | refcol;
    imgtypes = data.Properties.VariableNames(allcol);
end

%% discrim analysis

% performs DA with specified parameters. Can do LDA and/or QDA. Also
setup
% to take combinatorial subsets of imgtypes and perform DA on each
subset.
% Results are saved in structures called LDA and QDA respectively. The
% structures are also converted to tables, LDATable and QDATable for
easier
% visualization of the data

    %length of imgtypes used for factorials below
    s = length(imgtypes);

    if combOn
        % init r as number of rows in cell array
        r = 0;
        %calc total number of combinations
        for j = a:b
            r = r + factorial(s)/(factorial(j)*factorial(s-j));
        end

        %initialize mat to hold all combinations of images types
        imgtypemat = cell(r,b);
        %loop to populate imgtypemat

```

```

        rowcounter = 1;
        for j = a:b
            % creates row of each possible set of j sized combinations
            subsets = combnk(imgtypes,j);
            [r_sub,c_sub] = size(subsets);
            imgtypemat(rowcounter:rowcounter+r_sub-1,1:c_sub) =
subsets;
            rowcounter = rowcounter + r_sub;
        end
    elseif ~combOn
        imgtypemat = imgtypes';
        b = s;
        r = 1;
    else
        warning('invalid choice for combOn');
    end

    %Setup initial variables that do not change with num imgtypes
    % number of cancer samples
    Nbenign = sum(strcmp('benign',diagnosis));
    % number of benign samples
    Ncancer = sum(strcmp('cancer',diagnosis));
    % number normal samples
    Nnormal = sum(strcmp('normal',diagnosis));
    % vector containing above numbers. Sorted alphabetically so match
data
    Nclass = [Nbenign Ncancer Nnormal];
    % number of total observations
    N = sum(Nclass);
    % total number of diagnosis types
    K = length(Nclass);

    % initialize variables to save in structure\
    % LDA variables
    if runLDA
        LDA.imgtypes = cell(r,1);
        LDA.imgtypesnum = zeros(r,1);
        LDA.resuberror = zeros(r,1);
        LDA.totalmisclass = zeros(r,1);
        LDA.cverror = zeros(r,1);
        LDA.confusionmat = cell(r,1);
        LDA.classnames = cell(r,1);
        LDA.pval_Mardia = zeros(r,1);
    end
    % QDA variables
    if runQDA
        QDA.imgtypes = cell(r,1);
        QDA.imgtypesnum = zeros(r,1);
        QDA.resuberror = zeros(r,1);
        QDA.totalmisclass = zeros(r,1);
        QDA.cverror = zeros(r,1);
        QDA.confusionmat = cell(r,1);
        QDA.classnames = cell(r,1);
        QDA.pval_Mardia = zeros(r,1);
    end
end

```

```

% if running LDA and QDA can calc Bartlett pval
if runLDA && runQDA
    LDA.pval_Bartlett = zeros(r,1);
    QDA.pval_Bartlett = zeros(r,1);
end

%loop over all rows of imgtypesmat
for j = 1:r
    imgtypesJ = imgtypemat(j,:);
    imgtypesJ = imgtypesJ(~cellfun('isempty',imgtypesJ));

    %setup variables that do change with imgtypes
    % create array of data with desired imgtypes
    X = data(:,imgtypesJ);
    % D = number of imgtypesJ used
    D = length(X(1,:));
    if runLDA
        LDA.imgtypes(j) = {imgtypesJ};
        LDA.imgtypesnum(j) = D;
    end
    if runQDA
        QDA.imgtypes(j) = {imgtypesJ};
        QDA.imgtypesnum(j) = D;
    end
end

%run LDA with validation checks
if runLDA
    % LDA - seems to work without using pseudoLinear
    L = fitcdiscr(X,diagnosis,'PredictorNames',imgtypesJ);

    %Calculate resubstitution error
    LDA.classnames(j) = {L.ClassNames'};
    LDA.resuberror(j) = resubLoss(L);
    LDA.totalmisclass(j) =
LDA.resuberror(j)*L.NumObservations;
    LDA.confusionmat(j) = {confusionmat(L.Y,resubPredict(L))};

    %cross validation
    cvmodelL = crossval(L,'kfold',5);
    LDA.cverror(j) = kfoldLoss(cvmodelL); % want this to be as
low as qerror

    %linear Q-Q plot and Mardia Kurtosis Test
    %setup variables
    mahL = mahal(L,L.X,'ClassLabels',L.Y);
    [mahL,sorted] = sort(mahL); % sorted obberved quantiles

    %calc Mardia Kurtosis - want pval high
    obsKurt = mean(mahL.^2);
    expKurt = D*(D+2);
    varKurt = 8*D*(D+2)/N;
    [~,LDA.pval_Mardia(j)] =
ztest(obsKurt,expKurt,sqrt(varKurt));

```

```

%plot Q-Q plot
if plotOn
    expQ = chi2inv((1:N)-0.5)/N,D); % expected quantiles
    figure(20);
    gscatter(expQ,mahL,L.Y(sorted),'bgr',[[],[],'off']);
    legend('normal','benign','cancer','Location','NW');
    xlabel('Expected quantile');
    ylabel('Observed quantile');
    title('Q-Q plot for LDA');
    line([0 20],[0 20],'color','k');
end

% can regularize (shrink number of predictors for linear
discrim, but
% not quadratic. Can implement later to see results if
time allows.

end

% run QDA with validation checks
if runQDA
    % QDA - needs pseudo - not sure how this alters following
validation tests
    Q =
fitcdiscr(X,diagnosis,'PredictorNames',imgtypesJ,'DiscrimType','pseudo
Quadratic');

    %Calculate resubstitution error
    QDA.classnames(j) = {Q.ClassNames};
    QDA.resuberror(j) = resubLoss(Q);
    QDA.totalmisclass(j) =
QDA.resuberror(j)*Q.NumObservations;
    QDA.confusionmat(j) = {confusionmat(Q.Y,resubPredict(Q))};

    %quadratic
    cvmodelQ = crossval(Q,'leaveout','on');
    QDA.cverror(j) = kfoldLoss(cvmodelQ); % want this to be as
low as qerror

    %quadratic Q-Q plot and Mardia Kurtosis Test
    %setup variables
    mahQ = mahal(Q,Q.X,'ClassLabels',Q.Y);
    expQ = chi2inv((1:N)-0.5)/N,D);
    [mahQ,sorted] = sort(mahQ);

    % Mardia Kurtosis Test - want high pval
    obsKurt = mean(mahQ.^2);
    expKurt = D*(D+2);
    varKurt = 8*D*(D+2)/N;
    [~,QDA.pval_Mardia(j)] =
ztest(obsKurt,expKurt,sqrt(varKurt));

    %Quadratic Q-Q plot

```

```

        if plotOn
            figure(21);
            gscatter(expQ,mahQ,Q.Y(sorted),'grb',[ ],[ ],'off');
            legend('normal','cancer','benign','Location','NW');
            xlabel('Expected quantile');
            ylabel('Observed quantile for QDA');
            title('Q-Q plot for QDA');
            line([0 20],[0 20],'color','k');
        end
    end

    if runQDA && runLDA
        % Bartlett Test of Equal Covariance Matrices for Linear
        Discriminant Analysis
        % check if linear or quad discrim analysis is appropriate
        if pval is less
            % than .05 then use quad, else use linear.
            Q =
            fitcdiscr(X,diagnosis,'PredictorNames',imgtypesJ,'DiscrimType','pseudo
            Quadratic');
            SigmaQ = Q.Sigma;
            SigmaL = L.Sigma;
            logV = (N-K)*log(det(SigmaL));
            for k=1:K
                logV = logV - (Nclass(k)-1)*log(det(SigmaQ(:,:,k)));
            end
            nu = (K-1)*D*(D+1)/2;
            %had to add a real to logV. Not sure if this is indicative
            of an issue in
            %the above lines of code or something missed in the MATLAB
            example.
            LDA.pval_Bartlett(j) = 1 - chi2cdf(real(logV),nu);
            QDA.pval_Bartlett(j) = LDA.pval_Bartlett(j);
        end

    end

    % convert save structure to tables for easier analysis.
    if runLDA
        LDATable = struct2table(LDA);
    end
    if runQDA
        QDATable = struct2table(QDA);
    end

    %
    % savstring = ['QDASubset_LeaveOneOut_' num2str(a) '-' num2str(b)];
    % save(savstring,'QDA','QDATable');
    % send_text_message('#####','att','MFI_Discrim
    Finished',savstring);

```

Principle component analysis was not used in the published results, but was also considered.

The analysis is performed in the script 'MFI_PCA.m' below. The script comments guide the user

through setting various parameters of interest such as images types, tissue type and what pathologies to consider. The script calls a supporting function, 'PCAdata.m', that takes in the user defined parameters and returns the data vectors in the proper form to run the PCA analysis. The function is also copied below.

```
%% Code to perform PCA on MFI data

%%
%%Set desired tissue subset and settings for analysis

%Tissue subset

range = 'fl'; %Options are 'fl' for fluorescence, 'ref' for
reflectance
            % and 'all' for all image types
tissue = 'ovary'; %Options are 'FT' (includes fimbria), 'Fimbria',
'Ovary', 'Uterine'
diagnosis = 'normal'; %options are 'normal', 'benign', 'cancer' or
'all'
colorby = 'diagnosis'; %Datapoints will be color coded accorindg to:
'diagnosis'

%Choose type of PCA. 1 for variance based, 2 for raw data
type = 1;

%Need to load data from spreadsheet? 1 for yes, 0 for no. Must load
the
%first time or after changing measurement type. Set to 0 if just
rerunning
%analysis with different tissue or PCA settings
load = 0;
meastype = 'MeanSurf'; % options are 'MeanWT', 'MedianWT', 'MeanSurf',
'MedianSurf'
if load
    dataraw =
importSpecDatabase('Specimen_database.xlsx','IntensityAnalysis-
Play',3,1772);
    dataReshape = spectralReshape(dataraw, meastype);
end

%This line creates proper variables for analysis based on above
settings.
[imgType, tissueID, intensities, colorvec] = PCAdata(dataReshape,
range, tissue, diagnosis, colorby);

%%
% create boxplot of data
figure(11)
boxplot(intensities,'orientation','horizontal','labels',imgType);
```

```

%%
%Run PCA command and create orthonormal coeff

%PCA with variable weights based on variance
if type == 1;

    [coeff,score,latent,tsquared,explained]=pca(intensities,'VariableWeights','variance');
elseif type ==2;
    [coeff,score,latent,tsquared,explained]=pca(intensities);
else
    warning('Invalid Entry for PCA calculation', '1 for variance normalizaion, 2 for raw comparison');
end
%PCA without variable weights
% [coeff,score,latent,tsquared,explained]=pca(intensities);

%orthonormalize coefficients
coefforth = diag(std(intensities))\coeff;

%%
% plot component scores

figure(21)
plot(score(:,1),score(:,2),'+');
xlabel('1st Principle Component');
ylabel('2nd Principle Component');

%%
% create scree plot
figure(31)
pareto(explained);
xlabel('Principle Component');
ylabel('Variance Explained (%)');

%%
%Find most extreme tissue samples
n = 0; %number of outliers to list
[st2,index] = sort(tsquared, 'descend');
extreme = index(1:n);
tissueID(extreme,:)

%%
% Visualize Results with biplot
% Data points should be colored as specified by user
figure(41)
hbi = biplot(coefforth(:,1:2),...
    'scores',score(:,1:2),...
    'varlabels',imgType,...
    'ObsLabels',colorvec,...
    'LineWidth',2);
title('Bi-Plot');
xlabel('PCA1');
ylabel('PCA2');

```

```

for ii = 1:length(hbi)-length(colorvec)
    set(hbi(ii), 'Color', 'k')
end
for ii = length(hbi)-length(colorvec):length(hbi)
    userdata = get(hbi(ii), 'UserData');
    if ~isempty(userdata)
        set(hbi(ii), 'Color', colorvec{userdata}, 'MarkerSize', 17);
    else
        set(hbi(ii), 'Color', 'k');
    end
end
end

```

‘PCAdatam’

```

function [imgType, tissueID, intensities, colorvec] = PCAdatam(datain,
range, tissue, diagnosis, colorby)

%% PCAdatam input descriptions
%datain is spectrally reshaped data table
%range is 'fl' fluorescence data, 'ref' reflectance data, or 'all' data
%Tissue specifies type of tissue to consider.
% Options: 'FT' (includes fimbria), 'Fimbria', 'Ovary', 'Uterine'
%Diagnosis limits tissue to 'normal' 'benign' 'cancer' or 'all'
%colorby specifies what feature to color code data by.
% Options: 'Menopause', 'Age', 'Diagnosis', 'Tissue'
%average by same feature as determined by colorby. 1 for yes, 0 for no

%% Construct necessary variables.

%Cell array (row) of table titles
tabletitles = datain.Properties.VariableNames();

%size of input table
[r, c] = size(datain);

%Make sure all string inputs have no spaces, 1st letter cap, remainder
%lower case
tissue = strtrim(tissue);
tissue = [upper(tissue(1)) lower(tissue(2:end))];
range = strtrim(range);
range = [upper(range(1)) lower(range(2:end))];
diagnosis = strtrim(lower(diagnosis));
colorby = strtrim(lower(colorby));

%location of fluorescence and reflectance data columns
if strcmp(range, 'Fl')
    flcol = strfind(tabletitles, 'F');
    flcol = ~cellfun(@isempty, flcol);
    imgType = datain.Properties.VariableNames(flcol);
elseif strcmp(range, 'Ref')

```

```

        refcol = strfind(tabletitles, 'R');
        refcol = ~cellfun(@isempty,refcol);
        imgType = datain.Properties.VariableNames(refcol);
elseif strcmp(range,'All')
    flcol = strfind(tabletitles, 'F');
    flcol = ~cellfun(@isempty,flcol);
    refcol = strfind(tabletitles, 'R');
    refcol = ~cellfun(@isempty,refcol);
    allcol = flcol | refcol;
    imgType = datain.Properties.VariableNames(allcol);
else
    warning('Invalid Range', 'Invalid tissue range. Input "Fl", "Ref",
or "All"');
    return
end

%determine location of desired tissue type
tissueloc = strfind(lower(datain.Tissue),lower(tissue));
tissueloc = ~cellfun(@isempty,tissueloc);

%%
%detemine location of different diagnosis
%Diagnosis limits tissue to 'normal' 'benign' 'cancer' or 'all'
%Initialize vectors to false logicals. This helps prevent errors later
when
%comparing locations as all vectors are logicals after locations are
%determined.
[cancerloc, normalloc, benignloc, otherloc] = deal(false(r,1));
if strcmp(diagnosis,'cancer') || strcmp(diagnosis,'all');
    cancerloc = strfind(lower(datain.PathologyPrimary),'cancer');
    cancerloc = ~cellfun(@isempty,cancerloc);
end
if strcmp(diagnosis,'normal') || strcmp(diagnosis,'all');
    normalloc = strfind(lower(datain.PathologyPrimary),'normal');
    normalloc = ~cellfun(@isempty,normalloc);
end
if strcmp(diagnosis,'benign') || strcmp(diagnosis,'all');
    benignloc = strfind(lower(datain.PathologyPrimary),'benign');
    benignloc = ~cellfun(@isempty,benignloc);
end
if strcmp(diagnosis,'other') || strcmp(diagnosis,'all');
    otherloc = ~(cancerloc | normalloc | benignloc);
end

%Determine location of desired diagnosis (unused loc vectors are all
false
%by default)
diagloc = cancerloc | normalloc | benignloc | otherloc;

%create tissueID vector from appropriate tissue and diagnosis
locations
tissueID = char(datain.TissueID(tissueloc & diagloc));

%create 2D array with appropriate intensity values from the table

```

```

intensities = datain(tissueloc & diagloc,imgType);
intensities = table2array(intensities);

%%
%colorby specifies what feature to color code data by.
% Options: 'Menopause', 'Age', 'Diagnosis', 'Tissue'
% *****only 'diagnosis' has been implemented thus far.

%if colorby is diagnosis return a vector with color codes with green
for
%normal, red for cancer and black for benign
if strcmp(colorby,'diagnosis')
    colorvec = cell(r,1);
    colorvec(normalloc) = {'g'};
    colorvec(benignloc) = {'b'};
    colorvec(cancerloc) = {'r'};
    colorvec(~(normalloc | benignloc | cancerloc)) = cellstr('k');
else
    warning('not programmed option...yet')
end

colorvec = colorvec(tissueloc & diagloc);
% %determine location of menopause status
% premenloc = strfind(datain.Menopause,'pre');
% premenloc = ~cellfun(@isempty,premenloc);
% postmenloc = strfind(datain.Menopause,'post');
% postmenloc = ~cellfun(@isempty,postmenloc);
% perimenloc = strfind(datain.PathologyPrimary,'peri');
% perimenloc = ~cellfun(@isempty,perimenloc);
% othermenloc = ~(premenloc | postmenloc | perimenloc);

end

```

The final type of analysis performed on the data was the calculation of Mahalanobis distance.

Again the results were not included in the published manuscript, but may be worth revisiting if more samples are acquired in the future. The MATLAB scripts are very similar in style to the PCA analysis scripts. The script 'MFI_Mahal.m' is the primary script running the analysis with user defined variables at the beginning. This is supported by the function 'Mahaldata.m' that takes in the user defined parameters and outputs the data in the proper form to carry out the analysis. Both files are copied below.

```

%% Code to perform Mahalanobis Distance on MFI data

%%
%Set desired tissue subset and settings for analysis

```

```

%Tissue subset

range = 'fl'; %Options are 'fl', 'ref' and 'all' for image types
tissue = 'Ovary'; %Options are 'FT' (includes fimbria), 'Fimbria',
'Ovary', 'Uterine'
centerto = 'normal'; %options are 'normal', 'benign', 'cancer' or
'all'

%Need to load data from spreadsheet? 1 for yes, 0 for no. Must load
the
%first time or after changing measurement type. Set to 0 if just
rerunning
%analysis with different tissue or PCA settings
load = 0;
meastype = 'MeanWT'; % options are 'MeanWT', 'MedianWT', 'MeanSurf',
'MedianSurf'
if load
    dataraw = importSpecDatabase('Specimen_database.xlsx',...
    'IntensityAnalysis-Play',3,1772);
    dataReshape = spectralReshape(dataraw, meastype);
end

%This line creates proper variables for analysis based on above
settings.
[tissueID, intensities, diagnosis, refsampl] = Mahaldata(dataReshape,
range, tissue, centerto);

a = 1;
b = 12;
M = mahal(intensities(:,a:b),refsampl(:,a:b));
x = 1:length(M);
nc = sum(strcmp('c',diagnosis));
nn = sum(strcmp('n',diagnosis));
nb = sum(strcmp('b',diagnosis));

figure(10)
scatter(x(1:nc),M(1:nc),'r')
hold on
scatter(x(nc+1:nn+nc),M(nc+1:nn+nc),'g');
scatter(x(nc+nn+1:nn+nc+nb),M(nc+nn+1:nn+nc+nb),'k');
hold off

```

‘Mahaldata.m’

```

function [tissueID, intensities, diagnosis, refsampl] =
Mahaldata(datain, range, tissue, centerto)

%% Mahaldata input descriptions
% Mahaldata outputs three matrices. One of normal, one of cancer and
one of
% benign samples and the chosen measurements
%
```

```

% datain is spectrally reshaped data table
% range is 'fl' fluorescence data, 'ref' reflectance data, or 'all'
data
% Tissue specifies type of tissue to consider.
% Options: 'FT' (includes fimbria), 'Fimbria', 'Ovary', 'Uterine'
% Diagnosis limits tissue to 'normal' 'benign' 'cancer' or 'all'
% colorby specifies what feature to color code data by.
% Options: 'Menopause', 'Age', 'Diagnosis', 'Tissue'
% (not implemented) average by same feature as determined by colorby.
% 1 for yes, 0 for no

%% Construct necessary variables.

%Cell array (row) of table titles
tabletitles = datain.Properties.VariableNames();

%size of input table
[r, ~] = size(datain);

%Make sure all string inputs have no spaces, 1st letter cap, remainder
%lower case
tissue = strtrim(tissue);
tissue = [upper(tissue(1)) lower(tissue(2:end))];
range = strtrim(range);
range = [upper(range(1)) lower(range(2:end))];
centerto = strtrim(lower(centerto));

%location of fluorescence and reflectance data columns
if strcmp(range,'Fl')
    flcol = strfind(tabletitles, 'F');
    flcol = ~cellfun(@isempty,flcol);
    imgType = datain.Properties.VariableNames(flcol);
elseif strcmp(range,'Ref')
    refcol = strfind(tabletitles, 'R');
    refcol = ~cellfun(@isempty,refcol);
    imgType = datain.Properties.VariableNames(refcol);
elseif strcmp(range,'All')
    flcol = strfind(tabletitles, 'F');
    flcol = ~cellfun(@isempty,flcol);
    refcol = strfind(tabletitles, 'R');
    refcol = ~cellfun(@isempty,refcol);
    allcol = flcol | refcol;
    imgType = datain.Properties.VariableNames(allcol);
else
    warning('Invalid tissue range. Input "Fl", "Ref", or "All"');
    return
end

%determine location of desired tissue type
tissueloc = strfind(lower(datain.Tissue),lower(tissue));
tissueloc = ~cellfun(@isempty,tissueloc);

%%
%determine location of different diagnosis

```

```

%centerto columnm centers data specified diagnosis type: 'normal'
'benign' 'cancer' or 'all'
%Initialize vectors to false logicals. This helps prevent errors later
when
%comparing locations as all vectors are logicals after locations are
%determined.
[cancerloc, normalloc, benignloc, otherloc] = deal(false(r,1));

cancerloc = strfind(lower(datain.PathologyPrimary), 'cancer');
cancerloc = ~cellfun(@isempty, cancerloc);
cancertab = datain(tissueloc & cancerloc, imgType);
cancerintensities = table2array(cancertab);
[nc, ~] = size(cancerintensities);
muc = mean(cancerintensities);

cancerTissueID = char(datain.TissueID(tissueloc & cancerloc));

normalloc = strfind(lower(datain.PathologyPrimary), 'normal');
normalloc = ~cellfun(@isempty, normalloc);
normaltab = datain(tissueloc & normalloc, imgType);
normalintensities = table2array(normaltab);
normalTissueID = char(datain.TissueID(tissueloc & normalloc));
[nn, ~] = size(normalintensities);
mun = mean(normalintensities);

benignloc = strfind(lower(datain.PathologyPrimary), 'benign');
benignloc = ~cellfun(@isempty, benignloc);
benigntab = datain(tissueloc & benignloc, imgType);
benignintensities = table2array(benigntab);
benignTissueID = char(datain.TissueID(tissueloc & benignloc));
[nb, ~] = size(benignintensities);
mub = mean(benignintensities);

intensities = [cancerintensities; normalintensities;
benignintensities];

%calc columnm means as determined by centerto
n = nc+nn+nb;
if strcmp(centerto, 'cancer')
    mu = muc;
    refsampl = cancerintensities;
elseif strcmp(centerto, 'normal')
    mu = mun;
    refsampl = normalintensities;
elseif strcmp(centerto, 'benign')
    mu = mub;
    refsampl = benignintensities;
elseif strcmp(centerto, 'all')
    mu = (nc*muc+nn*mun+nb*mub)/(n);
    refsampl = intensities;
else
    warning('invalid choice for centerto')
end

```



```
%calc final column centered intensity matrix

intensities = intensities - repmat(mu,n,1);

%center refsampl
[r,~] = size(refsample);
refsample = refsample - repmat(mu,r,1);

%final tissue ID vector
tissueID = [cancerTissueID;normalTissueID;benignTissueID];

%initialize and populate diagnosis vector
diagnosis = cell(n,1);
diagnosis(1:nc) = {'c'};
diagnosis(nc+1:nc+nn) = {'n'};
diagnosis(nc+nn+1:n) = {'b'};

end
```

APPENDIX B: FALLOPOSCOPE

This appendix contains all supporting material for the falloposcope project. This includes the submitted manuscript and copies or locations of electronic files including standard operating procedures, lens prescriptions and MATLAB scripts.

B.1. Submitted Manuscript

The following manuscript has been submitted to the Journal of Biomedical Optics.

Ultra miniature optical design for multispectral fluorescence imaging endoscopes

Tyler H. Tate^{*a}, Molly Keenan^b, John Black^c, Urs Utzinger^{a,b}, Jennifer K. Barton^{a,b}

^aCollege of Optical Sciences, University of Arizona, 1630 E University Blvd, Tucson, AZ 85721

^bBiomedical Engineering, University of Arizona 1657 E Helen Street, Tucson, AZ 85721

^cGlannaventa Inc., 2276 Allegheny Way, San Mateo, CA, 94402, USA

Abstract: A miniature wide-field multispectral endoscopic imaging system was developed enabling reflectance and fluorescence imaging over a broad wavelength range. At 0.8 mm diameter, the endoscope can be utilized for natural orifice imaging in small lumens such as the fallopian tubes. Five lasers from 250 to 642 nm are coupled into a 125 μm diameter multimode fiber and transmitted to the endoscope distal tip for illumination. Ultraviolet and blue wavelengths excite endogenous fluorophores which can provide differential fluorescence emission images for health and disease. Visible wavelengths provide reflectance images which can be combined for pseudo white-light imaging and navigation. Imaging is performed by a 300 μm diameter three-element lens system connected to a 3000 element fiber. The lens system was designed for 70° full field of view, working distance from 3 mm to infinity, and 40% contrast at the Nyquist cutoff of the fiber bundle. Measured performance characteristics are near design goals. The endoscope was utilized to obtain example monochromatic, pseudo white-light, and composite fluorescence images of phantoms and porcine reproductive tract. This work shows the feasibility of packaging a highly capable multispectral fluorescence imaging system into a miniature endoscopic system which may have applications in early detection of cancer.

Keywords: Multispectral Imaging, Fluorescence, Lens Design, Endoscope, Cancer, ObGyn

*First Author, E-mail: TylerTate@email.arizona.edu

Grant Funding:

Department of Defense (W81XWH-13-1-0131); The National Institutes of Health/ National Institute of Biomedical Imaging and Bioengineering (U54EB015403); Arizona Technology Research Innovation Fund Imaging Fellowship

1. Introduction

Early detection and diagnosis of some diseases is limited by the ability to obtain high resolution images in deeply buried organs. An example is ovarian cancer, the deadliest female reproductive malignancy¹. Ovarian cancer typically presents with non-specific symptoms and current screening methods (physical examination, transvaginal ultrasound, the CA-125 blood test) have not proven to be reliable or effective when used for annual screening in the general population in large clinical trials²⁻⁴. Detection at a stage early enough to make a significant difference in outcome is problematic both because of the lack of obvious symptoms and the peculiar natural history of the most lethal phenotype of the disease – High Grade Serous Ovarian Cancer (HGSOC)^{123,124}. The model suggests that HGSOC exists in an occult asymptomatic form for 3 – 4 years where it is too small to be detected by a secreted biomarker, MRI, CT and probably ultrasound, followed by a rapid growth phase in years 4 – 5 with concomitant presentation of symptoms, at which time the tumor is already metastatic and lethal^{103,104}.

Emerging consensus suggests that a significant fraction, perhaps over 50%, of HGSOC actually originates in the fallopian tube with subsequent migration to the ovary and peritoneum^{10,16}. If this hypothesis is correct it opens a window on early detection of the disease through minimally invasive endoscopy using relatively inexpensive but robust optical components. Optical imaging enables localization of disease and could confirm diagnosis from a suspicious blood marker before invasive surgical procedures are required. High resolution optical techniques potentially have the capability to yield both structural and functional information at the resolution level necessary for early detection but free space optics cannot penetrate trans-dermally through the body to sufficient depth. Fiber

optics and miniaturization of free-space components allow integration into minimally invasive endoscopes.

The body provides a natural pathway via the vagina, cervix and uterus to access the fallopian tubes and ovaries. The proximal tubal opening of the fallopian tube is located in the uterus with an ostium diameter of approximately 1 mm²⁵. The tube then expands to a maximum intratubal diameter of approximately 1 cm throughout a 12-15 cm tortuous path to the fimbriae where the tube is attached to the ovary²⁵. Simple white-light imaging endoscopes called falloposcopes with outer diameters (OD) less than a millimeter have been used previously to image the fallopian tube *in-vivo* for fertility-impeding blockages^{125–128}. These falloposcopes were introduced through the working channel of a hysteroscope. Imaging was performed by a lens attached to a coherent fiber bundle (CFB). Falloposcopes designed for tubal imaging of fertility blockages lack sufficient imaging performance to screen for subtle changes presented by early-stage ovarian cancer.

The navigational portion of a screening falloposcope should be forward-viewing with a wide-field of view and in a flexible package of at most 800- μ m OD. Forward-viewing, wide-field endoscopes have three primary technologies to relay images from the distal tip to the computer: fiber bundles, miniature detectors, and optical scanning. Many modern endoscopes now use miniature CMOS detectors directly in the endoscope tip. Miniature detectors with 0.5 mm x 0.5 mm dimensions have been demonstrated and 1 mm x 1 mm detectors are commercially available¹²⁹. As the technology continues to shrink it may be viable for an 800- μ m OD endoscope, but is not currently an option. Scanning techniques such as piezo scanning fiber endoscopes have also continued to shrink⁸¹. A 1.2 mm implementation has been used to image 1 cm of the distal fallopian tube *in-vivo*¹³⁰. The

technique provides significant optical advantages and high effective pixel density, but requires additional miniaturization to be inserted further into the fallopian tube. The most traditional forward-viewing endoscopic imaging technique uses a CFB. A lens in the endoscope tip images onto the distal face of the CFB and a separate imaging system outside of the body then images the proximal face of the CFB onto a detector. For endoscopes with sub-millimeter diameters, the CFB approach remains the most viable technology but as with any camera system there is a trade-off between field of view and resolution. The limited size of the falloposcope restricts the number of CFB pixels compromising the ability to perform simultaneous wide-field navigation with near cellular resolution. However, fluorescence imaging can enable detection of early disease through tissue functional changes.

Fluorescence imaging can be used to visualize changes in chemical make-up of tissue and is well suited to wide-field imaging. In particular, endogenous fluorophores (tryptophan, collagen, nicotinamide adenine dinucleotide + hydrogen, etc.) can have different concentrations in normal and abnormal tissue. Using UV and short-wave visible excitation sources, different fluorophores can be excited in the tissue. Endogenous fluorescence differences between normal, benign and cancerous ovarian tissue have been characterized both *in-vivo* and *ex-vivo* by the investigators and others using fiber optic probes^{27,39,41,131} and wide-field autofluorescence imaging^{40,106,132}. MFI can image in both reflectance and fluorescence mode to either measure optical absorption or fluorescence emission, both of which can be an indicator of molecular changes (changes in concentration of hemoglobin or fluorophores) or to combine multiple reflectance images for pseudo white-light imaging. Miniaturizing the wide-field MFI system for endoscopic use is the

next step to validate use of this technique *in-vivo* in deeply buried organs. In this paper we describe the optical design and characterization of a miniaturized MFI system and its integration into an 800- μm OD falloposcope prototype.

2. Design and Methods

2.1. Optical Design

The MFI optical design is comprised of four optical subsystems with independent and interrelated specifications (Fig. 1). Following the path of the light the four optical subsystems are: proximal illumination, distal illumination, distal imaging, and proximal imaging. For effective navigation the overall system specification for full field of view (FFOV) is 70-degrees. Based on previous studies the included illumination wavelengths are 250, 375, 406, 515, and 642 nm^{27,39–41,106,131,132}. The ultraviolet and blue wavelengths efficiently excite the endogenous fluorophores. Sampling the blood absorption curve in reflectance mode with 375, 406 and 515 nm can also provide diagnostic utility¹³². Finally, pseudo white-light imaging can be obtained by acquiring and combining a sequence of images with the 406, 515 and 642 nm illumination wavelengths. The broad spectral range including 250 nm light and the requirement to perform both reflectance and fluorescence imaging requires separate excitation and illumination channels. The imaging channel is optimized for imaging from 375 nm to 642 nm. Thus 250 nm illumination is only used for fluorescence mode, but all other illumination wavelengths can be used in either reflectance or fluorescence mode. In order to accommodate integration into a flexible endoscope with OD of at most 800 microns, the illumination and imaging channels are limited to 125 and 300 μm diameters respectively. The remaining space is necessary for the ferrule, pull-wires

and protective sheath¹³³. However, the design does allow a second 125- μm diameter lumen for additional future functionality without exceeding total OD requirements.

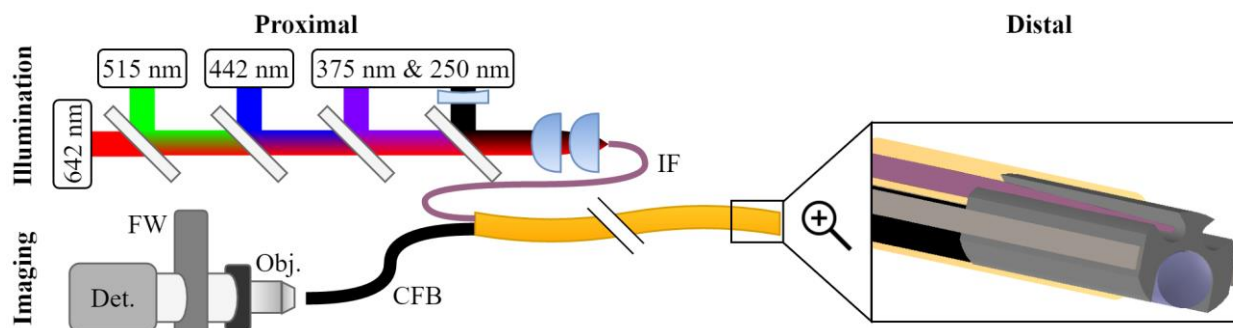


Figure 1. Endoscopic MFI system overview. The proximal illumination system combining five laser beams into the illumination fiber (IF) is shown top left. The proximal illumination system imaging the proximal face of the CFB through the microscope objective (Obj.), filter wheel (FW) and onto the detector (Det.) is shown bottom left. On the right is a zoomed in model of the distal tip showing the tapered illumination fiber on top and the imaging lens with CFB bottom.

2.2. Proximal Illumination

Proximally, the five laser beams are collimated, co-aligned, and focused into the illumination fiber. The two ultraviolet wavelengths are produced by a pulsed, frequency doubled and tripled alexandrite laser described previously¹³⁴. The 406 nm, 515 nm, and 642 nm wavelengths are provided by SM pigtailed diode lasers (Models: LP406-SF20, LP520-SF15 and LP642-SF20, Thorlabs, Newton, New Jersey) each with a temperature-controlled diode driver (CLD1010LP, Thorlabs). Each of the visible lasers is collimated by an adjustable focus collimator (CFC-11X-A, Thorlabs). The beams are combined using a series of four dichroic mirrors (Models: ZT594RDC, ZT488RDC, ZT375RDC, Chroma Technology Corp, Bellows Falls, Vermont, and model FF310-DiO1, Semrock Inc., Rochester, New York). The 642 nm laser is the reference beam and passes through all

dichroics. Each subsequent shorter wavelength is coaligned with the red beam using a dichroic that transmits the longer wavelength(s) and reflects the shorter wavelength such that after the fourth dichroic all five laser beams are coaligned.

The coaligned beam path is then focused into the illumination fiber. Based on the diameter and high UV to Vis transmission requirements, the illumination fiber used was a high-OH silica core fiber (FIP100110125, Polymicro, Phoenix, AZ) with 0.22 numerical aperture (NA), a 100 μm core and OD of 125 μm . The primary coupling lenses are a pair of uncoated plano-convex 20 mm focal length calcium fluoride lenses (LA5315, Thorlabs). Using a pair of lenses rather than a single lens provides two major advantages at the cost of one disadvantage. The split lenses significantly reduce spherical aberration, necessary to focus the lasers into the 100 μm core fiber. Additionally, the 4 to 4.5 mm diameter laser beams require an effective focal length of approximately 10 mm to match the 0.22 NA fiber. The effective focal length of the lens pair is 9.8 mm and the 20 mm focal length lenses are readily available off-the-shelf while an equivalent single lens is not. However, due to the wide spectral range the lenses are uncoated and using a pair of lenses increases losses from Fresnel reflections. Despite calcium fluoride being low dispersion, the lenses require longitudinal chromatic aberration correction. The focus location of the 375 nm beam is used as the reference focal distance. The adjustable focus collimators on the visible beams are effectively used as weak positive lenses to independently match each visible beam focus to the 375 nm beam focus. The 250 nm beam is chromatically corrected by placing a negative 200 mm UV anti-reflection coated fused silica lens (48-325, Edmund Optics, Barrington, New Jersey) in the beam path just prior to dichroic mirror. Assuming 4.5 mm beam diameters the design theoretically focuses all five beams to the same location

with root mean square radii between 5.5 μm and 15.5 μm and matching the illumination fiber. The 100- μm core, .22 NA fiber is placed just beyond focus to couple in the light without damaging the fiber face.

2.3. *Distal Illumination*

The distal illumination must fully illuminate the FFOV imaged by the distal imaging objective. Multimode fibers with the necessary spectral transmission range and outer diameter are not available with sufficient NA to illuminate a 70-degree FFOV. Thus the illumination fiber distal output illumination angle requires modification. The illumination fiber is not coaxial with the imaging optics axis so the illumination angle must be slightly larger than the 70-degree imaging field. Thus the desired output NA is at least 0.6, corresponding to a 73.7-degree illuminated FFOV. The étendue of a fiber is approximately constant meaning the output NA can be increased as the area of output face of the fiber is decreased. Reducing the fiber face area to 36.7 μm diameter increases output NA to 0.6. The distal end of the fiber is tapered to meet this specification¹³³.

2.4. *Distal Imaging*

To provide good navigational performance through the fallopian tube and on the surface of the ovary the distal imaging lens design must image a 70 degree FFOV and have a long depth of focus. Additionally, the lenses must image a wide spectral range of 375 to 642 nm to acquire fluorescence and reflectance images. Physically, the lens design is limited to 300- μm diameter elements with reasonable thicknesses and curvatures to reduce manufacturing and construction complexity. The lens design performance was designed to slightly exceed the performance of the CFB, to enable good contrast at CFB-limited spatial frequencies after accounting for moderate construction alignment tolerances.

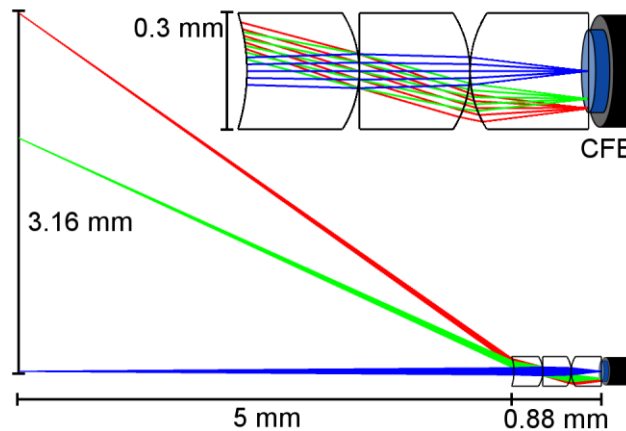


Figure 2. Custom 3 element distal imaging lens. The zoomed out view (bottom) shows the 6.38 mm FFOV at a nominal WD of 5 mm. The total lens length is 0.88 mm and the lens OD is 0.3 mm. A magnified view of the lenses focusing onto the CFB is also shown (top). The image circle of the CFB (blue) has a diameter of 0.19 mm.

The resulting optical design is a custom three-element lens (Fig. 2) that images onto a 3,000 element imaging CFB (Fujikura FIGH-03-215S). The CFB has a coating diameter of 285 μm , image circle diameter of 190 μm , 0.4 NA and typical core-to-core spacing of 3.1 μm to 3.4 μm . The attenuation of light increases significantly for wavelengths shorter than 390 nm, but over a length of at most a few meters necessary for an endoscope is usable at 375 nm.

The minimum 3.1- μm core spacing of the CFB corresponds to a maximum Nyquist cutoff frequency of 161 cycles/mm. The resulting lens design is f/2.4 and achieves at least 40% contrast at the Nyquist cutoff of the CFB for polychromatic imaging for all rays over a 70° FFOV and at all working distances from 3 mm to infinity. While outside of optimal range, contrast remains above 30% for working distances as short as 1.2 mm. The designed polychromatic MTF at a nominal working distance of 5 mm is shown in Fig 3. In most circumstances the lens will be used to image single wavelength reflectance or specific

fluorescence emission bands rather than the full design wavelength range. The MTF is further improved in these scenarios as much of the degradation comes from chromatic aberrations over the full spectral range.

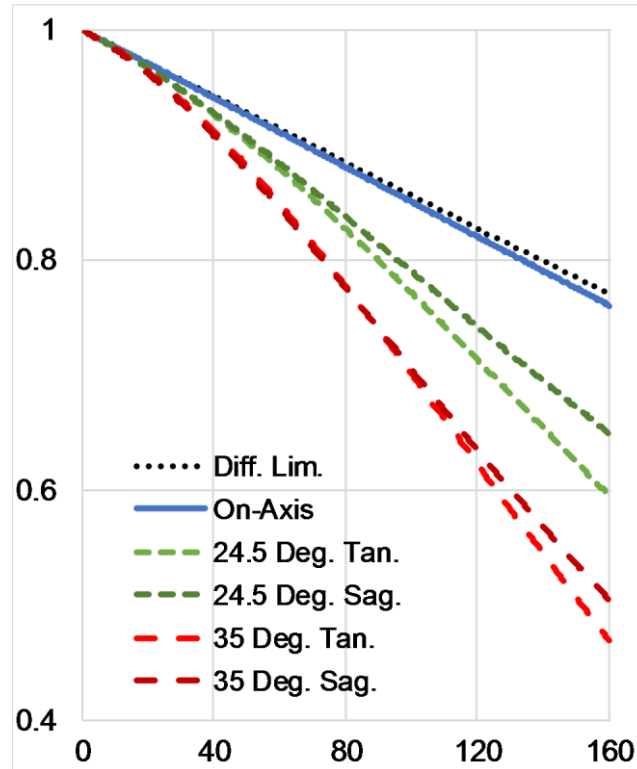


Figure 3. Polychromatic MTF of the 3 element lens design at a working distance of 5 mm. The vertical axis is the modulus of the OTF and the horizontal axis is spatial frequency in cycles per millimeter. The minimum core-to-core spacing of the fiber bundle corresponds to a maximum frequency cutoff of approximately 160 cycles per millimeter.

The design prioritizes correction of spherical aberration, coma, axial color, and astigmatism. Distortion is the most significant remaining aberration followed by field curvature and lateral color. These aberrations are acceptable as resolution (and thus detection ability) is more important than faithful reproduction of a flat, even field while imaging the non-planar geometry inside the fallopian tube. Each individual image uses a single excitation wavelength and narrow emission band. Thus lateral color will not be an

issue within each image, but rather something that can be corrected with software for composite image combination. Distortion does not reduce image sharpness and is an acceptable tradeoff for the wide 70° FFOV. Another design feature includes being image-space telecentric, to provide even illumination onto each fiber in the CFB and maintain a constant image circle diameter of 190 μm to match the CFB.

The three elements in the lens are stacking and only include two unique non-planar surfaces. The stacking design simplifies construction by allowing the lenses to be dropped into the MFI imaging channel of the ferrule and held proximally by the fiber bundle and distally by a cover plate. Normal mounting and alignment techniques are nearly impossible to implement at the miniature scale so tight tolerances on ferrule and the lens dimensions are necessary. Using only two unique nonplanar curvatures reduces costs by simplifying construction and testing for the manufacture. The length of the lens assembly is 0.88 mm allowing ample space to secure the CFB behind the lenses inside a 3-mm-long ferrule. This rigid length is not expected to compromise tracking and navigation in tortuous anatomy.

2.5. Proximal Imaging

The proximal face of fiber bundle is imaged with a modified microscope. An infinity-corrected, UV-enhanced, 20X objective (UApo/340 20X/0.75, Olympus, Tokyo, Japan) is used with a UV-corrected achromat tube lens of focal length 151.5 mm (027-3025, OptoSigma, Santa Ana, California). Olympus objective magnifications are specified assuming a 180 mm focal length tube lens. The shorter focal length tube lens results in a reduction in overall magnification from 20X to 16.8X. The detector (PIXIS 1024, Princeton Instruments, Acton, New Jersey) has 13 x 13 μm pixels. In this configuration the 3.1- μm core-to-core spacing of the CFB is 52.2 microns on the detector which corresponds to

approximately 4 detector pixels per core-to-core spacing, exceeding the Nyquist sampling requirement. In the infinity space between the objective and tube lens, a 10-position filter wheel (LB10W-3985, Sutter Instrument, Novato, California) allows specific emission bands for fluorescence imaging to be selected, or an open position allows for reflectance imaging.

2.6. *Image Processing*

Images were recorded as 16-bit grayscale images using WinView (Princeton Instruments). Individual images were processed using image analysis software (ImageJ, National Institute of Health) and MATLAB (The MathWorks, Natick, Massachusetts). For all images the pixel values outside the fiber bundle image circle were set to 0. The pixels inside the image circle were contrast enhanced such that the brightest 1% and darkest 1% of pixels were respectively set to the maximum and minimum intensity values. After contrast enhancement a slight Gaussian blur was applied to increase visual perception by mitigating the pixilation effects of the CFB without degrading resolution¹³⁵. Color reflectance images were created by weighted combinations of 406 nm illumination as the blue channel, 515 nm illumination for the green channel, and 642 nm illumination for the red channel. Weighting in each channel was adjusted to match perception of accurate color rendition. Color fluorescence images used the light collected from narrow band 450 nm, 532 nm, and 590 nm emission filters. All emission filters had approximate full-width half-maximum of 10 nm. Composite images were created by combining the three emission filter images and weighting the channels to approximate visual color intensity.

2.7. *Imaging System Testing*

The MFI imaging system resolution and field-of-view were characterized and compared to theoretical simulations. Additionally, the imaging system's ability to create a pseudo white light image, and to capture fluorescence images was evaluated.

2.8. *Imaging Resolution Testing*

The imaging lens parameters and approximate fiber bundle parameters were modeled as a complete system (Imager, Five Focal, Boulder, Colorado) to determine the expected minimal resolvable feature size and field of view at working distances of 1, 3, 5, 7 and 10 mm.

The constructed endoscope imaged bar targets on USAF test target at the center and edge of the field for each working distance. The test target was trans-illuminated with white light and images were acquired in grayscale without an emission filter. The resulting images were processed as described above with a Gaussian blur radius of 1.4 pixels.

The resolution was evaluated on-axis and at the edge of the field by imaging a series of bar targets near the resolution cutoff at each location. The edge of the field was considered approximately nine tenths of the radius in order to reasonably fit the bar targets into the field of view. A representative profile was drawn across horizontal and vertical bars of each target and the modulation frequency was measured. The Rayleigh resolution criteria for two points specifies a drop of 26.4% between peak and valley intensity. Modulation contrast is given by the equation:

$$\text{Modulation Contrast} = (I_{\max} - I_{\min}) / (I_{\max} + I_{\min})$$

Thus the Rayleigh criteria corresponds to modulation contrast of 15.21%. Bar targets with modulation contrast for both vertical and horizontal bars greater than or equal to

15.21% were considered resolvable. The width of the minimum resolvable bar was compared to the modeled minimum resolvable feature size for each working distance.

2.9. *Imaging Field of View Testing*

The constructed endoscope's field of view was measured by imaging a square wave target with one line-pair per millimeter at each working distance. The target was trans-illuminated with white light and images were acquired in grayscale without an emission filter. The line pairs were used to measure the approximate field of view in millimeters at each working distance and the compared to the simulated values.

2.10. *Fluorescence Standards Imaging*

Dye	Solvent	Concentration
SR	Ethanol	0.8 μ M
QS	0.5 M H ₂ SO ₄	2 μ M
FI	0.1 M NaOH	0.2 μ M

Table 1. The fluorescence dyes used for testing and their concentration and dissolution solvent. SR is sulforhodamine, QS is quinine sulfate and FI is fluorescein.

The endoscope's ability to image fluorescence was evaluated by imaging cuvettes of sulforhodamine, fluorescein and quinine sulfate (Table 1). The three cuvettes were placed side by side and the five color illumination laser beam was aimed to pass through all three vials. The imaging endoscope was placed perpendicular to the laser beam such that it could image the laser beam path inside each vial. For each of the illumination wavelengths except 642 nm, three images were recorded with narrow band emission filters at 450 nm, 532 nm and 590 nm. A fourth image was recorded without an emission filter. The images were processed as described above. A qualitative composite color image was created using the filtered images. For the composite color image, the 590 nm filter image was mapped to the orange color given by hexadecimal feb900 to match visual perception of the fluorescence

signal. The 450 nm and 532 nm images were mapped to the blue and green channels respectively.

3. Results

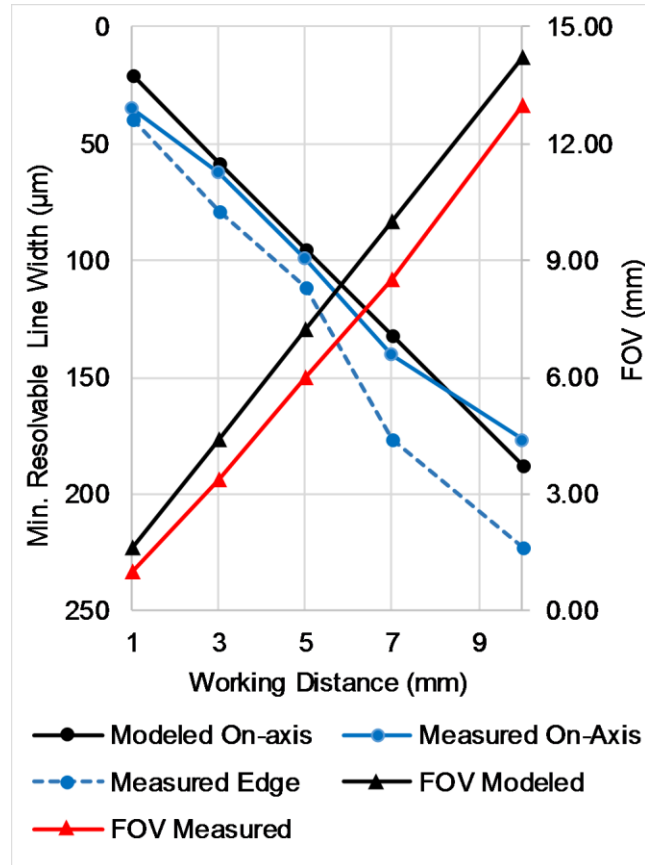


Figure 4. Measured resolution and field of view compared to modeled values at working distances of 1, 3, 5, 7 and 10 mm.

3.1. *Imaging resolution and field of view*

Between the optimal working distance range of 3 to 10 mm the measured minimum resolvable feature size compared favorably with the modeled values (Fig 4). Sample images of on-axis bar target testing at 3, 5 and 10 mm are shown in figure 5. At a working distance of 1 mm the endoscope barely resolved the smallest bars (Group 3, Element 6) on the test target on-axis. Off-axis performance at all working distances was worse than on-

axis as expected from the MTF. The field of view was measured at the same working distances as the resolution. It was consistently slightly smaller than the modeled values as shown in Fig 4.

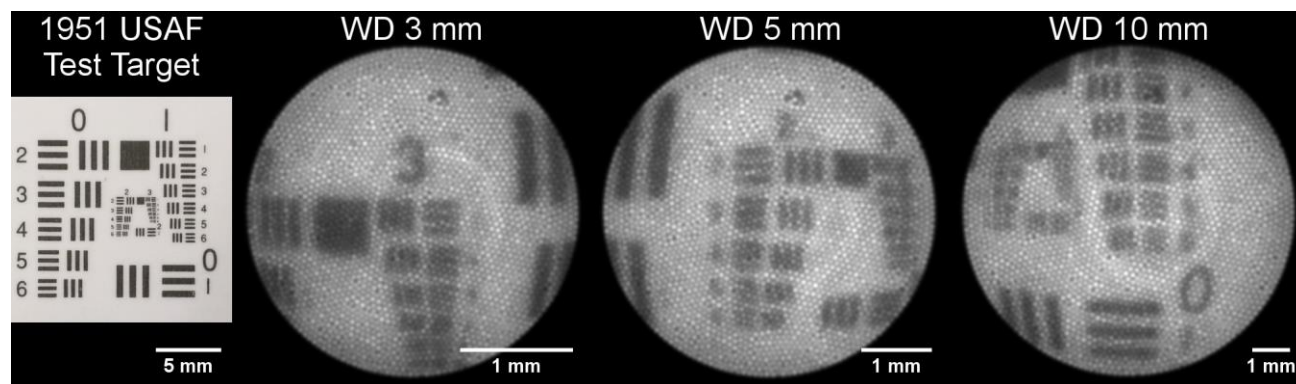


Figure 5. Sample images from on-axis resolution testing. The left most image is a digital camera image of the 1951 USAF test target used. The following three images from left to right are images of the test target acquired using the endoscope at working distances of 3, 5 and 10 mm. Minimum resolvable features were determined to be group 3 element 1, group 2 element 3 and group 1 element 5 respectively.

3.2. Fluorescence imaging

Absorption	Dye		
	SR	QS	FI
250 nm	14.5%	100.0%	29.1%
375 nm	5.3%	15.1%	1.6%
406 nm	1.5%	0.4%	1.8%
515 nm	9.5%	0.0%	13.1%
Emission			
Peak (nm)	593	449	515
FWHM (nm)	34	94	38

Table 2. Absorption and emission properties for each fluorescence dyes. Absorption percentages for each dye are given for each illumination wavelength. Percentages are normalized for each dye such that the peak absorption wavelength is 100%. Emission spectrum peak wavelengths and spectral width at half maximum are also provided. SR is sulforhodamine, QS is quinine sulfate and FI is fluorescein.

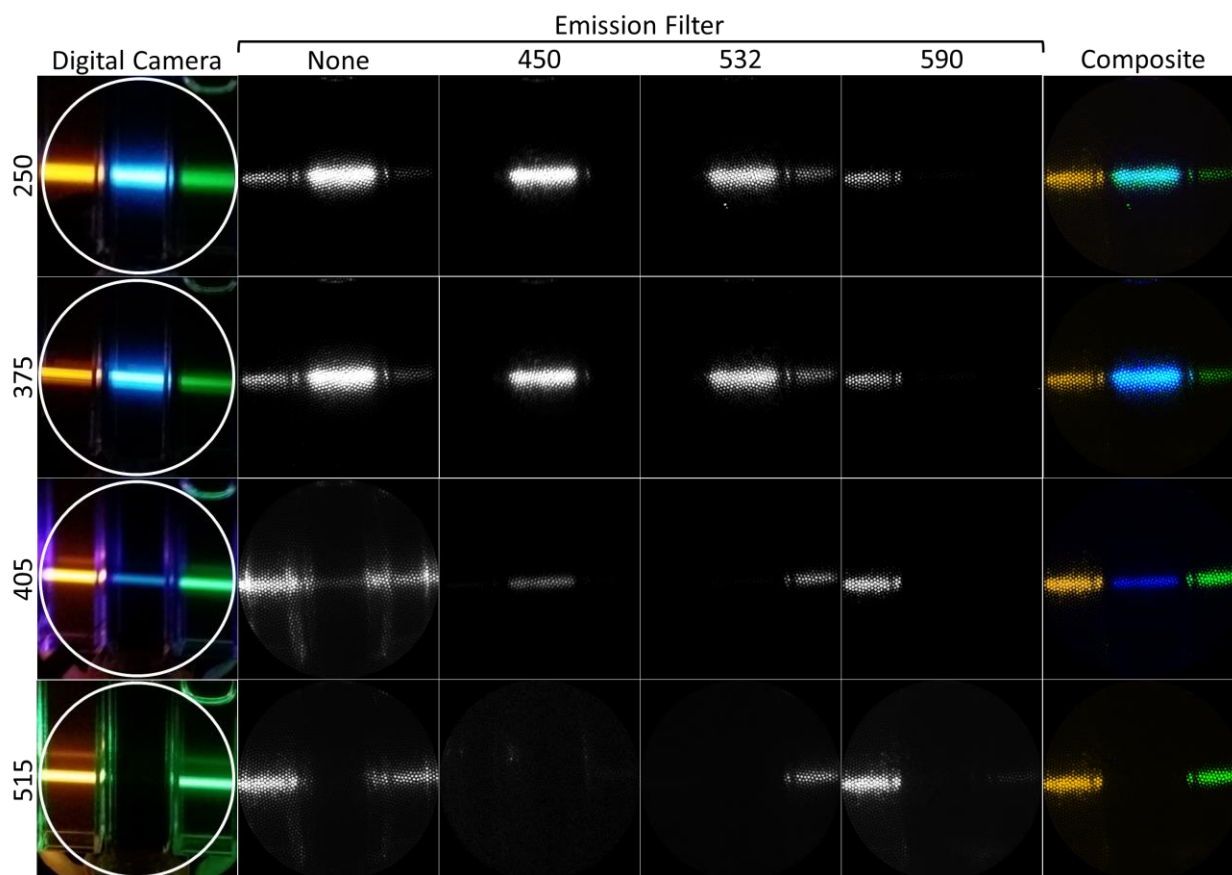


Figure 6. Images of fluorescence dyes in 1 cm wide cuvettes. From left to right the cuvettes contain sulforhodamine, quinine sulfate and fluorescein. Each row of images corresponds to one of the four illumination wavelengths used. The left most column is an image taken with a digital camera. The white circle represents the approximate field of view of the endoscope. From left to right the middle four columns are images taken with the endoscope with no, 450 nm, 532 nm and 590 nm emission filters. The right most column is the color composite image of the 450, 532 and 590 nm emission filter images.

The results of imaging fluorescein, quinine sulfate and sulforhodamine can be seen in figure 6 and the absorption characteristics of the dyes are given in Table 2. Due to the significant variables that account for final image intensity including illumination power and bandwidth, illumination light absorption, fluorophore quantum yield and concentrations, fluorescence emission spectra, emission filter spectra, optical system spectral response, and image processing, the figure is not quantitative. Qualitative comparison of fluorescence intensity of the dyes at each illumination wavelength align well

with predictions based on the approximate quantum yields. The emission filters also successfully blocked the out-of-band illumination light that can be seen in the images with visible illumination and no emission filter. The UV excitation images without a band pass filter have an IR filter in the active filter wheel location to suppress a small residual amount of the 755 nm alexandrite fundamental beam present in the UV beams.

3.3. Color imaging

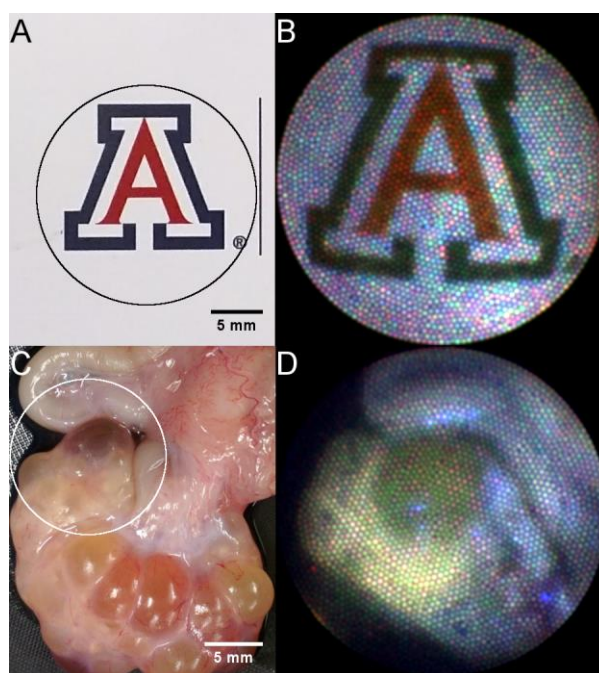


Figure 7. Images on left are taken using a digital camera and are of A) the University of Arizona logo on a business card and C) a section of a porcine reproductive system including ovary with follicles (bottom) and fallopian tube (top left). Corresponding images taken with the endoscope are on the right with field of view approximated by circles overlaid on left images. Image B is a composite color reflectance images taken by sequentially acquiring images with 405, 515 and 642 nm illumination. Image D is a composite color fluorescence image created using 375 nm excitation and sequentially acquiring images using the 450, 532 and 590 nm emission filters.

In order to test the RGB imaging modality, colorful objects were imaged sequentially with the visible illumination sources and the reflectance images were combined into a color composite using ImageJ. Figure 7 shows a color composite image of the University of

Arizona logo on a business card showing faithful reproduction of the saturated red and blue. Color fluorescence imaging was also tested by imaging a section of porcine ovarian and fallopian tube tissue (Fig. 7). The tissue was acquired from local slaughterhouses in a manner approved by the University of Arizona's Institutional Animal Care and Use Committee. The tissue was illuminated with 375 nm light and imaged sequentially with the 450 nm, 532 nm and 642 nm emission filters. The three fluorescence images were then combined into a composite color image.

4. Discussion

A miniature endoscope imaging system capable of wide-field navigation using UV and visible illumination for either autofluorescence or pseudo white-light imaging modalities has been built. The fully constructed endoscope integrates 300- μm diameter lenses and independent illumination channel into a 790 μm outer diameter package for use in the human fallopian tube. The wide field of view with good imaging performance over a large depth of field is ideal for navigation. The ability to perform autofluorescence imaging may allow for increased sensitivity to cancer compared to a standard white-light camera. Achieving the imaging specifications within the specified form factor and over the desired wavelength range posed significant challenges however the demonstrated prototype met specifications and has a modular, flexible design for future endoscopes to build upon.

The small and flexible endoscope could be modified for use in other applications such as insertion through a small bore hypodermic needle. The mechanical design of the endoscope allows for steering capabilities as well as an additional 125- μm lumen for

additional functionality such as high resolution OCT imaging. The illumination system can be customized to include any laser wavelengths from 250 nm through the visible spectrum as needed for the application. Near infrared illumination could also be incorporated into the system, but if used with 250 nm illumination may require custom dichroic mirror coatings. Off-the-shelf dichroic mirrors designed to reflect 250 nm and transmit longer wavelengths typically have high transmission losses in the near infrared. A system performing exclusively fluorescence imaging may be able to combine illumination and imaging into a single path for an even smaller form factor. However, UV illumination wavelengths would be limited by CFB attenuation in a single path configuration.

The imaging lens and ferrule materials cannot exhibit fluorescence when exposed the UV illumination. Autofluorescence signals are typically very low and any additional fluorescence from materials would reduce signal-to-noise ratio to unacceptable levels. This requirement currently eliminates plastics or polymers used in injection molding, 3D printing, diamond turning or GRIN materials. The UV wavelength requirement also limits the proximal imaging system. Assuming a CFB with reasonable UV transmission becomes available, the system that relays the face of the CFB to the detector would require a specialized microscope objective and tube lens to transmit well below 340 nm. Chromatic aberrations and detector spectral response range could be additional issues when imaging over a wider spectral range. Limited choices of UV transmissive fibers necessitated the need to taper the distal tip of the illumination fiber to achieve sufficient illumination angle.

While the endoscope achieved the modeled resolution, the field of view was smaller than expected. The discrepancy could be due to a number of reasons. The most likely cause is the image circle size of the CFB. It is specified to be $190 \pm 20 \mu\text{m}$. The lens design is image space telecentric. This feature minimizes angle-of-incidence dependence of the CFB and provides even illumination across the image. The telecentricity also means the 70-degree field is designed to image onto a 190- μm diameter circle. Thus at a 5 mm working distance, the expected FFOV is 7.22 mm (66 degrees). If the image circle is reduced to 170- μm diameter, then the imaged FFOV would be 5.72 mm (58 degrees) while a 210- μm image circle would correspond to a FFOV of 7.91 mm (75 degrees). The measured FFOV at 5 mm working distance is 6 mm which is within the tolerance range. Changes in fiber bundle image circle diameter will have a trade-off with resolution. The number of fibers remains constant so a smaller image circle will have a decreased average core-to-core spacing of fibers and thus increased resolution potential. This is consistent with the favorable measured against modeled resolution and could explain the better than modeled resolution performance at the 10 mm working distance. The theoretical performance of the lens is overdesigned so a well aligned lens system would still be fiber limited out to an image circle size of 220 μm which corresponds to an 8.65 mm FFOV at 5 mm WD (80 degrees). Larger fields would begin to be clipped by the edge of the proximal-most lens which could cause undesirable stray light reflections. Other factors which could contribute to the reduced FFOV are lens alignment and lens manufacturing tolerances.

The ultimate goal of the endoscope is to be used as an effective screening method for ovarian cancer detection and other diseases in tissue that can be reached via small

diameter lumens (e.g. pancreatic or bile duct). Achieving that goal is a multi-step process. The first generation endoscope presented here successfully proved that MFI imaging can be miniaturized to provide wide-field functional imaging in a sub 800- μ m diameter package. The next step is to improve the design such that robust endoscopes can be built quickly and reliably to provide safe real-time imaging in limited human trials. Additional optical engineering challenges for the second generation system are to simplify, shrink and automate the proximal optical systems to further reduce size and increase portability of system for integration into a surgical cart.

Acknowledgements:

Dr. Khanh Kieu

Financial Disclosure:

Mr. Tate reports grants from United States Department of Defense, grants from National Institute of Biomedical Imaging and Bioengineering , grants from Arizona Technology and Research Innovation Fund Imaging Fellowship, during the conduct of the study; In addition, all authors have a patent *Falloposcope System and Method for Ovarian Cancer Detection* pending.

B.2. Data Storage

The Parent directory containing all design files, presentation, images and other files related to the project are saved on the lab storage drive in the directory:

`\Projects\Grants\DoD_Falloposcope`

Design files are in the subfolders prefixed with 'Design'. All reports including manuscripts, presentations, proposals, and the patent application are in the 'Reports' folder. Images of the construction and images taken by the prototype are in the 'Images' folder.

B.3. Standard Operating Procedures

I have contributed four SOP's to this project. Three are related to the MFI illumination system and one for the construction of the 3 element lenses in the distal tip. The illumination system SOP's are on the full alignment of the Alexandrite laser, the standard operation of the Alexandrite laser and the alignment of the 5-color laser system. All of the SOP's clearly named according to lab conventions and digitally available in the laboratory SOP folder on the lab storage drive.

B.4. Lens Design Files

The MFI proximal imaging system uses off-the-shelf components as described in the submitted manuscript in an infinite conjugate microscope configuration. The components were chosen using first order parameters to ensure Nyquist sampling of the fiber cores on the detector. The proximal imaging system was further modeled in optical design software as the microscope objective clearly had sufficient performance to image the fiber face. The MFI proximal illumination and distal imaging systems were modeled in Zemax OpticStudio before construction. The proximal illumination system uses off-the-shelf components while the distal imaging system uses highly custom miniature optical elements.

B.4.1. Distal 3 element Objective

There are different versions of the design file to evaluate performance when adding a cover plate or immersing in saline. The prescription for the three custom elements constant with the following prescription.

```
System/Prescription Data
GENERAL LENS DATA:
Configuration 2 of 4

Surfaces      :      8
Stop          :      3
System Aperture : Image Space F/# = 2.4
Fast Semi-Diameters : On
Field Unpolarized : On
Convert thin film phase to ray equivalent : On
J/E Conversion Method : X Axis Reference
Glass Catalogs : INFRARED OHARA
Ray Aiming : Paraxial Reference, Cache On
X Pupil Shift :      0
Y Pupil Shift :      0
Z Pupil Shift :      0
X Pupil Compress :      0
Y Pupil Compress :      0
Apodization : Uniform, factor = 0.00000E+00
Reference OPD : Exit Pupil
Paraxial Rays Setting : Ignore Coordinate Breaks
```

Method to Compute F/# :Tracing Rays
 Method to Compute Huygens Integral : Force Spherical
 Print Coordinate Breaks :On
 Multi-Threading :On
 OPD Modulo 2 Pi :Off
 Temperature (C) : 2.00000E+01
 Pressure (ATM) : 1.00000E+00
 Adjust Index Data To Environment :Off
 Effective Focal Length : 0.174421(in air at system temperature and pressure)
 Effective Focal Length : 0.174421(in image space)
 Back Focal Length : -0.003277468
 Total Track : 0.883634
 Image Space F/# : 2.4
 Paraxial Working F/# : 2.40822
 Working F/# : 2.405156
 Image Space NA : 0.2032869
 Object Space NA : 0.007047936
 Stop Radius : 0.04384011
 Paraxial Image Height : 0.1225492
 Paraxial Magnification : -0.0339468
 Entrance Pupil Diameter : 0.07267543
 Entrance Pupil Position : 0.1556675
 Exit Pupil Diameter : 0.7203042
 Exit Pupil Position : -1.732008
 Field Type : Angle in degrees
 Maximum Radial Field : 35
 Primary Wavelength [μm] : 0.406
 Angular Magnification : 0.1008955
 Lens Units : Millimeters
 Source Units : Watts
 Analysis Units : Watts/cm²
 Afocal Mode Units : milliradians
 MTF Units : cycles/millimeter
 Include Calculated Data in Session File :On

SURFACE DATA SUMMARY:

Surf	Type	Radius	Thickness	Glass	Diameter
OBJ	STANDARD	Infinity	5.0000000		7.2200740
1	STANDARD	-0.5000143	0.2910416	S-FPM3	0.3000000
2	STANDARD	-0.2795876	0.0000000		0.3000000
STO	STANDARD	Infinity	0.0000000		0.0876802
4	STANDARD	Infinity	0.2862806	S-FPL51Y	0.3000000
5	STANDARD	-0.2795876	0.0000000		0.3000000
6	STANDARD	0.2795876	0.3063117	SAPPHIRE	0.3000000

7	STANDARD	Infinity	0.000000		0.300000
IMA	STANDARD	Infinity			0.1988509

Fields : 3

Field Type : Angle in degrees

#	X-Value	Y-Value	Weight
1	0.000000	0.000000	1.500000
2	0.000000	24.500000	2.000000
3	0.000000	35.000000	1.000000

Wavelengths : 5

Units: μm

#	Value	Weight
1	0.375000	1.000000
2	0.406000	2.000000
3	0.515000	1.000000
4	0.642000	1.000000
5	0.450000	1.000000

MULTI-CONFIGURATION DATA:

Configuration 1:	Surf 0 Thickness:	3
Configuration 2:	Surf 0 Thickness::	5
Configuration 3:	Surf 0 Thickness:	7
Configuration 4:	Surf 0 Thickness:	10

B.4.2. Proximal Illumination System

This design is also described in the submitted manuscript. The final design filename is 'IlluminationSystemSimpleFinalARnegative-CollimaterAdjustments514.zmx' with the following lens prescription:

Configuration 5 of 5

GENERAL LENS DATA:

Surfaces	:	13
Stop	:	5
System Aperture	:	Entrance Pupil Diameter = 4.5
Fast Semi-Diameters	:	On
Field Unpolarized	:	On
Convert thin film phase to ray equivalent	:	On
J/E Conversion Method	:	X Axis Reference
Glass Catalogs	:	SCHOTT INFRARED CORNING

Ray Aiming : Off
 Apodization : Uniform, factor = 0.00000E+00
 Reference OPD : Exit Pupil
 Paraxial Rays Setting : Ignore Coordinate Breaks
 Method to Compute F/# : Tracing Rays
 Method to Compute Huygens Integral : Force Spherical
 Print Coordinate Breaks : On
 Multi-Threading : On
 OPD Modulo 2 Pi : Off
 Temperature (C) : 2.00000E+01
 Pressure (ATM) : 1.00000E+00
 Adjust Index Data To Environment : Off
 Effective Focal Length : 11.68679(in air at system temperature and pressure)
 Effective Focal Length : 11.68679(in image space)
 Back Focal Length : 5.657147
 Total Track : 51.08499
 Image Space F/# : 2.597064
 Paraxial Working F/# : 2.597064
 Working F/# : 2.573124
 Image Space NA : 0.1890533
 Object Space NA : 2.25e-10
 Stop Radius : 2.245066
 Paraxial Image Height : 0
 Paraxial Magnification : 0
 Entrance Pupil Diameter : 4.5
 Entrance Pupil Position : 6.002198
 Exit Pupil Diameter : 2.368287
 Exit Pupil Position : 6.24274
 Field Type : Angle in degrees
 Maximum Radial Field : 0
 Primary Wavelength [μm] : 0.642
 Angular Magnification : 0
 Lens Units : Millimeters
 Afocal Mode Units : milliradians
 MTF Units : cycles/millimeter
 Include Calculated Data in Session File : On

Fields : 1
 Field Type : Angle in degrees

#	X-Value	Y-Value	Weight
1	0.000000	0.000000	1.000000

Vignetting Factors

#	VDX	VDY	VCX	VCY	VAN
1	0.000000	0.000000	0.000000	0.000000	0.000000

Wavelengths : 1
 Units: μm

#	Value	Weight
1	0.642000	1.000000

SURFACE DATA SUMMARY:

#	Type	Comment	Radius	Paraxial Focal Length	Thickness	Material	Coating
OBJ	Std.		Infinity	-	INF		
1	Std.		Infinity	-	5.00		
2	Parax	Red		456.06	1.00		
3	Parax	Green		593.43	7.50		
4	Parax	Blue		1244.84	16.00		
5	Std.		Infinity	-	0.00		
6	Std.		Infinity	-	2.50	C79-80	ZEC_UVAR
7	Std.	48325	91.69	-	0.00		ZEC_UVAR
8	Std.		Infinity	-	30.00		
9	Std.	LA5315	8.67	-	4.26	CAF2	
10	Std.		Infinity	-	1.00		
11	Std.	LA5315	8.67	-	4.26	CAF2	
12	Std.		Infinity	-	5.57		
IMA	Std.		Infinity	-			

MULTI-CONFIGURATION DATA:

Configuration 1:

1 Wavelength 1 :	0.25
2 Ignore 6-7 :	0
3 Ignore 3-3 :	1
4 Ignore 4-4 :	1
5 Ignore 2-2 :	1

Configuration 2:

1 Wavelength 1 :	0.375
2 Ignore 6-7 :	1
3 Ignore 3-3 :	1
4 Ignore 4-4 :	1
5 Ignore 2-2 :	1

Configuration 3:

1 Wavelength 1 :	0.406
2 Ignore 6-7 :	1
3 Ignore 3-3 :	1
4 Ignore 4-4 :	0
5 Ignore 2-2 :	1

Configuration 4:

1 Wavelength 1 :	0.514
2 Ignore 6-7 :	1
3 Ignore 3-3 :	0
4 Ignore 4-4 :	1
5 Ignore 2-2 :	1

Configuration 5:

1 Wavelength 1 :	0.642
2 Ignore 6-7 :	1
3 Ignore 3-3 :	1
4 Ignore 4-4 :	1
5 Ignore 2-2 :	0

B.5. MATLAB scripts

MATLAB was used in this project for Gaussian beam modeling of the distal OCT design, image processing of acquired by MFI and measuring modulation contrast on images of USAF bar targets. All three sets of MATLAB scripts and functions follow.

B.5.1. Gaussian Beam Modeling

As discussed in the introduction Gaussian beam modeling is a useful technique to design all fiber based OCT optics. The technique propagates a Gaussian beam through the optical system as a q parameter through ABCD matrices. Functions to generate an ABCD matrix for each surface type are defined first. Then a script follows that uses the functions to model the complete optical system. The scripts are well commented so the user can easily make modifications for future applications.

```
function [ M ] = ABCD_IntRef( n1,n2 )
%Outputs ABCD matrix for refraction through a flat interface
% n1 is index before interface and n2 is after
M = [1 0;0 n1/n2];

end

function [ M ] = ABCD_CurvRef( n1, n2, R )
%Refract at curved interface
% n1 is index before surface
% n2 is index after
% R is rad of curvature

M = [1 0;-(n2-n1)/(n2*R) n1/n2];

End

function [ M ] = ABCD_Prop(l)
%Outputs ABCD matrix for prop through constant index material
% input length of prop
M = [1 l;0 1];

End

function [ M ] = ABCD_ThinLens( f )
%Outputs ABCD mat for thin lens
% f is focal length

M=[1 0;-1/f 1];
```

```

end

function [ M ] = ABCD_GRIN( g, l )
%Outputs ABCD mat for GRIN lens
%   g is gradient pitch such that index is a function of radius r and
g
%   n(r)=n1(1-.5*g^2*r^2)
%   l is length of GRIN
%   Note: Pitch P=2*pi/g

M = [cos(g*l) (1/g)*sin(g*l);-g*sin(g*l) cos(g*l)];

end

%% ABCD matrix gaussian beam prop for OCT with GRIN lens
% Code to propogate gaussian beam through optical system. The code
% calculates the q-factor after each element and plots the gaussian
beam
% waist through the system. Use 'ABCD_*.m' functions to generate ABCD
% matrices. The 'BeamWaist.m' function generates the beam waist
through z
% given the q factor for a give space.
%
% Note that if you want to change the number of spaces you need to
change
% the num_spaces variable, add/delete the space, add/delete the ABCD
% matrices for the space and following interface, add/delete the
desired
% plotting code.
%
% All lengths are microns. Distances must be integers
%
% Code could use some error checking for when rayleigh range or waist
are
% outside of the final medium.
%
% A GUI would be nice
%
% Last updated: 1/28/2016
% Author: Tyler Tate

%% Set Wavelength

lambda = 1; %microns

%% Set number of mediums light propgates through including SM fiber

num_spaces = 6; %beam exists in n spaces (e.g. 5 spaces would be: SM
fiber, no-core, GRIN, no-core, air)

%% Code initializes various vectors. You should not need to edit this
section

```

```

num_mats = num_spaces*2-1; %num ABCD matrices (spaces plus interfaces)
M = zeros(2,2,num_mats); %init 3D vector of ABCD mats.
n = ones(num_spaces,1); %init index vector
d = zeros(num_spaces,1); %init dist traveled vector
w0 = ones(num_spaces,1); %init beam waist vector
z_loc = zeros(num_spaces,1); %init vector of distance from current pos
to beam waste
z_shift = zeros(num_spaces,1); %init vector to track beam waste axis
shifts
q = zeros(num_spaces,1); %init vector of q factor after each mat
space_name = cell(num_spaces,1); %init vector of space names

%% Now define each propogation medium (space)

% space 1. (where the beam starts)
% SMF-28 fiber in this example
%edit these values
s = 1; %current space number
space_name(s) = cellstr('780HP'); %set name of space
z_loc(s) = 0; %beam waist located at z=0
z_shift(s) = z_loc(s); %set shift for gaussian equations
SM_fiber_dia = 125; %microns
MFD = 5; %mode field diameter in microns. 5.9 for HI1060, 5 for HI780
w0(s) = MFD/2; %beam waist exiting fiber
% note from thorlabs website forum:
% refractive index of 780HP at 780nm: Core = 1.4598 Clad = 1.4537
% from http://fibersensor-physics450.wikidot.com/ the index of pure
silica
% at 980 is 1.4507 and the 780HP fiber is +.0059 higher = 1.4566
% Thus I am estimating that index at 890 is average of those two.
n(s) = 1.458; %approx index of 780hp fiber
d(s) = 0; %Length of propogation. This should be zero for this
application
%don't edit this
q(s) = 1i*n(s)*pi*w0(s)^2/lambda; %q factor exiting fiber

%space 2. (prop through no-core)
%No-core fiber parameters
s=2;
space_name(s) = cellstr('NC'); %set name of space
%Information from thorlabs on FG125LA: "We don't specify the
refractive
% index for this fiber, but based on using the raw glass preform data,
% the cladding index could be 1.452 at 890 nm"
% Molly had 1.4487 from unknown source.
% The difference between the two is 1-2% in terms of final parameters.
n(s) = 1.452; %index of no-core fiber
d(s) = 212; %physical length of no-core in microns (Dirk example=360)

%space 3 (prop through grin)
%GRIN Fiber parameters
s = 3;
space_name(s) = cellstr('GRIN'); %set name of space

```

```

ap_GRIN = 62.5; %clear aperture diameter of GRIN fiber
n(s) = 1.478; %reference index for GRIN
% Note that pitch  $p=2\pi/g$ . For  $g=.006$  this gives 1047.2 microns.
% So for every 523.6 micron multiple added to length, same ending
% parameters result, but image flips.
g = .006; %GRIN profile in reciprocal microns
d(s) = 160; %physical length in microns

%space 4. (prop through 2nd no-core)
%No-core fiber parameters
s=4;
space_name(s) = cellstr('NC'); %set name of space
n(s) = n(2); %index of no-core fiber
d(s) = 210; %physical length of no-core in microns

%space 5
%Air gap between fiber and tissue
s=5;
space_name(s) = cellstr('Gap');
n(s) = 1;
d(s) = 120; %physical length in microns

%space 6
%tissue space
s=6;
space_name(s) = cellstr('Sample'); %set name of space
n(s) = 1; %tissue
d(s) = 300; %physical length to plot prop in tissue (make longer than
WD to graph properly)

%% Define ABCD matrices
% Generate ABCD matrix for each space and interfaces between them.

M(:, :, 1) = ABCD_Prop(d(1)); %prop in space 1. ID mat is d(1)=0
M(:, :, 2) = ABCD_FlatRef(n(1), n(2)); %Interface 1 (fiber to no-core)
M(:, :, 3) = ABCD_Prop(d(2)); %prop through no core
M(:, :, 4) = ABCD_FlatRef(n(2), n(3)); %Interface 2 (no-core to GRIN)
M(:, :, 5) = ABCD_GRIN(g, d(3)); %prop through GRIN
M(:, :, 6) = ABCD_FlatRef(n(3), n(4)); %Interface 3 (GRIN to no-core)
M(:, :, 7) = ABCD_Prop(d(4)); %prop through no core
M(:, :, 8) = ABCD_FlatRef(n(4), n(5)); %Interface 4 (no-core to air gap)
M(:, :, 9) = ABCD_Prop(d(5)); %prop through air gap
M(:, :, 10) = ABCD_FlatRef(n(5), n(6)); %Interface 5 (air gap to tissue)
% M(:, :, x) = ABCD_Prop(d(5)); %Final prop through air
% Note that the final air propagation matrix isn't actually used to
plot
% the beam waist as the final interface gives the q-factor with
sufficient
% information to plot the waist any distance beyond the final
interface.
% It is included here for completeness and use for future
functionality.

%% Transfer gaussian beam through each ABCD matrix

```

```

% First define a distance vector that tracks total traveled distance
of beam
d_cum = zeros(length(d),1);
d_cum(1) = d(1);
for k=2:length(d_cum)
    d_cum(k) = d_cum(k-1)+d(k);
end

% Loop does a propagation and the following interface on each
iteration
for k=1:num_spaces-1
    in = [q(k);1]; %input
    Msys = M(:, :, 2*k)*M(:, :, 2*k-1); %ABCD mat for prop then interface
    out = Msys*in; %output
    q(k+1)= out(1)/out(2); %generate new normalized q factor
    z_loc(k+1) = real(q(k+1)); %beam waist location is real part of q
    factor
    z_shift(k+1) = d_cum(k)-z_loc(k+1); %track beam waist loc relative
to each space
    w0(k+1) = sqrt(imag(q(k+1))*lambda/(n(k+1)*pi)); %calc beam waist
for each space
end

%% Generate plot of beam waist size through system

%note that q-factor gives beam waist and location. The Gaussian
equations are defined such that the beam waist is located at z=0.
Z_shift
%is used to shift the output from gaussian equations to the global
coordinate system.

%define axes
xmin = -200; %distance left of fiber face to plot for visual clarity
xmax = sum(d(1:end)); %distance to plot right of zero
ymin = 0; %optical axis is bottom of plot
ymax = SM_fiber_dia/2; %height of plot limited to SM fiber radius
z = linspace(z_loc(1),xmax,xmax-z_loc(1)+1); %define z axis (1
sample/micron)
h = figure('Position', [20, 200, 750, 450]); %init figure loc and size
axis([xmin xmax ymin ymax]); %set fig axes
hold on %set so figure overlays each of the following plots

%Plot features for SMF fiber
%plot beam in fiber as horizontal line for visualization
line([xmin 0],[w0(1) w0(1)], 'Color', 'b');
%add vertical line for fiber/no-core interface
s = 1;
line([d_cum(s)+1 d_cum(s)+1], [0 ymax], 'Color', 'k');
%add text box for fiber specs
str = {char(space_name(s)), 'n =', num2str(n(s), '%.4f\n'), 'MFD =',
[num2str(MFD, '%.2f') '\mum']};
text((xmin+d(s))/2, ymax*.9, str, 'HorizontalAlignment', 'center', 'Vertica
lAlignment', 'top');

```

```

%plot beam in 1st no-core
s = 2; %no-core is space 2
domain = z(d_cum(s-1)+1:d_cum(s)+1); %it exists in this range
%calc beam waist over appropriate domain and z_shift
nc_beam = BeamWaist(domain-z_shift(s),w0(s),lambda,n(s));
plot(domain, nc_beam)
line([sum(d(1:s)) sum(d(1:s))], [0 ymax],'Color','k');
str = {char(space_name(s)), 'n =', num2str(n(s),'%.4f\n'), 'L =',
[num2str(d(s),'%.0f') '\mum']};
text((d_cum(s-1)+d_cum(s))/2,ymax*.9,str,'HorizontalAlignment','center','VerticalAlig
nment','top');

% add line for GRIN/Air interface and text in GRIN
s = 3;
line([d_cum(s)+1 d_cum(s)+1], [0 ymax],'Color','k');
str = {char(space_name(s)), 'n =', num2str(n(s),'%.4f\n'), 'L =',
[num2str(d(s),'%.0f') '\mum'],'g=', [num2str(g*1000,'%.2f'), '']};
text((d_cum(s-1)+d_cum(s))/2,ymax*.9,str,'HorizontalAlignment','center','VerticalAli
gnment','top');
%Following does a seperate ABCD prop through GRIN in short intervals
for
%plotting purposes.
int = 15; %interval width between points plotted in GRIN
domain = d_cum(s-1):int:d_cum(s); %domain in GRIN
domain = domain(2:end); %Don't want first coordinate as its on
boundary
dom_size = length(domain); %having length of vector is useful
waistheight = zeros(dom_size,1); %init vector for waist heigh inside
GRIN
Mtemp = ABCD_GRIN(g,int); %This is the prop vector in the GRIN with
interval width
z_loc_GRIN = zeros(dom_size,1); %init vector of distance from current
pos to beam waist
z_shift_GRIN = zeros(dom_size,1); %init vector to track beam waist
axis shifts
w0_GRIN = zeros(dom_size,1); %init vector to track min waist through
GRIN
qtemp = q(s); %set initial q factor in GRIN
%loop to calc q factor at each interval location through GRIN
for k=1:dom_size
    in = [qtemp;1]; %input vector
    out = Mtemp*in; %output vector
    qtemp = out(1)/out(2); %generate new normalized q factor
    z_loc_GRIN(k) = real(qtemp); %dist to waist
    z_shift_GRIN(k) = d_cum(s-1)+k*int-z_loc_GRIN(k); %shift loc to
global coordinates
    w0_GRIN(k) = sqrt(imag(qtemp)*lambda/(n(s)*pi)); %waist for
current beam shape
    waistheight(k) = BeamWaist(domain(k)-
z_shift_GRIN(k),w0_GRIN(k),lambda,n(s)); %find waist height at current
location
end

```

```

%plot results on graph
plot(domain,waistheight,':');
%plot line representing max beam height in GRIN (clear aperture)
line([d_cum(s-1) d_cum(s)], [ap_GRIN/2
ap_GRIN/2], 'Color','k', 'LineStyle',':');

%plot beam in 2nd no-core
s = 4; %2nd no-core is space 4
domain = z(d_cum(s-1)+1:d_cum(s)+1); %it exists in this domain
%calc beam waist over appropriate domain and z_shift
nc_beam2 = BeamWaist(domain-z_shift(s),w0(s),lambda,n(s));
plot(domain, nc_beam2)
line([d_cum(s)+1 d_cum(s)+1], [0 ymax], 'Color','k');
%add text box for no-core
str = {char(space_name(s)), 'n =', num2str(n(s), '%.4f\n'), 'L =',
[num2str(d(s), '%.0f') '\mum']};
text((d_cum(s-
1)+d_cum(s))/2, ymax*.9, str, 'HorizontalAlignment','center', 'VerticalAli
gnment','top');
%add dotted line to represent angle polish of 2nd no-core (assume 45
deg)
line([d_cum(s)-SM_fiber_dia/2 d_cum(s)], [0
SM_fiber_dia/2], 'Color','k', 'LineStyle',':');

%plot beam in air gap between fiber edge and tissue
s = 5; %space 5
domain = z(d_cum(s-1)+1:d_cum(s)+1); %it exists in this domain
%calc beam waist over appropriate domain and z_shift
ag_beam = BeamWaist(domain-z_shift(s),w0(s),lambda,n(s));
plot(domain, ag_beam)
line([d_cum(s)+1 d_cum(s)+1], [0 ymax], 'Color','k');
%add text box for no-core
str = {char(space_name(s)), 'n =', num2str(n(s), '%.4f\n'), 'L =',
[num2str(d(s), '%.0f') '\mum']};
text((d_cum(s-
1)+d_cum(s))/2, ymax*.9, str, 'HorizontalAlignment','center', 'VerticalAli
gnment','top');

%plot beam in tissue after air gap
s = 6;
domain = z(d_cum(s-1)+1:d_cum(s)+1);
%calc beam waist over appropriate domain and z_shift
tissue_beam = BeamWaist(domain-z_shift(s),w0(s),lambda,n(s));
plot(domain, tissue_beam)
w0_loc = d_cum(s-1)+1-z_loc(end);
line([w0_loc w0_loc], [0 w0(s)], 'Color','r');
%add Rayleigh range to plot
zr = w0(s)^2*pi*n(s)/lambda;
line([w0_loc-zr w0_loc-zr], [0 sqrt(2)*w0(s)], 'Color','g');
line([w0_loc+zr w0_loc+zr], [0 sqrt(2)*w0(s)], 'Color','g');
str = {char(space_name(s)), ['n =', num2str(n(s), '%.4f\n')], ...
['WD=' num2str(-z_loc(s), '%.0f\n') '\mum'], ...
['Spot Dia=' num2str(2*w0(s), '%.2f') '\mum'], ...
['FWHM=' num2str(2*w0(s)/1.699) '\mum'], ...

```

```

        ['\lambda=', num2str(lambda*1000, '%.0f'), 'nm'], ...
        ['DOF=' num2str(2*zr, '%.0f') '\mum']]);
text((d_cum(s-1)+d_cum(s))/2, ymax*.9, str, 'HorizontalAlignment', 'center', 'VerticalAlignm
gnment', 'top');

%final graph formatting
hold off
title('Gaussian Beam Waist (1/e^2 intensity) Through OCT Optics');
xlabel('Distance in microns');
ylabel('Beam radius in microns');

figure
s = 5; %air gap between fiber output and tissue
domain = z(d_cum(s-1)+1:d_cum(s+1)); %it exists in this domain
xmax = max(domain)-d_cum(s-1);

n_fig2 = 1; %This figure is for reference when testing in air. index =
1
ag_beam = BeamWaist(domain-z_shift(s), w0(s), lambda, n_fig2);
plot(ag_beam)
axis([0 xmax ymin ymax]); %set fig axes
title('Beam Waist (1/e^2 intensity) in air immediately after exiting
NC');
xlabel('Distance in microns');
ylabel('Beam radius in microns');
w0_loc = -z_loc(s);
line([w0_loc w0_loc], [0 w0(s)], 'Color', 'r');
zr = w0(s)^2*pi*n_fig2/lambda;
line([w0_loc-zr w0_loc-zr], [0 sqrt(2)*w0(s)], 'Color', 'g');
line([w0_loc+zr w0_loc+zr], [0 sqrt(2)*w0(s)], 'Color', 'g');
%add text box for testing in air
str = {'Air testing specs', ['n=' num2str(n_fig2, '%.1f\n')], ['WD='
num2str(-z_loc(s), '%.0f\n') '\mum'], ['Spot Dia='
num2str(2*w0(s), '%.2f') '\mum'], ['FWHM=' num2str(2*w0(s)/1.699)
'\mum'], ['\lambda=', num2str(lambda*1000, '%.0f'), 'nm'], ['DOF='
num2str(2*zr, '%.0f') '\mum']];
text(xmax/2, ymax*.9, str, 'HorizontalAlignment', 'center', 'VerticalAlignm
ent', 'top');

```

B.5.2. CFB Image Processing

The CFB relays images from the distal MFI objective lens to the proximal end of the CFB where they are imaged onto the detector. The acquisition software is winview which by default saves all image files with the proprietary ‘.SPE’ extension. The raw images qualitatively suffer from the distraction of the sharp honeycomb pattern of the CFB. In this section I provide

MATLAB scripts to convert images to the standard '.TIF' format and then process the images to improve qualitative visualization. All MATLAB scripts and functions are saved in the directory:

C:\Users\Tyler\Google Drive\TOL\DoD_Falloposcope\Images\CFB Image Processing

Copies of all '.SPE' images in a folder can be converted to '.TIF' files and saved in a new folder using the following 'SpeReader.m' script. This script calls on the function 'SpeReader.m' available for free on MathWorks file exchange and saved in the directory.

```
%% Script to save a copy of SPE images as TIF images.

root_dir = 'PATH...\Endoscopic MFI\Winview Images\EXAMPLE';
% subfolder of root directory with SPE images
% folder should ONLY contain SPE images to be converted.
dirSPE = [root_dir '\SPE\EXAMPLE'];
% subfolder of root directory to create and save TIF copies
dirTIF = [root_dir '\TIFF\EXAMPLE\'];
mkdir(dirTIF);
% Read in SPE filenames
fileList = getAllFiles(dirSPE);
n = length(fileList);
fileName = cell(n,1);
% Read in each image from dirSPE, convert, save in dirTIF
for ii = 1:n
    imOb = SpeReader(fileList{ii});
    sloc = strfind(fileList{1}, '\');
    fileName{ii} = fileList{ii}(sloc(end)+1:end-4);
    img = read(imOb);
    wdir = [dirTIF fileName{ii} '.tif'];
    imwrite(img,wdir);
end
```

Once the images are saved as .TIF files the image quality can be improved with image processing. The function 'CFB_BatchProcess.m' performs automated image processing on all images in a directory and saves the processed images in a new user specified directory. The processing first located the CFB in the image using the developed function 'CFB_Find.m' that relies on MATLAB's built in circle find capabilities. Based on the determined circle location the image is cropped to a user specified size with the CFB centered in the cropped image using the developed function 'CFB_Crop.m'. Another supporting function, 'CFB_Mask.m', is used to create a mask of the CFB and set all pixels outside the CFB mask to zero as they do not contain

any image signal. A third supporting function, 'CFB_Norm.m' then uses the mask to saturate the pixels inside the CFB according to a user specified saturation range. The image is then resized if specified by the user using the nearest neighbor algorithm to avoid loss of image quality due to interpolation algorithms. Finally, a Gaussian blur with pixel size specified by the user is applied to the image. When done with a small radius (1-1.5 pixels) the distracting honeycomb pattern of the CFB is reduced and the relayed image becomes easier to identify. Image resolution is not lost if the blur is small enough to spread the signal from each fiber into the signal-free cladding region around each fiber without blurring into adjacent fiber signals.

This process is completed on all images in the directory. The automated processing is dependent on MATLAB being able to identify the location and size of the CFB. For images with very low signal the pixels inside the CFB will not be distinguishable from detector noise. This can be an issue for fluorescence emission imaging when only a small region of the object is emitting a signal such as in the cuvette images in the manuscript. The problem can be solved by preprocessing the images manually in ImageJ. Using ImageJ the user can draw a circle around the CFB and then set all pixels outside the circle to zero. This will create a significant enough pixel difference between the background and the CFB that MATLAB will be able to locate the CFB.

All functions are well commented for ease of future adaptation and use. This processing procedure was developed for the falloposcope project, but is generally applicable to any imaging using a CFB. The 'CFB_BatchProcess.m' function and its supporting functions follow:

```
function CFB_BatchProcess(sigma,crop_size,saturation_range,scale)
%% Processes a folder of CFB images with specified settings
% INPUTS
% - dir_in: folder with the images.
% - dir_out: folder to write processed images
% - sigma: Guassian blur size. Set to 0 to skip blurring step
% - crop_size: Crop image to specified size centered on CFB. EX1:
%   crop_size=280 will make a 280x280 pixel image. EX2:
crop_size=[280,300]
%   will output images with width 280 and height 300. EX3: crop_size=0
will
%   skip this processing
```

```

% - saturation_range=[low_in, high_in]: Contrast limits for input
image,
%   specified as a two-element numeric vector with values between 0
and 1.
%   Values below low_in and above high_in are clipped; If you specify
an
%   empty matrix ([ ]), imadjust uses the default limits [0 1]. EX:
%   [.01,.99] will saturate the lowest and highest 1 percent of pixel
%   values inside the circular mask containing the CFB.
% - scale: scalar value greater than 1 will increase image size using
%   'nearest neighbor algorithm'. Set to 1 to skip. Scaling will take
place
%   after masking, cropping and normalizing. Gaussian blur will be
applied
%   after scaling with sigma = sigma*scale. Further testing needed to
%   verify no loss in image quality.

dir_in = uigetdir('DEFAULT DIRECTORY','Please select folder with
images for processing');
dir_out = uigetdir('DEFAULT DIRECTORY','Please select folder to save
processed images');

% % make write directory if it does not exist.
% if ~exist(dir_out,'dir')
%     mkdir(dir_out);
% end

% get list of all files in read directory
fileList = getAllFiles(dir_in);
n = length(fileList);
fileName = cell(n,1);

if scale>1
    sigma = sigma*scale;
end

%loop over and process each image in read directory.
for ii = 10:n
%   read image
    img = imread(fileList{ii});
%   isolate img name from directory
    sloc = strfind(fileList{ii},'\');
    fileName{ii} = fileList{ii}(sloc(end)+1:end-4);
%   find center and radius of CFB
    [c,r] = CFB_Find(img);
%   crop image to specified size centered on CFB
    if crop_size ~= 0
        [img,left,top] = CFB_Crop(img,crop_size,c);
        c = c - [left,top] + [1,1]; %update CFB center location
    end
%   create mask (circle mask around CFB)
    mask = CFB_Mask(img,c,r+.5);
%   mult img by mask to set all pixels outside CFB to zero
    img = img.*mask;

```

```

%   normalize image using only pixels in mask with input saturation
range
    img = CFB_Norm(img,saturation_range,mask);
%   if scale factor is set greater than 1 then upscale image and
increase
%   sigma factor accordingly
    if scale>1
        img = imresize(img,scale,'nearest');
    end
%   if sigma is larger than zero then apply gaussian blur to image
    if sigma~=0
        img = imgaussfilt(img,sigma);
    end
%   Create new full output file name and write to dir_out
    wdir = [dir_out '\' fileName{ii} '.tif'];
    imwrite(img,wdir);
end

end

```

```

function [center, radius] = CFB_Find(img)
%% takes in image of Coherent Fiber Bundle and outputs center, radius
of CFB

%set variables. Could be option inputs with varargin in future.
BWthresh = .0127; %set via trial and error
StrelSize = 5;
minRad = 100; %expected rad -30
maxRad = 160; %expected rad +30
% note: find circle is more sensitive, but slower with larger radius
range.
% The increased sensitivity is inexplicable to me at this point.

%dilate, erode and bw make solid circle in CFB loc for circle find
img = padarray(img,[StrelSize,StrelSize]); % ensures sufficient border
around CFB
SE = strel('disk',StrelSize);
tmp = imdilate(img,SE);
tmp = imerode(tmp,SE);
tmp = im2bw(tmp,BWthresh);

%using bw image find circle around CFB
[center,radius] =
imfindcircles(tmp,[minRad,maxRad],'Sensitivity',.91);
center = center(1,:);    % Keep 1st (best) found circle and radius.
However,
radius = radius(1,:);    % if more than 1 found then probably other
issues.
end

```

```

function [circ_mask] = CFB_Mask(img, center, radius)

```

```
%% creates circular mask given an image, center and radius of circ in
image
```

```
[y,x] = size(img);
[X,Y]=meshgrid(1:x,1:y);
circ_mask = sqrt((X-center(1)).^2+(Y-center(2)).^2)<=radius;
%must be same data type as img for math operations
circ_mask = uint16(circ_mask);
```

```
function [img_cropped, left_offset, top_offset] = CFB_Crop(img,
crop_size, center)
%% crops CFB image to new image centered on fiber bundle.
% Inputs:
% - img is original fiber bundle image.
% - size is new size specified as a single integer for a square or an
%   integer vector: [width,height]
% - center is center of fiber bundle (x,y)
% Outputs
% - img_cropped is the cropped img
% - offsets are how much as been removed from top and left side which
%   is
%   useful for updating circle center locations.

if length(crop_size)==1
    w = crop_size;
    h = crop_size;
else
    w = crop_size(1);
    h = crop_size(2);
end

top_offset = ceil(center(2)-h/2);
bottom_offset = floor(center(2)+h/2);
right_offset = floor(center(1)+w/2);
left_offset = ceil(center(1)-w/2);
img_cropped = img(top_offset:bottom_offset,left_offset:right_offset);
```

```
function [img_norm] = CFB_Norm(img,saturation_range,mask)
%% Outputs img with the ROI given by mask histogram normalized
% Inputs
% - img is img to be normalized
% - saturation_range=[low_in, high_in] Contrast limits for input
image,
%   specified as a two-element numeric vector with values between 0
and 1.
%   Values below low_in and above high_in are clipped; that is, values
%   below low_in map to low_out, and those above high_in map to
high_out.
%   If you specify an empty matrix ([]), imadjust uses the default
limits [0 1].
% - mask is the mask that provide the ROI of data points to use for
%   normalization in the image.
```

```
% Output
% - output is image normalized based on ROI and given saturation
limits

f = @(x) imadjust(x,saturation_range,[]);
img_norm = roifilt2(img,mask,f);
```

B.5.3. USAF Test Target Modulation Contrast Measurements

The final set of MATLAB code written for this project is designed to record modulation contrast of bar targets such as those on the 1951 USAF test target. The developed MATLAB function, 'CFB_BatchContrast.m' takes no input arguments. After initiating the function the user will be asked to select the directory containing the set of images to make contrast measurement on. Each image in the directory will be displayed to the user to draw a profile line across the bar targets. The intensity profile of the line will be displayed with the automatically detected minimums and maximums used in the contrast measurement detected. Each time the user draws a line on the image the user has the option to save the measurement, draw a new line or skip the image. The user is asked to draw the line twice on each image, once for tangential and once for sagittal bars. After all images in the folder have been measured the user will be asked where to save the results and with what file type.

This function will work on any set of USAF test target images and is not specific to CFB images. It has one supporting function that takes in the vector of minimum intensities and the vector of maximum intensities of the profile line and outputs the modulation contrast. The only files in the folder selected should be images. The main and supporting function follow:

```
%% Function to measure the modulation contrast of USAF test targets
function CFB_BatchContrast()
%Replace EXAMPLE with convenient default directory
dir_in = uigetdir('EXAMPLE...\USAF Images');
fileList = getAllFiles(dir_in);
n = length(fileList);
fileName = cell(n,1);
SagittalContrast = zeros(n,1);
S_min_1 = zeros(n,1);
S_max_1 = zeros(n,1);
S_min_2 = zeros(n,1);
```

```

S_max_2 = zeros(n,1);
S_min_3 = zeros(n,1);
TangentialContrast = zeros(n,1);
T_min_1 = zeros(n,1);
T_max_1 = zeros(n,1);
T_min_2 = zeros(n,1);
T_max_2 = zeros(n,1);
T_min_3 = zeros(n,1);
fprintf('\nDraw profile:\n\tLeft click for start\n\tRight click for
end\n')

for ii = 1:n
    img = imread(fileList{ii});
    sloc = strfind(fileList{ii}, '\');
    fileName{ii} = fileList{ii}(sloc(end)+1:end-4);
    [imgH,~] = size(img);
    imgM = 100*floor(900/imgH);
    fprintf(['\n' fileName{ii}])
    for jj = 1:2
        c = 0;
        repeat = 1;
        while(repeat)
            figure(10)
            imshow(img, [], 'InitialMagnification', imgM)
            if jj == 1
                fprintf('\n\tSagittal bars (radiating from center or
vertical bars if in center)')
                title([fileName{ii} ' SAGITTAL']);
            else
                fprintf('\n\tTangential bars')
                title([fileName{ii} ' TANGENTIAL']);
            end
            title(fileName{ii});
            prof = improfile; % draw line on image, save intensity
profile

                % find minimums (peaks of inverted function) with min
distance 1/4.5 of pixels
                [~,min_loc] = findpeaks(max(prof)-
prof, 'Minpeakdistance', length(prof)/4.5);
                while length(min_loc)~=3
                    fprintf('\n\tPlease choose new profile. 3 minimums not
found')
                    prof = improfile;
                    % find minimums (peaks of inverted function) with min
distance 1/4 of pixels
                    [~,min_loc] = findpeaks(max(prof)-
prof, 'Minpeakdistance', length(prof)/4.5);
                end

                [~,max_loc1] =
findpeaks(prof(min_loc(1):min_loc(2)), 'SortStr', 'descend', 'NPeaks', 1);
                [~,max_loc2] =
findpeaks(prof(min_loc(2):min_loc(3)), 'SortStr', 'descend', 'NPeaks', 1);
                max_loc = [min_loc(1)+max_loc1-1, min_loc(2)+max_loc2-1];

```

```

        min_val = prof(min_loc);
        max_val = prof(max_loc);

        % repeat for maximums between the mins also with 1/4
distance.
        % use to calc (Imax-Imin)/(Imax+Imin)
        %make batch processing routine to have user take data for
every image and
        %save results.
        hold off
        figure(11)
        plot(prof)
        hold on
        plot(max_loc,max_val,'o')
        plot(min_loc,min_val,'*')
        c = CFB_Contrast(min_val,max_val);
        hold off
        str = sprintf('Measured modulation contrast is
%3.1f%%',c*100);
        choice = questdlg(str, 'Repeat Measurement?',...
            'Repeat','Save and continue','Set c=0 and
continue','Repeat');
        switch choice
            case 'Repeat'
                repeat=1;
                fprintf('\n\tRepeat Measurement');
            case 'Save and continue'
                repeat=0;
            case 'Set c=0 and continue'
                repeat=0;
                c = 0;
        end
        if jj==1
            SagittalContrast(ii)=c;
            S_min_1(ii) = min_val(1);
            S_max_1(ii) = max_val(1);
            S_min_2(ii) = min_val(2);
            S_max_2(ii) = max_val(2);
            S_min_3(ii) = min_val(3);
        else
            TangentialContrast(ii)=c;
            T_min_1(ii) = min_val(1);
            T_max_1(ii) = max_val(1);
            T_min_2(ii) = min_val(2);
            T_max_2(ii) = max_val(2);
            T_min_3(ii) = min_val(3);
        end
    end
end
end
end

results = table(fileName,SagittalContrast,S_min_1,S_max_1,S_min_2,...
S_max_2,S_min_3,TangentialContrast,T_min_1,T_max_1,T_min_2,T_max_2,T_m
in_3);

```



```

[filename, pathname] =
uiputfile({'*.txt'; '*.dat'; '*.mat'; '*.xlsx'; '*.xls'; '*.xls'; '*.xls'; '*.xls'}, 'S
ave as');
writetable(results, [pathname filename])
fprintf('\nFile Saved\n\n')
end

function c = CFB_Contrast(Imin, Imax)
%calculates modulation contrast Imax-min / Imax+Imin
c = (max(Imax) - min(Imin)) / (max(Imax) + min(Imin));

```

APPENDIX C: DOUBLE REFLECTION COVER PLATE

This appendix includes a technical write up for the modeled single lens system for forward viewing navigation and scanning side-viewing OCT. The lens design prescription is reported and a modified version of the previously reported Gaussian beam propagation model is included. The Gaussian beam model is used to increase illumination fiber output rather than for OCT imaging.

C.1. Detailed Lens overview

The following report is written following SPIE guidelines for future submission as a technical paper or conference proceedings.

Single Lens System for Forward Viewing Navigation and Scanning Side-Viewing OCT

Tyler H. Tate^a, Davis McGregor^b, Jennifer Barton^{a,c}

^aCollege of Optical Sciences, University of Arizona, 1630 E University Blvd, Tucson, AZ 85721

^bAerospace and Mechanical Engineering, 1130 N. Mountain Ave, Tucson, AZ 85721

^cBiomedical Engineering, University of Arizona 1657 E Helen Street, Tucson, AZ 85721

Abstract

A technical write-up on the optical design for dual modality endoscopes based on piezo scanning fiber technology is presented including novel design approaches. In particular, optical designs for combining forward-viewing navigation and side viewing OCT are considered with potential application of navigating body lumens such as the fallopian tube, biliary ducts and cardiovascular system. Advantages and disadvantages of the technology compared to coherent imaging bundles are considered. Design considerations in choice of fiber for the scanning system are explored and a new idea to increase the divergence angle of the scanning fiber for improved system performance is presented. A novel cover plate design is presented that allows for side-viewing scanning OCT capable of acquiring cross-sectional images of the tubal lumen. Finally, an example optical design using both the increased divergence angle technique and novel cover plate is presented.

1. Introduction

Forward-viewing endoscopes utilizing piezo scanning fiber (SF) endoscope technology was developed⁸¹. SF is an alternate method of image formation compared to the use of an imaging coherent fiber bundle (CFB) or a miniature detector in the endoscope tip. In one implementation, a single mode fiber is coaxial centered inside a quartered piezo tube. The fiber is fixed to one end

of the tube with a small cantilevered length of fiber protruding (Figure 11). Electrically driving the piezo tube at the mechanical resonance frequency of the fiber causes the cantilevered fiber tip to oscillate. By driving the piezo tube in two orthogonal axes at resonance while controlling the phase difference and amplitude it is possible to scan the fiber tip in a predetermined pattern. A spiral scan is typical. The output of the fiber can be considered a point-source with Gaussian beam output and rapidly scanning the fiber in a spiral pattern effectively creates a disc of point sources. An optical illumination system can be designed to image the scanning fiber onto the sample. Calibration allows *a priori* knowledge of the illumination scanning location as a function of time. High temporal recording of the reflectance or fluorescence light returning from the sample allows the intensity of the image to be known as a function of time. Image reconstruction is performed by correlating the known scan locations and detection intensities as a function of time during each scan.

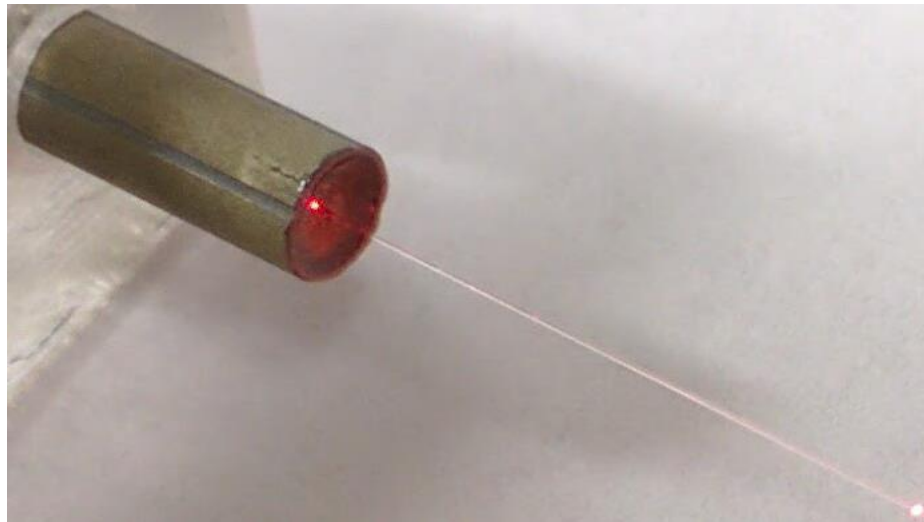


Figure 11: A prototype setup of a quartered piezo tube (QPT) with a cantilevered length of fiber (CL) fixed to one end with adhesive (A) and protruding out. The other end of the QPT is fixed to an acrylic mounting block. A red diode laser is coupled into the fiber.

For endoscopes with diameter smaller than a few millimeters a miniature detector is too large. SF or CFB are the two primary image formation technologies with advantages and disadvantages compared in Table 2. CFB endoscopes can be built smaller with available CFB's as small as 1600

elements (pixels) and just 200-micron outer diameter. Depending on configuration at least one illumination fiber with diameter of 50-125 microns may also be necessary. In comparison the smallest demonstrated SF endoscope uses a piezo tube of 450-micron outer diameter.⁸¹ The mounting of the tube requires some additional space and reflectance or fluorescence configurations typically use a ring of collection fibers around the outside of the lens system. It may be possible to use a dual clad fiber for both illumination and light collection, but it is unclear if sufficient light would be collected in practice. Thus SF endoscopes smaller than 1 mm total outer diameter may be possible, but have yet to be demonstrated. A SF endoscope with piezo tube of equivalent diameter to a CFB can have 2-4 times the effective pixel density depending on configuration and scan speed. The scanning fiber does not suffer from the honeycomb artifact of using a CFB as a relay element. The increased pixel density and lack of honeycomb artifact come at the expense of significantly more complicated image acquisition and processing. A major potential advantage of SF technology driving this report is the possibility to use the SF for simultaneous dual-modality imaging with scanning OCT that is not practical in a small diameter CFB endoscope, since practical CFBs do not preserve phase information (typically individual cores are multimode and core-to-core coupling occurs).

SF endoscopes have been built for forward viewing using visible light⁸¹ or OCT^{76,83}. Forward viewing OCT requires a very high speed OCT system in order to create 3D volume images with good sampling density in real-time. From a practical stand-point, a clinically useful method to display video rate 3D volumes remains a challenge. For certain tubal endoscopic applications, it is more useful to have circumferentially scanning side viewing OCT to create a 2D cross-sectional image of the tubal wall. A forward-viewing reflectance or fluorescence imaging channel is more practical for navigation. Using SF technology, it is possible to design a system that does both side-viewing OCT with scanning and forward viewing navigation.

Design Feature	CFB	SF
Single-channel dual modality imaging	No	Yes
OCT scanning	No	Yes
UV material transmission challenges	Imaging	Illumination
Effective Pixel Density (pixels/mm ²) ⁸¹	~113k	~345k
Minimum endoscope diameter	~500 μ m	~1 mm
Imaging honeycomb effect	Yes	No
Minimum bend radius of optical fibers	15-20 mm	~2-3 mm
Image processing and reconstruction	Moderate	Complex

Table 2: Table comparing design features for dual modality endoscopes based on a CFB and SF design. For UV fluorescence imaging both UV excitation and emission must be transmitted through the system, limiting material choices for the lens system in either configuration. The minimum bend radius of the flexible section of an endoscope depends on the combined characteristics of all materials used in construction. The smaller fibers used in a SF endoscope allow a reduced minimum system bend radius without fiber damage. The rigid tip length in the SF endoscope will typically need to be longer to accommodate the piezo tube and cantilevered fiber.

Most scanning, side-viewing OCT systems rely on a single mode optical fiber with a stationary optical axis and a planar reflecting element. The reflection may be via a mirror, prism or angle polished element. The reflective surface rotates around the optical axis to scan the beam. In an SF design the output optical axis of the OCT beam can be scanned in a circle around the lens system optical axis. Since the optical axis is no longer coaxial with the lens system a rotating planar mirror is no longer appropriate for beam turning. In this study the OCT scan is set to a specific displacement radius of the tip of the cantilevered fiber. The circular scan of the source at the given displacement angle is turned by a rotational symmetric double reflection from a custom cover plate. The result is a circumferential cross-sectional scan in the tissue. In this study the maximal displacement of the fiber is used for the OCT scan.

The forward-viewing channel can be separated from the OCT scan spatially. Since the OCT beam is the maximum displacement, the double reflecting surfaces can be annular such that the forward viewing channel operates at a smaller displacement and transmits through the center of the annuluses. A proof-of-concept optical design for this system is shown in Figure 2.

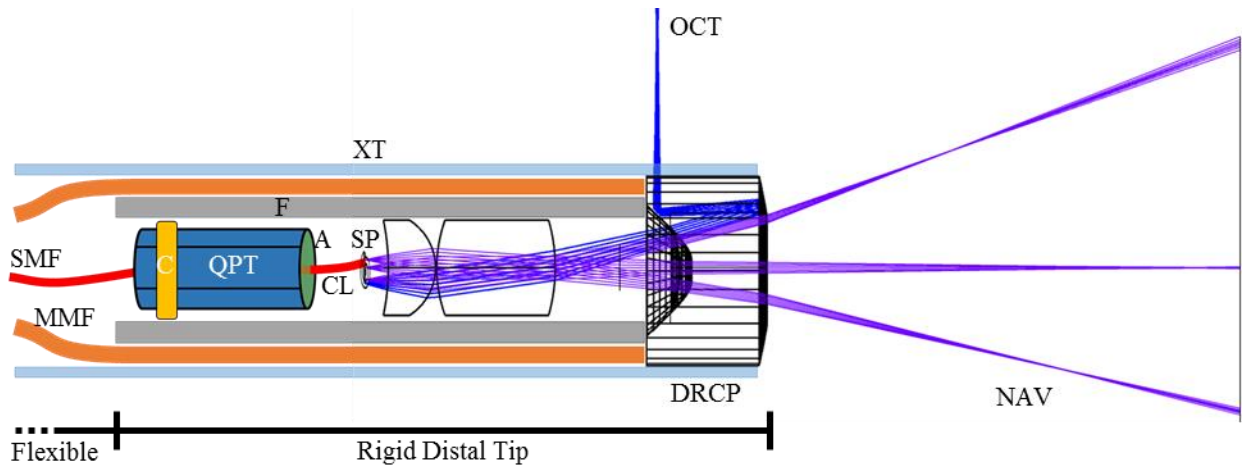


Figure 12: Sample design of a dual modality SF endoscope with side-viewing OCT and forward viewing navigation (NAV). The design shows the single-mode fiber (SMF) passing through the quartered piezo tube (QPT). It is adhered (A) to the tube with cantilevered length (CL) protruding to produce the scan pattern (SP). The QPT is attached to the rigid ferrule (F) with a mounting collar (C). The lenses are also held in by the ferrule. A ring of high NA multimode fibers MMF surround the ferrule. The outer most layer is IR transparent extruded tubing (XT). The double reflection cover plate (DRCP) at the distal end separate the two image modalities spatially. Design is not to scale.

2. Design

A complete conceptual design of a dual modality SF endoscope for side-scanning OCT and forward viewing navigation is presented. This includes a detailed optical design of the endoscope tip and a sample system design. The focus of the paper is the choice of scanning fiber and lens design including the novel double reflection cover plate (DRCP) that spatially separates the two channels. A sample of the layout of an endoscope distal tip with a DRCP is shown in Figure 12. For the prototype design, the forward viewing channel is monochromatic with 406 nm illumination suitable for reflectance imaging and excitation of intrinsic fluorophores. A sample system diagram is shown in Figure 13, assuming a tri-color blue, green, and red illumination system was implemented. The complete system, mechanical and optical design for a dual modality endoscope is multi-faceted and specific design choices depend on the application. This section focuses on the optical design considerations and characteristics including a DRCP.

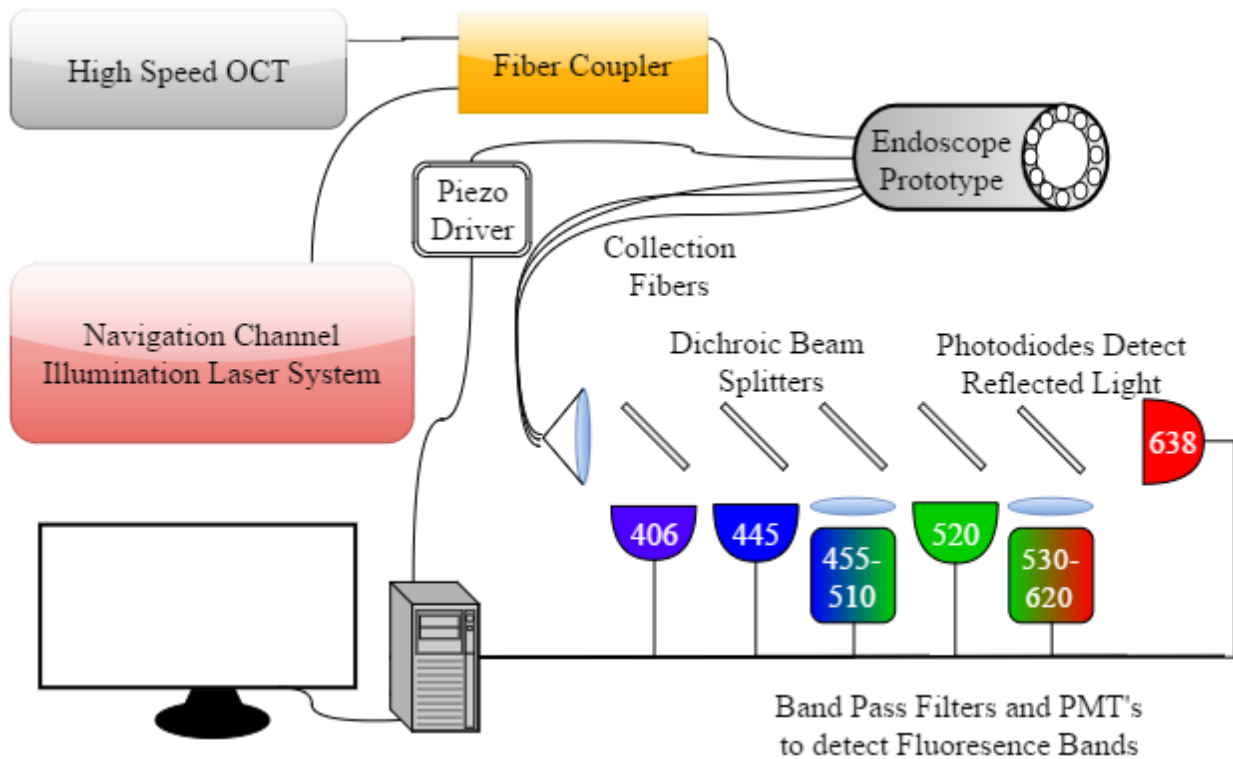


Figure 13: Sample system diagram for a dual modality scanning fiber endoscope. The illumination for the navigational channel and OCT must be combined using a fiber coupler into a single fiber for scanning. In this example the detection system for the navigation channel includes multiple photodiodes and photomultiplier tubes (PMT) to simultaneously detect reflected light and fluorescence from multiple illumination wavelengths. This can be configured for white-light imaging, fluorescence imaging or both as necessary for the application.

2.1. Illumination Wavelengths

The choice of illumination wavelengths will impact optical performance, design and material choices. OCT requires a single-mode (SM) fiber operating in the near IR with typical central wavelength around 890 nm, 930 nm, 1060 nm or 1300 nm. Longer wavelengths tend to have deeper penetration in tissue, but worse imaging resolution. The DRCP material is an acrylic polymer suitable for diamond turning fabrication. The specific polymer will affect transmission range, but generally transmission efficiency for acrylic has drop outs above 1200 nm. For the proof of concept design a central wavelength of 1000 nm is used. Slight modifications to the design can be made to accommodate the specific OCT system used.

The navigation channel will be used for reflectance or fluorescence imaging. For reflectance imaging a single visible laser can be used for monochromatic imaging or a combination of red, green and blue lasers can be used for white-light equivalent imaging. For fluorescence imaging blue or near UV sources are necessary. The broader the wavelength range the more chromatic considerations are necessary for the optical design and the choice of scanning optical fiber. For this design a single mode fiber coupled 406 nm fiber diode laser (e.g. Thorlabs LP406-SF20) is assumed to be the source. Reflected light can be used to generate a monochromatic image and the wavelength is short enough to excite many endogenous fluorophores. Simultaneous collection of reflected light and fluorescence emission could be used to create a reflectance image with overlaid fluorescence signals. Additional laser wavelengths could be added in the future for color imaging or multispectral fluorescence imaging (Figure 13).

2.2. Scanning Fiber

Fundamentally the scanning fiber is the light source in an illumination system. Before designing the lens system to image the light source into the sample space it is critical to know the light source characteristics. In particular the numerical aperture (NA) of the fiber and the scanning geometry will determine the achievable limits to the resolution and FFOV of the illumination system.

A SM fiber is necessary for the interference in the OCT system, and SM fibers naturally provide even illumination in the navigation channel. SM fibers are only designed to operate over wavelength ranges of a few hundred nanometers. The V number is a dimensional parameter associated with step index fibers defined as:

$$V = \frac{2\pi}{\lambda} * a * NA(\lambda) = \frac{2\pi}{\lambda} * a * \sqrt{n_{core}^2(\lambda) - n_{cladding}^2(\lambda)}$$

In this equation a is the radius of fiber, NA is the numerical aperture, n_{core} is the index of refraction of the fiber core and $n_{cladding}$ is the index of refraction of the fiber cladding.

Emphasized here is that the indices of refraction and thus NA are wavelength dependent. Fibers only support a single mode of transmission below $V \approx 2.405$. for larger V numbers the number of supported modes is:

$$\text{Number of Modes} \approx \frac{V^2}{2}$$

This becomes relevant if a SM fiber designed for 1 micron wavelengths is also used with 406 nm wavelengths. With the rough assumptions that the V number for a SM fiber is 2 for 1 micron wavelengths and the NA is constant than the V number will be around 4.9 for 406 nm light and thus allow approximately 12 modes of propagation. The output power distribution will be a superposition of propagation modes rather than a disc with smooth Gaussian power distribution. Additionally the mode field diameter (MFD) is twice the beam waist, ω_0 , and can be approximated from the V number using¹³⁶:

$$\frac{\omega_0}{a} \approx 0.65 + \frac{1.691}{V^{3/2}} + \frac{2.879}{V^6}$$

Approximating the output beam of a SM fiber can reasonably be done as a Gaussian beam with beam waist ω_0 at the fiber face. All other parameters of the Gaussian beam including the divergence angle which is equivalent to the NA in the far-field can be derived from the beam waist size. When using a SM fiber with shorter wavelengths than it is designed for it becomes multimode and has a different mode field diameter (and thus a different NA). For the navigation channel the practical impact of these effects should be examined experimentally to determine if they lead to an unacceptable degradation of illumination beam quality and thus image quality. If the negative effects are minimal for the forward viewing channel then the simplest solution for a dual modality system is to use a SM fiber designed for the wavelength ranges of the OCT system.

Alternative fiber choices may include dual-clad fibers or multi-core fibers. Dual clad fibers have a SM core to transmit the OCT. There are then two layers of cladding and the inner cladding may be suitable for the navigation channel illumination. It will still be multimode, but may have

many modes and when used in combination with a mode scrambler provide a reasonably even illumination pattern. The inner cladding may also be able to be designed with a higher NA than the SM core allowing for improved resolution in tissue space for the forward viewing channel. A multi-core fiber could also be custom designed in which multiple SM cores are placed in the same fiber. Each core would be SM over a limited wavelength range and in combination could cover any desirably range of the near UV, visible and near IR spectrum. The total size of a dual-clad or multi-core fiber may be larger than what is available as a standard SM fiber. The increased mass will reduce the resonant scanning frequency.

The scanning geometry and maximum deflection of the tip of the fiber relative to the optical axis the lens system defines the physical extent of the illumination source. The maximum deflection depends on the material properties and physical dimension of the piezo tube and the fiber as well as the cantilevered length of the fiber. The equations for determining the resonance frequency of the fiber have eigenvalue solutions of increasing frequency. The maximum tip deflection is achieved with the lowest resonance frequency. Experimentally, a 17 mm length of cantilevered 780HP fiber has been verified to have a maximum tip deflection of $\pm 200 \mu\text{m}$ with a RMS driving voltage of 20 V at the lowest resonance frequency. Depending on the specific configuration of the piezo tube and fiber the tip deflection will change. This study assumes $\pm 200 \mu\text{m}$ as a reasonable initial design values. Increasing the maximum tip deflection increases the total number of effective pixels and thus can improve the resolution or FFOV.

2.3. Increasing the Numerical Aperture

The lens design initially assumes a SM fiber designed for 1-micron light with an NA of 0.127 (MFD=5). SM fibers operating near 1 micron typically have NA values between 0.1 and 0.2 so these are considered reasonable, but conservative estimates. For this study the same SM fiber when used with 406 nm light is assumed to have a reduced NA of 0.086 (MFD=3). This number

will need to be experimentally verified, but is considered a reasonable approximation. The optical design for both the OCT and navigation channel would benefit from increased fiber NA.

One method of increasing NA coming out of the fiber is to fusion splice small sections of large core multimode fiber followed by gradient index (GRIN) fiber onto the end of the scanning fiber (Figure 14). The lengths are short enough and the material characteristics and physical dimensions are similar enough to standard SM fibers that the resonant properties of the fiber are not expected to be degraded. The effect is a very short relay system that reimages the beam waist to a smaller size just outside of the spliced GRIN fiber. The smaller beam waist corresponds to an increased divergence angle after the focal spot. Using this technique, the output NA of the fusion spliced assembly can be increased to 0.27 for the 1-micron light and 0.18 for the 406 nm light. The technique is ideal for single mode fibers and dual clad fibers as the optical axis and mechanical axis are coaxial. Multicore fibers with each core having an independent optical axis slightly displaced from the optical axis of the GRIN fiber may have minor angular divergence for light from each core at the output.

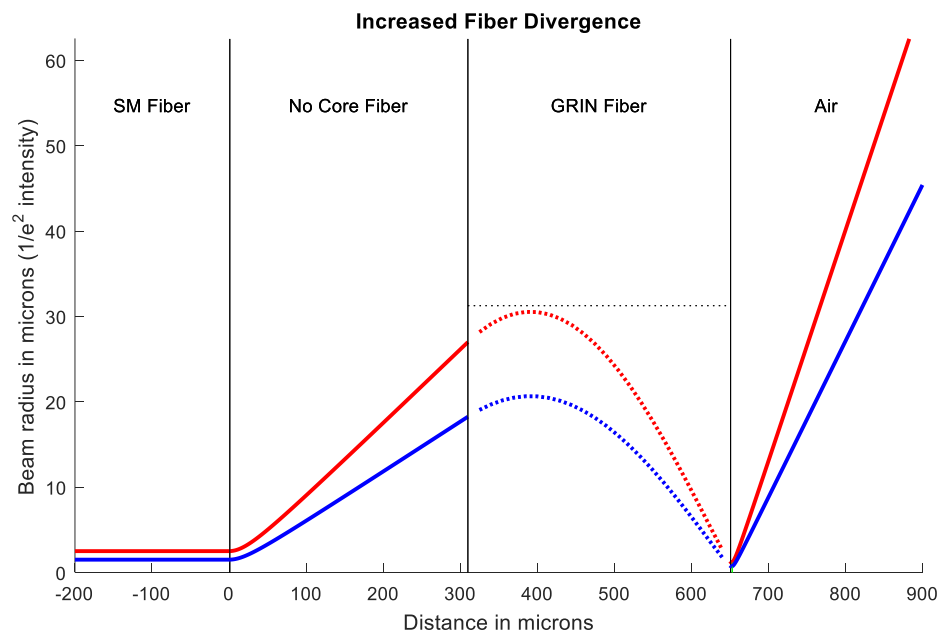


Figure 14: Plot of the beam waist ($1/e^2$ intensity) vs distance from the output of the SM fiber. A GRIN fiber is used to increase the divergence angle. The red line represents the 1-micron beam

with initial MFD of 5 microns and the blue line represents the 406-nm beam with initial MFD of 3 microns. The SM fiber, no core fiber and GRIN fiber are all assumed to have outer diameter of 125 microns and to be fusion spliced together. The horizontal dashed line in the GRIN fiber represents the maximum usable aperture.

The majority of the source properties critical to the lens design have now been discussed. One final consideration is that the output optical axis of the oscillating fiber will tilt with respect to the optical axis of the lens system as a function of displacement. For a cantilevered fiber length of 17 mm a conservative estimate based on early experimental results with the setup shown in Figure 11 suggest that the tangent line from the tip of the fiber would cross the axis 10 mm behind the fiber tip. Thus the maximally divergent tangent line creates a triangle with a 10 mm base and 200-micron height. This corresponds to a divergence angle of 1.15 degrees. For the proof of concept endoscope this value is considered negligible. Thus the complete assumptions for the light source are a 200-micron fiber tip deflection with telecentric output of 0.27 NA at 1 micron and 0.18 NA at 406 nm

2.4. Lens Design

The goal of the design is to provide forward viewing navigation with as large of a FFOV as possible with simultaneous side viewing OCT. For applications like transvaginal ovarian cancer screening and biliary duct imaging the endoscope outer diameter is ideally 3.3 mm or less. Due to the small size and limited alignment compensation of endoscopes, lens designs with few and simple elements are preferred. For this design two glass lenses with spherical surfaces are used in addition to the custom DRCP.

Due to the significant difference in wavelength between the two modalities the lens design functions differently for each wavelength. The first two lenses provide the focal power for the 406 nm light. If the cover plate had flat surfaces the 406 nm light would be focused just outside the cover plate front of the endoscope with nearly 0.4 NA and 17.5 degree FFOV. The first (proximal) surface of the cover plate has negative power to increase the working distance and

field of view at the expense of reducing the NA. The rear (distal) surface of the cover plate is flat and transmissive over the region that the forward viewing rays transmit.

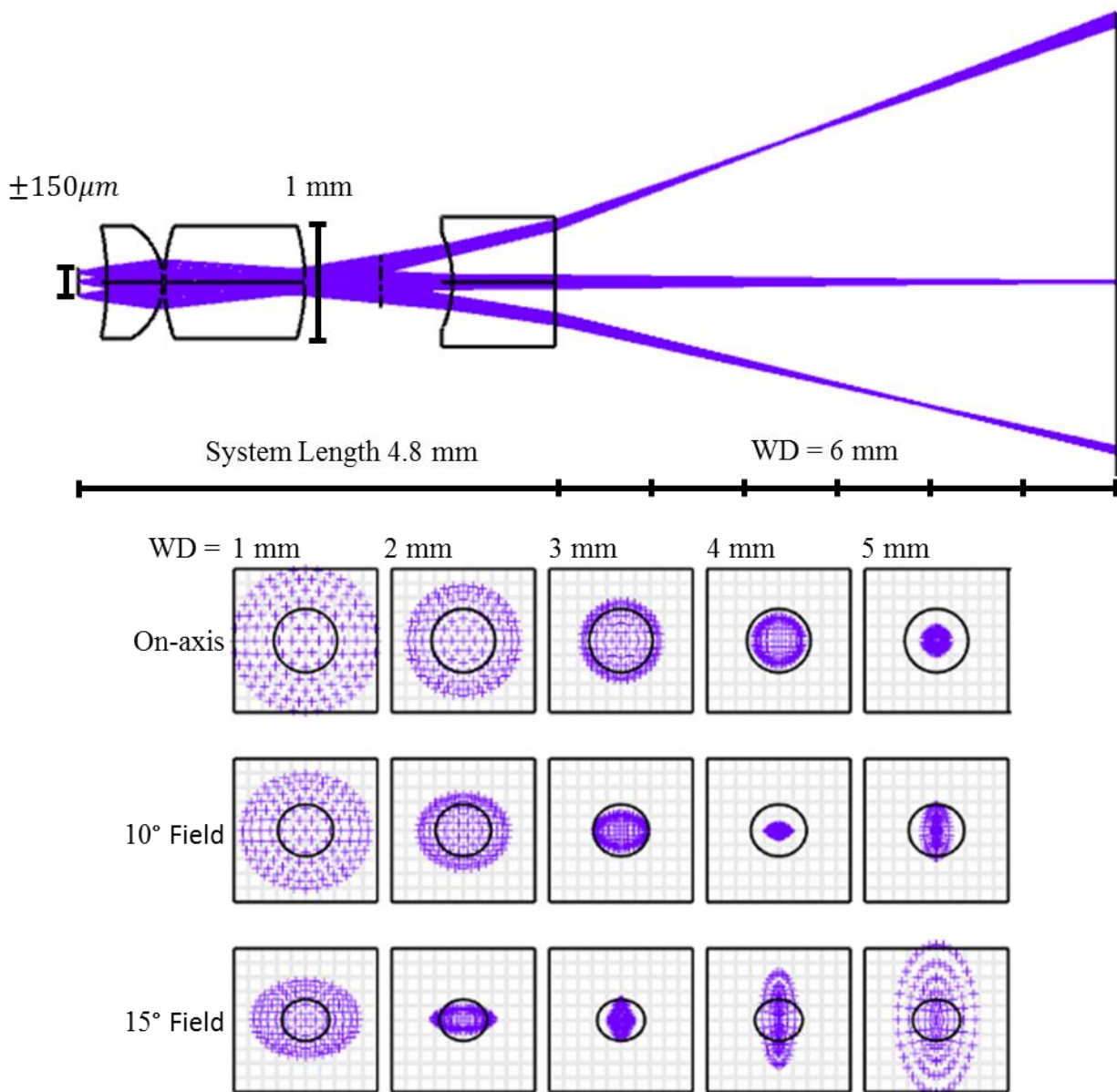


Figure 15: Top - Lens system shown in forward viewing navigation configuration. Only the portion of the cover plate is shown that interacts with the forward viewing rays. Bottom - Spot diagrams for each field in 1 mm steps from 1 mm to 5 mm working distances. Each box has 100-micron side lengths and airy disks are shown in each box with diameter 44.32 microns.

The design from the perspective of the forward-viewing channel along with spot diagrams in one millimeter steps for the first 5 millimeters of working distance is shown in Figure 15. The NA is approximately 0.01 corresponding to an airy disk diameter of 44 microns. The FFOV is 30 degrees. The minimal spot size is at progressively shorter working distances as the field angle increases. For illumination inside of a tube this is an advantage. The tubal walls will have higher resolution at shorter working distances while the tubal opening in front of the endoscope will have higher resolution at longer working distances. As an illumination system the working distance can be considered any distance from which sufficient reflected or fluorescence light is collected to generate an image. The illumination beam will have angular resolution with best spatial resolution at the minimum spot diameters. The low NA system will have reasonably consistent performance over a long working distance.

The field of view is limited by the spatial separation of the navigation and OCT beams on the second surface of the cover plate. An annular region is used to reflect the OCT beam which limits the range of deflection usable for navigation to 75% of maximum. In terms of area, only 56% of source extent is used leading to significant loss of potential pixels.

For OCT only the largest field angle beam originating from the maximal fiber tip deviation is considered and it takes a different path through the lenses system. The light passes through the first two lenses and the negative power central region of the first surface of the cover plate similar to the navigation channel. The significantly longer wavelength

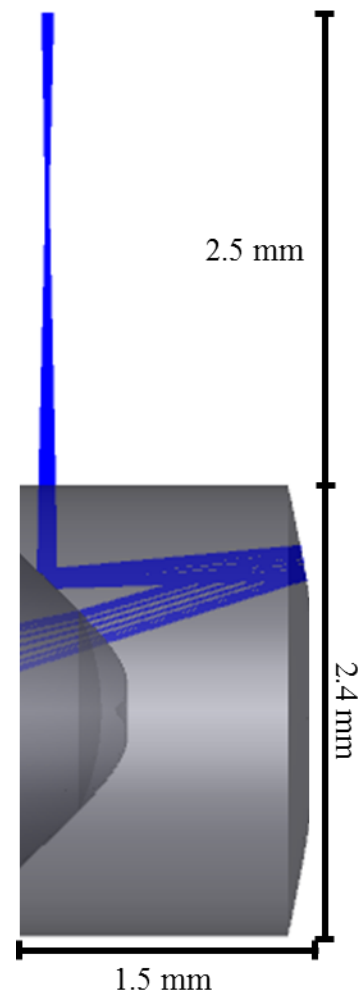


Figure 16: OCT light path through double reflection cover plate.

experiences less refractive power at each surface and the beam is approximately collimated after entering the cover plate.

Rather than pass through the flat transmissive central region on the second surface of the cover plate the OCT beam reflects from an annular region of the cover plate with an aspheric profile. The light makes a second pass through the cover plate and a second reflection from another reflective annular region of the cover plate with an aspheric profile on the first surface (Figure 16). The first reflection primarily adds positive focal power to the beam along with some deviation. The second reflection primarily deviates the beam for side viewing and adds some negative power to extend the working distance and depth of focus.

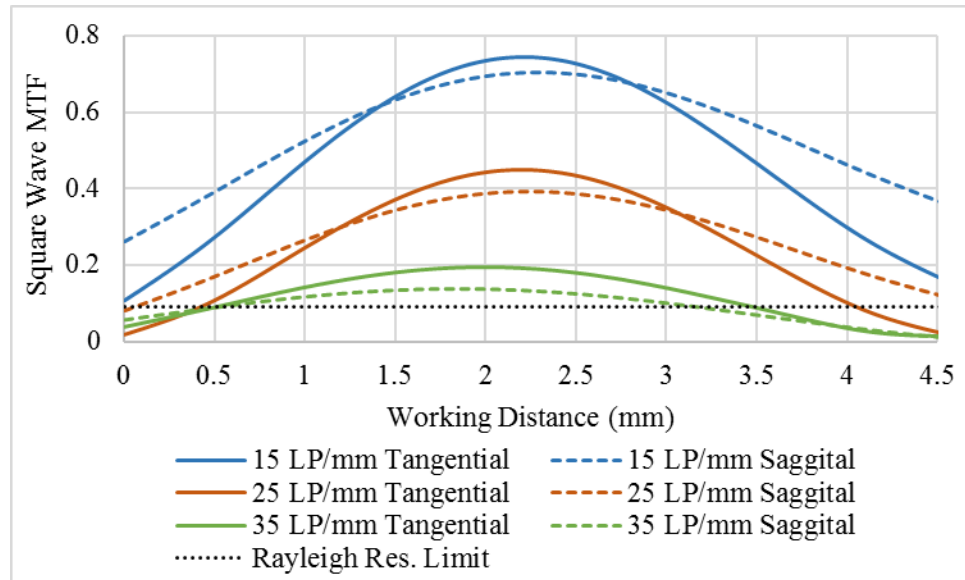


Figure 17: Graph showing the MTF contrast of a square wave target as a function of working distance for the OCT system. Best focus is generally between 1.5 and 2.5 mm working distances. Lower frequency square wave targets have higher contrast and large depth of fields as expected.

The OCT beam is designed for best focus 1.5-2.5 mm outside the cover plate as shown in Figure 16. A square wave target with 25 LP/mm has contrast above the Rayleigh limit (9%) for a range of working distances from 0.5 mm to 4 mm. In this implementation of the design the cover plate is 2.4 mm leading to best focus in an annular region of 5.4 to 7.4 mm diameter. For reference, bile duct diameter is 4.1 mm in normal patients and can increase to over 11 mm in

abnormal conditions such as gallstones, pancreatitis or tumor development¹³⁷. With the goal of placing the OCT focus inside of the tissue wall this design may be suitable for this application. Further increases to working distance with the same sized DRCP are challenging and result in a loss of resolution. The DRCP could be scaled up or down depending on application. Diamond turning can fabricate 1 mm thick by 1 mm diameter elements relatively easily. Smaller sizes may pose fabrication and coating challenges.

2.5. Resolution Considerations

Resolution of a scanning fiber endoscope depends on scanning geometry, sample acquisition rate and lens system. The scanning geometry and sample acquisition rate can be adjusted after construction allowing an adjustable trade-off between sampling density and scanning speed. The best achievable resolution is fundamentally limited by the illumination lens system. The lens system is imaging the effective point source of the scanning fiber onto the sample. Assuming a diffraction limited imaging system the Rayleigh resolution, Δx , is half the airy disk diameter given by:

$$\Delta x = \frac{D_{airy}}{2} = \frac{1.22\lambda}{NA}$$

The theoretical maximum number of resolvable points is thus equivalent to the number of non-overlapping circles with diameter Δx that have centers inside the illumination disc used to create the image with radius R_{img} . This is a classic circle packing problem and the solution is best approximated with a computational algorithm as there is no explicit formula¹³⁸. Free online computation tools such as WolframAlpha can be used to quickly make the calculation. For the system described the beam is diffraction limited at all field angles at a working distance of 3.8 mm with $\Delta x = 19.05 \mu m$ and $R_{img} = 2.032 mm$. Given these parameters approximately 41k resolvable points are possible. The forward viewing channel only uses ± 150 micron tip deflection of the fiber which corresponds to a scanned area of $0.071 mm^2$. Thus 41k resolvable

points corresponds to a pixel density of 580k pixels/mm² which is higher than estimated in table 2. For comparison, a CFB with 3.1-micron core-to-core separation and a 325-micron diameter image circle (Fujikura FIGH-10-350S) has 10,000 pixels which also corresponds to a slightly higher number than estimated in table 2 with 120,000 pixels/mm². An improvement of 3-5 times the pixel density when compared to a CFB is expected. Some degradation will occur in the scanning fiber resolution due to scanning artifacts and digital resampling. However, similar image quality degradation is present when using a CFB as the honeycomb structure must be reimaged onto a digital detector on the proximal side of the endoscope.

For Nyquist sampling the system must sample with $\Delta x/2$ spacing. The sampling for a scanning fiber endoscope typically occurs in a spiral pattern and the collected samples must be digitally resampled for display on a Cartesian pixel grid. The final resolution will be determined by the sampling frequency, scan artifacts, optical aberrations and digital resampling efficiency.

The approximate number of sample points per scan for Nyquist sampling can be determined from the scanning geometry. Assuming negligible distortion and other aberrations a spiral scan of the fiber tip will image to a spiral scan in sample space. The parameterized Cartesian coordinates for the sample space spiral scan are given as a function of time by:

$$x(t) = R(t) * \cos(t)$$

$$y(t) = R(t) * \sin(t)$$

Where t is a time vector for each image acquisition from time zero to total image acquisition time T and sampling rate $1/\Delta t$. The radial location of the point is given by $R(t)$ as a function of time with a maximum value equal to R_{img} . For simplicity this derivation assumes a simple Archimedean spiral in which $R(t)$ is a constant function of time (linear). Thus the branches (rings) of the spiral have constant separation distance.

Nyquist sampling requires at least two samples per Δx . The total number of samples, N_{Total} can be determined as the product of necessary number of samples per spiral branch, N_{θ} , and the

necessary number of spiral branches, N_r . With a constant time between samples, Δt , the number of samples per branch is constant. In other words, the angular separation between each sample point with respect to the origin is constant, but since the radial distance between each sample point is increasing the distance between consecutive sample points increases over time. The sampling density is thus foveated with Nyquist sampling at the edge of the image requiring oversampling the center of the image. Both N_r and N_θ can be calculated using Δx and R_{img} :

$$N_\theta = \frac{\pi}{\sin^{-1}\left(\frac{\Delta x}{2R_{img}}\right)}$$

$$N_r = \frac{2R_{img}}{\Delta x}$$

$$N_{Total} = N_r * N_\theta$$

Using the values for the resolution and image size above this system approximately requires $N_r = 213$ and $N_\theta = 670$ for Nyquist sampling of the full image. Thus 285,420 samples must be acquired during the full scan. A sample acquisition spiral with $N_r = 21$ and $N_\theta = 67$ is shown in Figure 18: Sample illumination spiral scan with 21 branches. Red circles represent acquisition sample points with 67 samples per branch. The radius of the red circles is equal to the airy disk radius of 19.05 microns. The outer black circle represents the maximum image size of radius 2.032 mm at a working distant of 3.8 mm. Axes have units of microns. Figure 18.

The time required for each branch of the spiral will be determined by the resonance frequency ω_0 . The interval between samples and total image acquisition time can be determined from ω_0 :

$$\Delta t = \frac{1}{N_\theta \omega_0}$$

$$T = \Delta t * N_{Total} = \frac{N_{Total}}{N_\theta \omega_0} = \frac{N_r}{\omega_0}$$

For the forward viewing channel to achieve a 24 Hz video frame rate the resonance frequency must be 5.1 kHz assuming continuous acquisition. In reality, maintaining a highly repeatable scan

during continuous scanning may not be possible. Additional time may need to be added after each spiral to reset the fiber velocity to zero using active dampening and passive decay. This can add as much as 40% additional acquisition time to each image and thus would require a resonance frequency of 7.1 KHz in order to maintain Nyquist sampling for 24 Hz video rate imaging. Depending on the application it may not be necessary to achieve Nyquist sampling of the full image in which case the number of samples may be reduced in exchange for increased frame rate. Ultimately the samples will be acquired in polar coordinates and will need to be resampled onto a Cartesian grid of pixels for display.

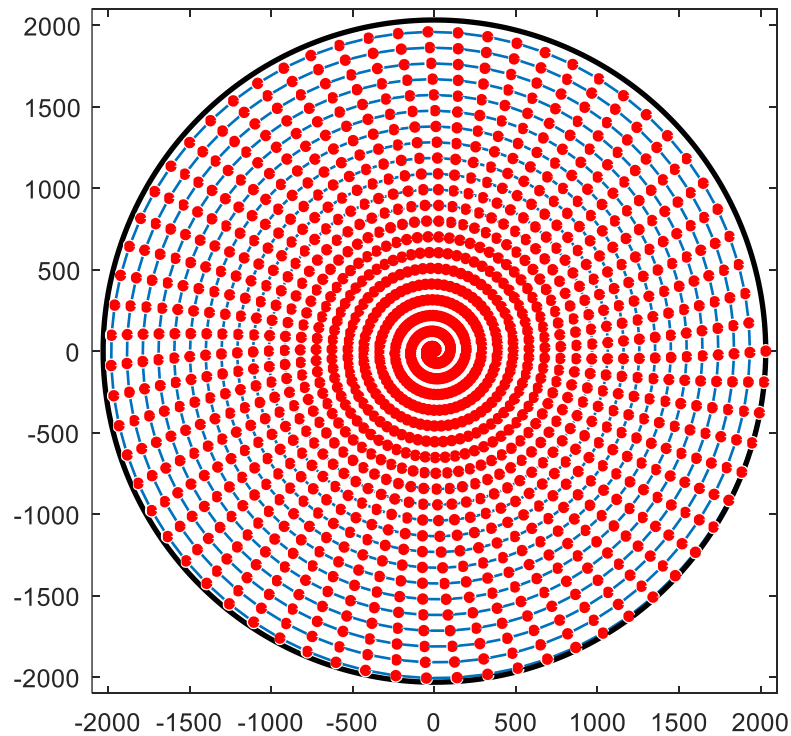


Figure 18: Sample illumination spiral scan with 21 branches. Red circles represent acquisition sample points with 67 samples per branch. The radius of the red circles is equal to the airy disk radius of 19.05 microns. The outer black circle represents the maximum image size of radius 2.032 mm at a working distant of 3.8 mm. Axes have units of microns.

3. Concluding remarks

The optical designs present here may have significant utility for future tubal endoscopic applications such as in the fallopian tube, bile ducts and cardiovascular system. Experimental verification remains necessary to validate some of the theoretical work presented here. The properties of SM designed for OCT when used out of specification for visible wavelengths needs to be evaluated. Fusion spliced no core and GRIN fiber has been successfully used for OCT focusing optics in the past^{71,85,139}, but the utility for increasing SF divergence must be validated. GRIN fibers are sometimes used for mode scrambling of multimode fibers so the use of a GRIN element for divergence increase will alter the illumination quality of the visible beams in the OCT SM fiber. Most importantly the fabrication, coating and testing the DRCP remains to be done.

The DRCP is designed to be fabricated from acrylic using diamond turning in order to allow different annular surface profiles. The physical limits of the tool and the realistic slope and depth of the negative surfaces needs further evaluation. A larger version should be designed and fabricated for benchtop proof-of-concept testing. The design offers a promising approach to using SF technology for side-viewing OCT. One limitation of the current design is the limited FFOV of the forward channel due to the spatial separation of the beam paths.

An alternate approach may be spectral separation of the near IR OCT beam from the forward-viewing visible channel. The first reflective surface could use a dichroic coating to reflect the OCT beam and transmit the navigational beam. This would potentially allow for the navigational channel to use the full spatial extent of the optical element increasing the FFOV. The approach may also allow for an overall size reduction necessary for endoscopes with outer diameter near of approximately 1 mm.

The DRCP does adds challenges to the light collection geometry that need further work to address. Placing the collection fibers behind the cover plate may allow back reflections from the proximal face of the cover plate to enter the collection fibers. Additionally, the annular mirrored

surface of the cover plate will partially obscure the collection cone of each fiber. An alternative is to place the ring of collection fibers outside the DRCP with the proximal faces of the DRCP and collection fibers at the proximal end of the endoscope tip. This approach solves the aforementioned issues for the forward viewing channel, but requires the OCT beam to pass through the ring of collection fibers. The collection fiber materials could be chosen to be IR transmissive, but the ring of fibers will still induce aberrations and back reflections into the OCT path. The diameter of the endoscope will be increased while the working distance of the side-viewing OCT will be reduced. It may be possible to use a custom capillary tube with a hollow core as an annular waveguide¹⁴⁰. A short length of rigid capillary tube could be placed around the proximal end of the rigid tip including the DRCP. The OCT beam would still need to pass through the waveguide, but the optical power would be rotationally symmetric and could be compensated for in the design of the DRCP. A ring of collection fibers could be placed at the proximal end of the waveguide in order to transmit light through the flexible region of the endoscope back to the proximal systems. As with the ring of collection fibers outside the DRCP the approach may increase the diameter of the endoscope, but still warrants further consideration if placing the collection fibers behind the DRCP proves to be an issue.

After initial proof of concept testing the design can be modified in terms of size and optical characteristics for a specific application. This could include the addition of illumination wavelengths for color or multispectral fluorescence imaging.

C.2. Lens Prescription

The following lens design presented in the technical write-up was developed using Zemax OpticStudio.

GENERAL LENS DATA:

```

Surfaces          :      10
Stop              :      1
System Aperture   : Object Space NA = 0.27
Telecentric Object Space:On
Field Unpolarized :On
Convert thin film phase to ray equivalent :On
J/E Conversion Method :X Axis Reference
Glass Catalogs    : SCHOTT MISC
Ray Aiming        :Off
Apodization       : Uniform, factor = 0.00000E+00
Reference OPD     :Exit Pupil
Paraxial Rays Setting :Ignore Coordinate Breaks
Method to Compute F/# :Tracing Rays
Method to Compute Huygens Integral : Force Spherical
Print Coordinate Breaks :On
Multi-Threading   :On
OPD Modulo 2 Pi   :Off
Temperature (C)   : 2.00000E+01
Pressure (ATM)    : 1.00000E+00
Adjust Index Data To Environment :Off
Effective Focal Length : 1e+10(in air at system temperature and pressure)
Effective Focal Length : 1e+10(in image space)
Total Track       : 4.929082
Image Space F/#    : 1.783075
Paraxial Working F/# : 10000
Working F/#       : 10000
Image Space NA     : 0
Object Space NA    : 0.27
Stop Radius       : 0.08412435
Paraxial Image Height : 0.2145519
Paraxial Magnification : -1.072759
Entrance Pupil Diameter : 5.60829e+09
Entrance Pupil Position : 1e+10
Exit Pupil Diameter : 0
Exit Pupil Position : 1e+10
Field Type        : Object height in Millimeters
Maximum Radial Field : 0.2
Primary Wavelength [μm] : 1
Angular Magnification : 1.291327e+10
Lens Units        : Millimeters
Source Units      : Watts
Analysis Units     : Watts/cm^2

```

Afocal Mode Units : milliradians
 MTF Units : cycles/millimeter
 Include Calculated Data in Session File :On

Fields : 4

Field Type : Object height in Millimeters

#	X-Value	Y-Value	Weight
1	0.000000	0.000000	0.000000
2	0.000000	0.100000	0.000000
3	0.000000	-0.150000	0.000000
4	0.000000	-0.200000	1.000000

Vignetting Factors

#	VDX	VDY	VCX	VCY	VAN
1	0.000000	0.000000	0.000000	0.000000	0.000000
2	0.000000	0.000000	0.000000	0.000000	0.000000
3	0.000000	0.000000	0.000000	0.000000	0.000000
4	0.000000	0.000000	0.000000	0.000000	0.000000

Wavelengths : 1

Units: μm

#	Value	Weight
1	1.000000	1.000000

SURFACE DATA SUMMARY:

Surf	Type	Radius	Thickness	Glass	Clear Diam	Chip Zone	Mech Diam
Conic	Comment						
OBJ	STANDARD	Infinity	0.3		0.4	0	0.4 0
STO	STANDARD	-2.916766	0.5973911		N-LAK8	1	0 1 0
2	STANDARD	-0.7113811	0.01602361			1	0 1 0
3	STANDARD	1.777779	1.500039		N-LASF44	1	0 1 0
4	STANDARD	-2.182404	0.8156279			1	0 1 0
5	NONSEQCO	Infinity	0		0.7765599	0	0.7765599 0
6	STANDARD	Infinity	2		2	0	2 0
IMA	STANDARD	Infinity			0.9418269	0	0.9418269 0

SURFACE DATA DETAIL:

Surface OBJ STANDARD

Surface STO STANDARD

Aperture : Floating Aperture

Maximum Radius : 0.5

Surface 2 STANDARD

Aperture : Floating Aperture

Maximum Radius : 0.5

Surface 3 STANDARD

Aperture : Floating Aperture
Maximum Radius : 0.5

Surface 4 STANDARD

Aperture : Floating Aperture
Maximum Radius : 0.5

Surface 5 NONSEQCO

Draw Ports? : 3
Decenter X : 0
Decenter Y : 1.21
Decenter Z : 0.7
Tilt About X : -90
Tilt About Y : 0
Tilt About Z : 0
Order : Decenter then tilt

There are 2 objects:

Object 1 :

Object Type : Odd Asphere Lens (NSC_OVAS)

Face 0 : Side Faces

Face Is : Object Default

Coating : WAR

Scattering : None

Face 1 : Front Face

Face Is : Reflective

Coating : (none)

Scattering : None

Face 2 : Back Face

Face Is : Reflective

Coating : (none)

Scattering : None

Reference Object : 0

Inside Of : 0

XYZ Position : 0 0 0.83180789

Tilt About XYZ : 0 0 0

Pos. Mtrx. R11 R12 R13 X : 1.00000000E+00 0.00000000E+00 0.00000000E+00 0.00000000E+00

Pos. Mtrx. R21 R22 R23 Y : 0.00000000E+00 1.00000000E+00 0.00000000E+00 0.00000000E+00

Pos. Mtrx. R31 R32 R33 Z : 0.00000000E+00 0.00000000E+00 1.00000000E+00 8.31807894E-01

Material : ACRYLIC

Index at 1.000000 μm = 1.48327291

Radial Aperture : 1.2

Thickness : 1.1

Radius 1 : -0.10820785

Conic 1 : -1.1852483

Coeff 1 r^1 : 1.1199547

Coeff 1 r^2 : 0

Coeff 1 r^3 : 0

Coeff 1 r^4 : 0

```

Coeff 1 r^5      :      0
Coeff 1 r^6      :      0
Coeff 1 r^7      :      0
Coeff 1 r^8      :      0
Coeff 1 r^9      :      0
Coeff 1 r^10     :      0
Coeff 1 r^11     :      0
Coeff 1 r^12     :      0
Radius 2        :   -4.3286492
Conic 2         :   -18.058599
Coeff 2 r^1     :   -0.032753362
Coeff 2 r^2     :   -0.0025186434
Coeff 2 r^3     :      0
Coeff 2 r^4     :      0
Coeff 2 r^5     :      0
Coeff 2 r^6     :      0
Coeff 2 r^7     :      0
Coeff 2 r^8     :      0
Coeff 2 r^9     :      0
Coeff 2 r^10    :      0
Coeff 2 r^11    :      0
Coeff 2 r^12    :      0

Object 2        :
Object Type     : Odd Asphere Lens (NSC_OVAS)
Face 0         : Side Faces
Face Is        : Object Default
Coating        : (none)
Scattering     : None
Face 1         : Front Face
Face Is        : Object Default
Coating        : (none)
Scattering     : None
Face 2         : Back Face
Face Is        : Object Default
Coating        : (none)
Scattering     : None
Reference Object : 0
Inside Of      : 0
XYZ Position   :      0      0  0.76180789
Tilt About XYZ :      0      0      0
Pos. Mtrx. R11 R12 R13 X : 1.00000000E+00 0.00000000E+00 0.00000000E+00 0.00000000E+00
Pos. Mtrx. R21 R22 R23 Y : 0.00000000E+00 1.00000000E+00 0.00000000E+00 0.00000000E+00
Pos. Mtrx. R31 R32 R33 Z : 0.00000000E+00 0.00000000E+00 1.00000000E+00 7.61807894E-01
Material       : ACRYLIC
Index at 1.000000 μm = 1.48327291
Radial Aperture :      0.527
Thickness      :      0.07
Radius 1      :   -1.2207757
Conic 1       :      0
Coeff 1 r^1   :      0

```

Coeff 1 r^2	:	0
Coeff 1 r^3	:	0
Coeff 1 r^4	:	0
Coeff 1 r^5	:	0
Coeff 1 r^6	:	0
Coeff 1 r^7	:	0
Coeff 1 r^8	:	0
Coeff 1 r^9	:	0
Coeff 1 r^10	:	0
Coeff 1 r^11	:	0
Coeff 1 r^12	:	0
Radius 2	:	-0.10820785
Conic 2	:	-1.1852483
Coeff 2 r^1	:	1.1199547
Coeff 2 r^2	:	0
Coeff 2 r^3	:	0
Coeff 2 r^4	:	0
Coeff 2 r^5	:	0
Coeff 2 r^6	:	0
Coeff 2 r^7	:	0
Coeff 2 r^8	:	0
Coeff 2 r^9	:	0
Coeff 2 r^10	:	0
Coeff 2 r^11	:	0
Coeff 2 r^12	:	0

Surface 6 STANDARD

Surface IMA STANDARD

MULTI-CONFIGURATION DATA:

Configuration 1:

1 Field wgt 1 :	0
2 Field wgt 2 :	0
3 Field wgt 3 :	0
4 Field wgt 4 :	1
5 Ignore 7-9 :	1
6 Ignore 5-6 :	0
7 Wavelength 1 :	1

Configuration 2:

1 Field wgt 1 :	1
2 Field wgt 2 :	1
3 Field wgt 3 :	1
4 Field wgt 4 :	0
5 Ignore 7-9 :	0
6 Ignore 5-6 :	1

7 Wavelength 1 : 0.406

SOLVE AND VARIABLE DATA:

Semi Diameter 1 : Fixed

Semi Diameter 2 : Fixed

Semi Diameter 3 : Fixed

Semi Diameter 4 : Fixed

Surf 5 NSC Object 2 Position Z : Pickup From 1 Scale 1.0000E+00 Offset -7.0000E-02 Column
Current

Surf 5 NSC Object 2 Parameter 19: Pickup From 1 Scale 1.0000E+00 Offset 0.0000E+00
Column Parameter 5

Surf 5 NSC Object 2 Parameter 20: Pickup From 1 Scale 1.0000E+00 Offset 0.0000E+00
Column Parameter 6

Surf 5 NSC Object 2 Parameter 21: Pickup From 1 Scale 1.0000E+00 Offset 0.0000E+00
Column Parameter 7

Semi Diameter 6 : Fixed

Semi Diameter 8 : Fixed

Semi Diameter 9 : Fixed

C.3. MATLAB Scripts

The modified version of the Gaussian beam propagation script used in the technical write-up follows. The ABCD matrix generating functions are identical to the those in the previous appendix and are not repeated. A short script to plot the spiral scan in figure 18 is also included.

```
%% ABCD matrix gaussian beam prop for NA increase with GRIN lens
% Code to propogate gaussian beam through optical system. The code
% calculates the q-factor after each element and plots the gaussian
beam
% waist through the system. Use 'ABCD_*.m' functions to generate
ABCD
% matrices. The 'BeamWaist.m' function generates the beam waist
through z
% given the q factor for a give space.
%
% Note that if you want to change the number of spaces you need to
change
% the num_spaces variable, add/delete the space, add/delete the ABCD
% matrices for the space and following interface, add/delete the
desired
% plotting code.
%
% All lengths are microns. Distances must be integers
%
% A GUI would be nice
%
% Last updated: 12/12/2016
% Author: Tyler Tate

%% Set Wavelength

lambda = .406; %microns

%% Set number of mediums light propgates through including SM fiber

num_spaces = 4; %beam exists in n spaces (e.g. 5 spaces would be: SM
fiber, no-core, GRIN, no-core, air)

%% Code initializes various vectors. You should not need to edit
this section

num_mats = num_spaces*2-1; %num ABCD matrices (spaces plus
interfaces)
M = zeros(2,2,num_mats); %init 3D vector of ABCD mats.
n = ones(num_spaces,1); %init index vector
d = zeros(num_spaces,1); %init dist traveled vector
w0 = ones(num_spaces,1); %init beam waist vector
```

```

z_loc = zeros(num_spaces,1); %init vector of distance from current
pos to beam waste
z_shift = zeros(num_spaces,1); %init vector to track beam waste axis
shifts
q = zeros(num_spaces,1); %init vector of q factor after each mat
space_name = cell(num_spaces,1); %init vector of space names

%% Now define each propogation medium (space)

% space 1. (where the beam starts)
% SMF-28 fiber in this example
%edit these values
s = 1; %current space number
space_name(s) = cellstr('SM Fiber'); %set name of space
z_loc(s) = 0; %beam waist located at z=0
z_shift(s) = z_loc(s); %set shift for gaussian equations
SM_fiber_dia = 125; %microns
MFD = 3; %mode field diameter in microns. 5.9 for HI1060, 5 for
HI780
w0(s) = MFD/2; %beam waist exiting fiber
% note from thorlabs website forum:
% refractive index of 780HP at 780nm: Core = 1.4598 Clad = 1.4537
% from http://fibersensor-phys450.wikidot.com/ the index of pure
silica
% at 980 is 1.4507 and the 780HP fiber is +.0059 higher = 1.4566
% Thus I am estimating that index at 890 is average of those two.
n(s) = 1.469; %approx index of 780hp fiber
d(s) = 0; %Length of propogation. This should be zero for this
application
%don't edit this
q(s) = 1i*n(s)*pi*w0(s)^2/lambda; %q factor exiting fiber

%space 2. (prop through no-core)
%No-core fiber parameters
s=2;
space_name(s) = cellstr('No Core Fiber'); %set name of space
%Information from thorlabs on FG125LA: "We don't specify the
refractive
% index for this fiber, but based on using the raw glass preform
data,
% the cladding index could be 1.452 at 890 nm"
% Molly had 1.4487 from unknown source.
% The difference between the two is 1-2% in terms of final
parameters.
n(s) = 1.469; %index of no-core fiber
d(s) = 310; %physical length of no-core in microns (Dirk
example=360)

%space 3 (prop through grin)
%GRIN Fiber parameters
s = 3;
space_name(s) = cellstr('GRIN Fiber'); %set name of space
ap_GRIN = 62.5; %clear aperture diameter of GRIN fiber
n(s) = 1.478; %reference index for GRIN
% Note that pitch p=2*pi/g. For g=.006 this gives 1047.2 microns.

```

```

% So for every 523.6 micron multiple added to length, same ending
% parameters result, but image flips.
g = .006; %GRIN profile in reciprocal microns
d(s) = 340; %physical length in microns

%space 4. (prop through air)
%Air parameters
s=4;
space_name(s) = cellstr('Air'); %set name of space
n(s) = 1; %index of no-core fiber
d(s) = 250; %physical length to plot prop in tissue (make longer
than WD to graph properly)
%

%% Define ABCD matrices
% Generate ABCD matrix for each space and interfaces between them.

M(:, :, 1) = ABCD_Prop(d(1)); %prop in space 1. ID mat is d(1)=0
M(:, :, 2) = ABCD_FlatRef(n(1), n(2)); %Interface 1 (fiber to no-core)
M(:, :, 3) = ABCD_Prop(d(2)); %prop through no core
M(:, :, 4) = ABCD_FlatRef(n(2), n(3)); %Interface 2 (no-core to GRIN)
M(:, :, 5) = ABCD_GRIN(g, d(3)); %prop through GRIN
M(:, :, 6) = ABCD_FlatRef(n(3), n(4)); %Interface 3 (GRIN to air)

%% Transfer gaussian beam through each ABCD matrix

% First define a distance vector that tracks total traveled distance
of beam
d_cum = zeros(length(d), 1);
d_cum(1) = d(1);
for k=2:length(d_cum)
    d_cum(k) = d_cum(k-1)+d(k);
end

% Loop does a propagation and the following interface on each
iteration
for k=1:num_spaces-1
    in = [q(k); 1]; %input
    Msys = M(:, :, 2*k) * M(:, :, 2*k-1); %ABCD mat for prop then
interface
    out = Msys*in; %output
    q(k+1) = out(1)/out(2); %generate new normalized q factor
    z_loc(k+1) = real(q(k+1)); %beam waist location is real part of
q factor
    z_shift(k+1) = d_cum(k) - z_loc(k+1); %track beam waist loc
relative to each space
    w0(k+1) = sqrt(imag(q(k+1)) * lambda / (n(k+1) * pi)); %calc beam
waist for each space
end

%% Generate plot of beam waist size through system

%note that q-factor gives beam waist and location. The Gaussian

```

```

%equations are defined such that the beam waist is located at z=0.
Z_shift
%is used to shift the output from gaussian equations to the global
%coordinate system.

% %define axes
xmin = -200; %distance left of fiber face to plot for visual clarity
xmax = sum(d(1:end)); %distance to plot right of zero
ymin = 0; %optical axis is bottom of plot
ymax = SM_fiber_dia/2; %height of plot limited to SM fiber radius
z = linspace(z_loc(1),xmax,xmax-z_loc(1)+1); %define z axis (1
sample/micron)

h = figure('Name','NA expansion','Position', [20, 200, 750, 450]);
%init figure loc and size
axis([xmin xmax ymin ymax]); %set fig axes
hold on %set so figure overlays each of the following plots

%Plot features for SMF fiber
%plot beam in fiber as horizontal line for visualization
line([xmin 0],[w0(1) w0(1)], 'Color', 'b', 'linewidth',2);
%add vertical line for fiber/no-core interface
s = 1;
line([d_cum(s)+1 d_cum(s)+1], [0 ymax], 'Color', 'k');
%add text box for fiber specs
str = {char(space_name(s))};%, ['n = ' num2str(n(s), '%.4f')], ['MFD
= ' num2str(MFD, '%.2f') '\mum'];
text((xmin+d(s))/2,ymax*.9,str, 'HorizontalAlignment', 'center', 'Verti
calAlignment', 'top');

%plot beam in 1st no-core
s = 2; %no-core is space 2
domain = z(d_cum(s-1)+1:d_cum(s)+1); %it exists in this range
%calc beam waist over appropriate domain and z_shift
nc_beam = BeamWaist(domain-z_shift(s),w0(s),lambda,n(s));
plot(domain, nc_beam, 'b', 'linewidth',2)
line([sum(d(1:s)) sum(d(1:s))], [0 ymax], 'Color', 'k');
str = {char(space_name(s))}; %, 'n =', num2str(n(s), '%.4f\n'), 'L
= ', [num2str(d(s), '%.0f') '\mum'], 'g= ', [num2str(g*1000, '%.2f'),
''];
text((d_cum(s-
1)+d_cum(s))/2,ymax*.9,str, 'HorizontalAlignment', 'center', 'VerticalA
lignment', 'top');

% add line for GRIN/Air interface and text in GRIN
s = 3;
line([d_cum(s)+1 d_cum(s)+1], [0 ymax], 'Color', 'k');
str = {char(space_name(s))}; %, 'n =', num2str(n(s), '%.4f\n'), 'L
= ', [num2str(d(s), '%.0f') '\mum'], 'g= ', [num2str(g*1000, '%.2f'),
''];
text((d_cum(s-
1)+d_cum(s))/2,ymax*.9,str, 'HorizontalAlignment', 'center', 'VerticalA
lignment', 'top');
%Following does a seperate ABCD prop through GRIN in short intervals
for

```



```

%plotting purposes.
int = 15; %interval width between points plotted in GRIN
domain = d_cum(s-1):int:d_cum(s); %domain in GRIN
domain = domain(2:end); %Don't want first coordinate as its on
boundary
dom_size = length(domain); %having length of vector is useful
waistheight = zeros(dom_size,1); %init vector for waist heigh inside
GRIN
Mtemp = ABCD_GRIN(g,int); %This is the prop vector in the GRIN with
interval width
z_loc_GRIN = zeros(dom_size,1); %init vector of distance from
current pos to beam waist
z_shift_GRIN = zeros(dom_size,1); %init vector to track beam waist
axis shifts
w0_GRIN = zeros(dom_size,1); %init vector to track min waist through
GRIN
qtemp = q(s); %set initial q factor in GRIN
%loop to calc q factor at each interval location through GRIN
for k=1:dom_size
    in = [qtemp;1]; %input vector
    out = Mtemp*in; %output vector
    qtemp = out(1)/out(2); %generate new normalized q factor
    z_loc_GRIN(k) = real(qtemp); %dist to waist
    z_shift_GRIN(k) = d_cum(s-1)+k*int-z_loc_GRIN(k); %shift loc to
global coordinates
    w0_GRIN(k) = sqrt(imag(qtemp)*lambda/(n(s)*pi)); %waist for
current beam shape
    waistheight(k) = BeamWaist(domain(k)-
z_shift_GRIN(k),w0_GRIN(k),lambda,n(s)); %find waist height at
current location
end
%plot results on graph
plot(domain,waistheight,'b:','linewidth',2);
%plot line representing max beam height in GRIN (clear aperature)
line([d_cum(s-1) d_cum(s)], [ap_GRIN/2
ap_GRIN/2], 'Color','k','LineStyle',':');

%plot beam in air
s = 4;
domain = z(d_cum(s-1)+1:d_cum(s)+1);
%calc beam waist over appropriate domain and z_shift
tissue_beam = BeamWaist(domain-z_shift(s),w0(s),lambda,n(s));
plot(domain, tissue_beam,'b','linewidth',2)
w0_loc = d_cum(s-1)+1-z_loc(end);
line([w0_loc w0_loc], [0 w0(s)], 'Color','g');
% %add Rayleigh range to plot
% zr = w0(s)^2*pi*n(s)/lambda;
% line([w0_loc-zr w0_loc-zr],[0 sqrt(2)*w0(s)], 'Color','g');
% line([w0_loc+zr w0_loc+zr],[0 sqrt(2)*w0(s)], 'Color','g');
str = {char(space_name(s));%, ['n =' num2str(n(s), '%.4f\n')],...
% ['WD=' num2str(-z_loc(s), '%.0f\n') '\mum'],...
% ['Spot Dia=' num2str(2*w0(s), '%.2f') '\mum'],...
% ['FWHM=' num2str(2*w0(s)/1.699) '\mum'],...
% ['\lambda=' num2str(lambda*1000, '%.0f'), 'nm'],...
% ['DOF=' num2str(2*zr, '%.0f') '\mum']};

```

```

text((d_cum(s-
1)+d_cum(s))/2,ymax*.9,str,'HorizontalAlignment','center','VerticalA
lignment','top');

%final graph formatting
hold off
title('Increased Fiber Divergence');
xlabel('Distance in microns');
ylabel('Beam radius in microns (1/e^2 intensity)');

```

Script to plot spiral scan with sampling density displayed:

```

%% PLOT SPIRAL SCAN
Ntotal = 1407; % total number of samples per image
Dairy = 38; % microns
Rimg = 2.032; %Image radius in mm
Nr = 21; % number of rings or branches of spiral)
t = linspace(0,Nr*2*pi,Ntotal); %vector of acquisition sample points
r = linspace(0,Rimg*1000,Ntotal); %vector of scan radius in microns
%paramertized Archimedean spiral
x = r.*cos(t);
y = r.*sin(t);
%Plot pattern
plot(x,y)
axis([-2100 2100 -2100 2100]) %set each value slightly larger than
Rimg
axis square %Forces plot area to be square
hold on %Add things to plot without overwriting
viscircles([0 0],Rimg*1000,'color','k') %plot max image size
viscircles([x',y'],Dairy*ones(Ntotal,1)/2); %plot airy disk at each
sample
hold off

```